NIFS-SWJTU Joint Project

for

the Chinese First Quasi-axisymmetric Stellarator

~Physics and Engineering Design~

Ver. 1.0

2018. May

National Institute for Fusion Science, National Institutes of Natural Sciences
Institute of Fusion Science, School of Physical Science and Technology, Southwest Jiaotong University

Documentation Contributors

(Alphabetical order)

Akihiro Shimizu	National Institute for Fusion Science
Chihiro Suzuki	National Institute for Fusion Science
Dapeng Yi	Hefei Keye Electro Physical Equipment Manufacturing
Hai Liu	Southwest Jiaotong University
Haifeng Liu	Southwest Jiaotong University
Kenichi Nagaoka	National Institute for Fusion Science
Mitsutaka Isobe	National Institute for Fusion Science
Shoichi Okamura	National Institute for Fusion Science
Yasuo Yoshimura	National Institute for Fusion Science
Yi Wan	Hefei Keye Electro Physical Equipment Manufacturing
Yuhong Xu	Southwest Jiaotong University

Contents

1. Introduction

The controlled nuclear fusion research is one of the most important issues for human beings because it is necessary to secure stable energy resources in order to enrich human life in the future. Fusion energy does not produce hydrocarbons and hence does not contribute to the global warming, which is one of the most serious environmental problems for Earth. The source of energy are isotopes of hydrogen, which are a common resource for the world because the hydrogen isotopes are obtained from seawater.

The development of technologies so far for making controlled nuclear fusion are based on two methods, namely, magnetic confinement of high temperature plasmas and the strong compression of high density plasmas with ultra-high intensity laser. For the magnetic confinement, high technology devices with strong magnetic field produced by large currents are used. This research started from the 1950s and varieties of different designs of magnetic confinement devices were proposed. After intensive research all over the world for more than a half century, two major magnetic confinement schemes have been established as candidates for the future fusion reactor design, namely, tokamak and stellarator.

These two designs have different advantages and disadvantages. Tokamak devices have better confinement property for high temperature plasmas because of their axisymmetric configuration of the magnetic field. However tokamaks have essential problems of suffering current disruptions, which is very hazardous for the devices, and the high cost of current drive system because a large plasma current flowing in the plasma is a necessary element for the tokamak concept. On the other hand, stellarator does not have current disruption problems and does not need high cost current drive system because it does not require plasma current as a necessary element of a magnetic confinement concept. However, because of the lack of axi-symmetry of the magnetic configuration, the confinement is degraded when the plasma temperature approaches the necessary conditions for the fusion reaction.

At present, large efforts toward magnetic confinement of high temperature plasmas are focused on tokamak researches. In France, ITER, the largest facility of magnetic fusion research is now under construction as an international joint project. This device is a tokamak type and it is planned to produce 10 times larger fusion reaction energy than the electric energy consumed for maintaining high temperature plasmas in the device. This program is the final goal of the long way in making good plasma confinement using tokamak type devices. As a next step of fusion research toward the power reactor, we must solve many engineering problems. One of those significant issues is technology problems related to the plasma current (disruptions and current

drive). It is strongly pointed out that we should have a multi-line research strategy for the future reactor design, namely, that we should continue the stellarator research as a safe candidate for the fusion power plant free from the plasma current problems.

When the bright news of achieving high electron temperature in the tokamak device in Russia was distributed throughout the world fusion community in 1969, all plasma experimentalists began to work on tokamak experiments, thus giving up research with their own devices with different concepts from the tokamak. Since then, the main line of magnetic confinement fusion has been based on the tokamak concept. However, there were two continuous research activities for devices with the stellarator concept. In Kyoto University, in Japan, a series of devices with the names of Heliotron (A, B, C, ... , D) were built and the plasma parameters were improved continuously. In Germany, a series of devices with the name Wendelstein (1, 2, 3, ..., 6) were producing very promising data with stellarator configuration. In the final phase of these series, Wendelstein 7a was built in Germany and started experiments in 1975. In Japan, Heliotron E was built and started experiments in 1980. Because the impact of experimental results from these devices were very large for the world fusion community, various types of stellarator programs were initiated in many countries in the 1980s.

In Japan, the designing work for LHD started in 1985, and the construction of the device began in 1989. In Germany, the first design workshop for Wendelstein 7-X (W7-X) took place in 1987 and the first modular coil was ordered in 1998. These two world leading stellarator devices with super-conducting magnets are now in operation for experimental research in various topics of magnetic confinement with stellarator concept. In addition to these large devices, there were two medium size stellarators in operation from the 1980s to the 2000s both in Japan and in Germany. The roles of these devices were to conduct supporting experimental research in advance of the completion of construction and starting the experiments in larger-size major devices. CHS was in operation from 1988 to 2006 and Wendelstein 7-AS was in operation from 1988 to 2002. The experimental results obtained in these devices before starting experiments in LHD and W7-X were very useful for planning experimental program in large devices. They also produced unique scientific results available only in the smaller size devices. In addition to these two experiments, many different types of stellarators were designed and built in other countries: in the United States, ATF with heliotron configuration and HSX with quasi-helical symmetric configuration started experiments in the 1980s. TJ-II in Spain and H-1 in Australia, both having the heliac configurations, started experiments in the 1980s. Among these devices, experiments in four devices are active at present, namely, LHD, W7-X, HSX, and TJ-II. Four other devices stopped

experiments (ATF, W7-AS, CHS, and H-1).

The 1980s was an exciting period for stellarator research as many devices were designed and constructed. Fortunately, four devices continue in operation. However, we notice that it is too long for scientists in active research fields to keep running experiments in old devices designed and built more than 30 years ago even though the devices are in healthy condition for the experiments. In fact, there were two research activities for the advanced design of stellarator concept in 1990s. In Japan, when CHS completed its initial phase of experimental program, the discussion for the next device after CHS was initiated in 1995. After making surveys for the possible candidates of the next devices, a plan for building a quasi-axisymmetric stellarator CHS-qa was chosen. Based on the physics and engineering design, a proposal of CHS-qa was completed in 2000 and submitted to the National Institute for Fusion Science (NIFS). Unfortunately, the proposal was not accepted because 2000 was just after the beginning of the LHD experiments and NIFS did not have financial and personnel capability to share in two large programs.

In Princeton Plasma Physics Laboratory (PPPL), a stellarator experiment program started in 1995 for building a medium size stellarator NCSX (National Compact Stellarator Experiment) in parallel to the existing spherical torus experiment NSTX. The design concept was a quasi-axisymmetric stellarator similar to CHS-qa. It had N=3 toroidal period number different from N=2 for CHS-qa. The proposal of the device construction was approved and PPPL started to build NCSX in 2000. Unfortunately, this program was cancelled in 2008 because of the rapid increase of the construction cost, which the United States government did not accept.

The advanced concept of quasi-axisymmetric stellarator is very attractive as it is a new scheme of stellarator configuration that had not been imagined by any scientists before 1994. A toroidal device of magnetic confinement must have rotating structures of magnetic field lines in a plasma toroid which can be produced either by a plasma current or by twisting of the plasma surface. Because a twisting shape is not axisymmetric, it is not naturally possible to make a twisting system as axisymmetric. A quasi-axisymmetric stellarator is not a hybrid device of tokamak and stellarator, either. When we design a hybrid system of two different concepts, all advantageous points and disadvantageous points are mixed together in general. However, the quasi-axisymmetric stellarator combines only advantageous points from both tokamak and stellarator, thus producing a new advantageous concept. Because such a new invention of the stellarator concept was not realized in the real experimental program in 2000, we now need to recover the lost 15 years by starting a new quasi-axisymmetric

stellarator experiment with the Chinese First Quasi-axisymmetric Stellarator (CFQS).

The present design of the CFQS device incorporates numerous experiences we have learned in CHS-qa design work. In addition, we are adding many new design points that have been learned in theoretical and computational works during the past 15 years. The divertor configuration design, which is supposed be one of the most important research issues in advanced stellarator concept, was renewed from the CHS-qa design with a new concept of the island bundle divertor configuration. For the engineering design of the device and manufacturing, we will make use of new numerical technologies of mechanical design and of new engineering facilities in order to obtain very high accuracy of the three dimensional shape of the device.

This program is a joint project conducted by NIFS in Japan and Southwest Jiaotong University (SWJTU) in China. We concluded the MoU in 2017 on NSJP (NIFS and SWJTU Joint Project) for CFQS experiment. In addition, we are working together with Keye Electro Physical Equipment Manufacturing Co., Ltd. in Hefei with their contribution in engineering design and manufacture of the device. Thus, in fact, the program is a joint project by three organizations in Japan and China. We have been working together for the physics and engineering design of CFQS device. SWJTU and the Keye company are primarily responsible for the engineering design and for manufacturing the device. NIFS is primarily responsible to contribute in preparing plasma heating system and diagnostic system. The experiment in the device will be conducted as international collaborations by NIFS, SWJTU and other researchers in foreign countries who will be interested in the challenging advanced stellarator program in Chengdu, China.

In the following sections, important items in the physics and engineering designs of CFQS will be described. We hope this report will provide give sufficient information to all researchers in the world about our CFQS program and motivate them to participate in the joint program of NSJP.

2. Research target

The CFQS is an internationally joint project between SWJTU (China) and NIFS (Japan). It is the first stellarator to be manufactured and assembled by the Hefei Keye Electro Physical Equipment Manufacturing Co. Ltd. in China. Whereas in China there have been several tokamaks built by national institutions there is no stellarator up to now. As the stellarator is technically much more complicated than the tokamak, our first target is to successfully construct the CFQS device and make it in good operation status in SWJTU. Secondly, we want to scientifically prove the major advantage of a quasi-axisymmetric (QA) stellarator in confining plasmas with reduced ripple, and hence, neoclassical transport in comparison with previous conventional stellarators. Thirdly, for complementing the 2D tokamak physics, we will thoroughly study the intrinsic 3D physics in the CFQS stellarator to improve our understanding on related 3D issues appeared in the tokamak, which has primarily 2D magnetic configuration.

The main focus of the CFQS research activities is on basic physics studies under the advanced QA configuration. The scientific subjects include neoclassical transport, macro-scale MHD instabilities (*interchange, ballooning, kink and tearing modes, etc*), micro instabilities (*electron drift wave, ITG, TEM and ETG modes, etc*) and turbulence-induced transport, nonlinear interaction and energy cascading of multi-scale turbulence and zonal flows, confinement scaling and isotopic effects, plasma rotations, and edge and divertor physics. Special attention will also be paid on MHD activities arising from the bootstrap current and the maximum J issue in the QA configuration.

3. The physics design

3.1 Equilibrium

The characteristics of three dimensional magnetic field configuration is uniquely determined, if the geometry of outermost magnetic surface, the radial profile of pressure and the toroidal current as a function of flux are given [3.1-1]. The equilibrium of the magnetic field configuration is obtained by the VMEC code [3.1-2]. This code calculates the equilibrium from the given outermost magnetic surface, the pressure and the toroidal current profile. The geometry of the torus outermost magnetic surface can be parameterized by the Fourier series as follows,

$$R(\theta,\phi,s) = \sum \; R_{mn}(s)\cos\left(m\theta - N_p n\phi\right),$$
$$Z(\theta,\phi,s) = \sum \; Z_{mn}(s)\sin\left(m\theta - N_p n\phi\right).$$

Here, θ, ϕ, s are the poloidal angle, toroidal angle, and the radial flux coordinate, m, n, are the poloidal and toroidal mode, and N_p is the toroidal periodic number of the magnetic field configuration. In other words, the geometry of the outermost magnetic surface (namely, the characteristics of the magnetic field configuration equilibrium) is expressed numerically by the dataset of R_{mn}, Z_{mn}. In stellarator optimization, we consider these parameters (R_{mn}, Z_{mn}) as control parameters, and some specific characters of magnetic field configuration are optimized. For numerical optimization, characters of magnetic field configuration are expressed numerically. For example, the sum of non-axisymmetric components of magnetic field in the Boozer coordinates[3.1-3], the Mercier criteria of D_I, and the effective helical ripple ε_{eff} etc. are used for the numerical evaluation of the magnetic configuration. These values that characterize the magnetic field configuration are optimized by changing the control parameters, *i. e.*, (R_{mn}, Z_{mn}) by using a non-linear optimization method. The guiding center orbits of the charged particles in stellarators are determined by the absolute value of the magnetic field in the Boozer coordinates [3.1-3,4], therefore the spectrum of magnetic field strength B_{mn} in the Boozer coordinates are important. If the magnetic field strength in this coordinate system, B, is axisymmetric, e. g. it depends on only the θ, the guiding center orbits in this coordinates also become axisymmetric. This configuration is called as a quasi-axisymmetric system, because the geometry of plasma boundary is three dimensional, however, in the boozer coordinates the particle orbit becomes axisymmetric and the good particle confinement property like tokamaks can be achieved.

As the post CHS project, the quasi-axisymmetric device, CHS-qa, was designed in NIFS [3.1-5]. The parameters of this device were as follows: Toroidal periodic number N_p is 2, the toroidal magnetic field strength B_t is 1.5 T, the major radius R is 1.5 m, and

the aspect ratio A_p is 3.2, which is called as the 2b32 configuration. This configuration was designed to have a good quasi-axisymmetry with good magnetic well and ballooning mode stability. Based on this configuration, new quasi-axisymmetric configuration is designed for the Chinese First Quasi-axisymmetric Stellarator (CFQS). Toroidal periodic number N_p of 2, the toroidal magnetic field strength B_t of 1.0 T, the major radius R is 1.0 m are chosen for the CFQS. From the engineering point, the same low aspect ratio of the CHS-qa is not easy to realize, so the plasma size is shrunk and the aspect ratio 4 is selected. In Fig. 3.1-1, the equilibrium of vacuum magnetic surface calculated by VMEC code. The R_{mn}, Z_{mn} for the CFQS are shown in Table 3.1-1. The radial profile of the rotational transform and the magnetic well are shown in Fig. 3.1-2. The profile of rotational transform is low shear, and in the all radial region, the magnetic well property is realized.

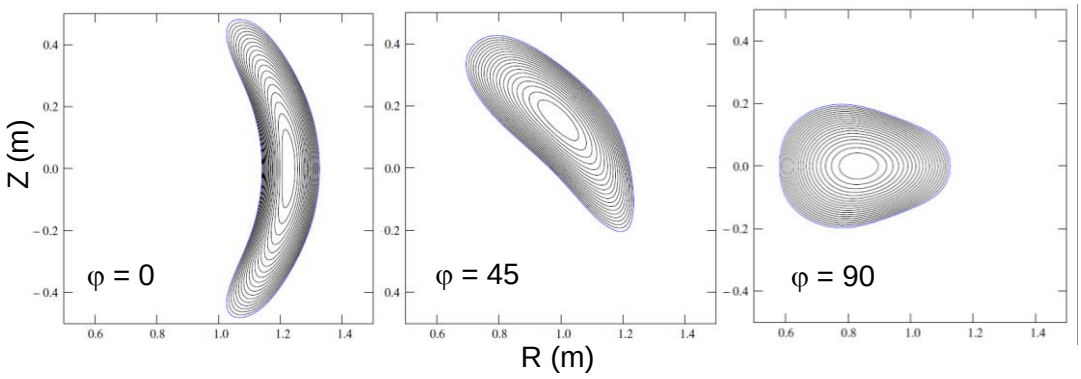

Fig. 3.1-1 CFQS vacuum magnetic surface calculated by VMEC code. Cross sections at toroidal angle of 0, 45, 90 degrees are shown.

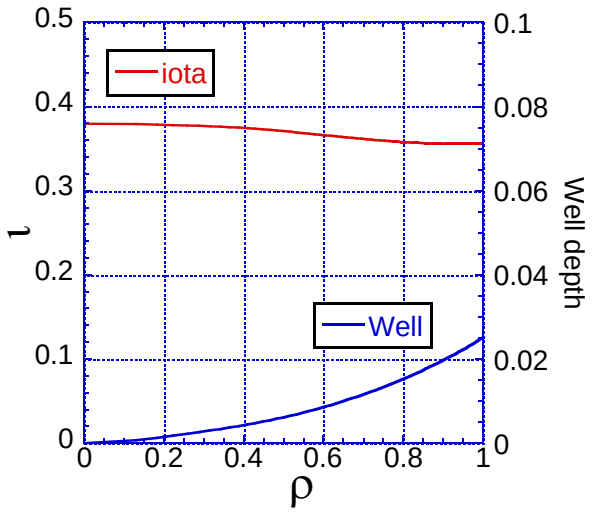

Fig. 3.1-2 The radial profiles of the rotational transform and magnetic well.

Table 3.1-1 The Fourier components of R_{mn}, Z_{mn} for the CFQS boundary surface

m	n	Rmn	Zmn
0	0	1.0000000E+00	0.0000000E+00
0	1	1.3918752E-01	-1.0414013E-01
0	2	3.5100658E-03	-2.0475983E-03
0	3	-1.0138762E-04	1.6428990E-03
0	4	-9.1750252E-05	1.8456690E-05
1	-4	2.7989089E-05	6.0830078E-05
1	-3	-8.3096040E-04	-1.0610252E-03
1	-2	5.3502814E-04	-1.2406187E-03
1	-1	3.2729681E-02	3.7654261E-02
1	0	1.9805122E-01	3.1531565E-01
1	1	-1.1902918E-01	1.0598813E-01
1	2	-9.8390157E-03	1.6001616E-02
1	3	-1.0368648E-04	-1.2356988E-03
1	4	-1.7749011E-04	-1.2332935E-05
2	-4	-1.2766617E-05	1.6195515E-05
2	-3	-2.2122215E-04	-1.6554195E-04
2	-2	2.6591390E-03	9.7085117E-04
2	-1	5.3927480E-03	3.9433596E-03

2	0	2.3684580E-02	5.2204140E-03
2	1	4.8005711E-02	1.8794565E-02
2	2	1.4185036E-02	-1.2816537E-02
2	3	6.3314713E-04	3.2291366E-03
2	4	3.2161498E-04	-3.0673594E-05
3	-4	-2.2443520E-05	-2.3378676E-05
3	-3	2.2473930E-06	7.0713582E-05
3	-2	1.5352426E-04	-7.0552937E-05
3	-1	2.7565433E-03	8.8330377E-04
3	0	-3.3340455E-03	3.2247828E-03
3	1	-7.5887014E-03	-6.6502611E-03
3	2	-5.4159396E-03	-2.3271074E-03
3	3	-1.3951568E-03	2.1069157E-03
3	4	3.4970178E-04	-6.3400330E-04
4	-4	-1.1323921E-05	4.6012342E-06
4	-3	2.9725326E-05	2.3180468E-05
4	-2	-5.7633646E-06	-6.4672276E-05
4	-1	-8.3562601E-05	-6.0365237E-05
4	0	2.3231144E-05	7.0775798E-04
4	1	1.5943290E-03	-9.7553194E-04
4	2	-1.0439876E-03	-2.9350188E-03
4	3	-3.6322487E-05	1.2533445E-03
4	4	8.9269815E-05	-2.0342868E-04
5	-4	-1.6603896E-06	-3.4285238E-06
5	-3	2.6346579E-06	4.2265526E-06
5	-2	2.7357046E-06	-5.4768039E-07
5	-1	2.2538179E-05	-1.3458213E-05
5	0	-6.2400690E-05	9.5602461E-05
5	1	2.9853761E-04	3.2243486E-04
5	2	2.5908595E-04	-7.4464898E-05
5	3	2.4740326E-04	2.5279785E-04
5	4	9.2800674E-05	-1.5522328E-04
6	-4	1.5257972E-05	-1.6282718E-05
6	-3	-3.1909260E-06	8.0248081E-06
6	-2	7.7656674E-06	-1.3497786E-06
6	-1	-6.6676361E-06	3.2346828E-05

6	0	-4.9591755E-05	-2.0796339E-04
6	1	2.2549727E-04	4.9671317E-04
6	2	-1.6547270E-04	-2.1090746E-04
6	3	4.0651174E-06	1.6411320E-04
6	4	-1.1442264E-05	-2.8567077E-05
7	-4	-1.1170521E-05	4.9738415E-06
7	-3	-2.0198698E-06	2.0807681E-06
7	-2	1.7530818E-06	9.1197790E-07
7	-1	8.9998125E-06	7.4200785E-06
7	0	-2.9831436E-05	-4.3511310E-05
7	1	7.5719416E-06	1.9510688E-05
7	2	1.2390900E-04	1.1000274E-04
7	3	-4.6991639E-05	-6.1617551E-05
7	4	3.8315450E-05	5.2277086E-05

References

[3.1-1] J. Nuhrenberg, R. Zille, physics Letters **A 129** (1988) 113.

[3.1-2] S. P. Hirshman, J. C. Whitson, Physics of Fluids **26** (1983) 3553.

[3.1-3] A. H. Boozer, Physics of Fluids **23** (1980) 904.

[3.1-4] A. H. Boozer, Physics of Fluids **24** (1981) 1999.

[3.1-5] S. Okamura *et al.*, Nuclear Fusion **41** (2001) 1865.

3.2 QA-ness

As stated above, the guiding center drift orbit is determined by the absolute value of B in the Boozer coordinates, because in the guiding orbit equation only the absolute value of B appears and the vector components of B do not appear. The Fourier components of the CFQS magnetic field in the Boozer coordinates are shown in Fig. 3.2-1. The toroidal ripple component, B_{10} is dominant for the good quasi-axisymmetric property. The contour map of magnetic field strength in the toroidal and poloidal angle plane are shown in Fig. 3.2-2.

Due to the quasi-axisymmetric property, the bootstrap current is driven from the neoclassical effect. The bootsj code can give us the bootstrap current in the collision less limit [3.2-1]. With the bootsj code, the bootstrap current is estimated for the CFQS. Fig. 3.2-3 shows the dependency of the bootstrap current on the averaged plasma beta. Here, low density case (n_{e0} =1.0 × 10^{19} m^{-3}, T_e = 10 T_i), and high density case (n_{e0} =2.0 × 10^{19} m^{-3}, T_e = T_i) are considered. Radial profiles for density, temperature are assumed to be

parabolic, $n_e \propto (1-\rho^2)$ and T_e, $T_i \propto (1-\rho^2)$. For the beta scan, n_e is fixed and the T_e, T_i are changed. The β of 1 %, the bootstrap current of 30 kA is expected. For low density case, the change of the rotational transform profile is shown in Fig. 3.2-4. The MHD instability, such as kink mode, will be studied in the future.

The neoclassical transport in the $1/\nu$ regime can be estimated by the NEO [3.2-2] code. By this code, so called the effective helical ripple ε_{eff}, is estimated and the neoclassical diffusion coefficient D is proportional to $v_d\ \varepsilon_{eff}^{3/2} / \nu$. Here, v_d and ν are the drift velocity and the collision frequency, respectively. The radial profile of ε_{eff} are shown in Fig.3.2-5. The magnetic configurations of the CFQS in this figure are calculated with VMEC, on fix boundary and free boundary condition. The ε_{eff} of the CFQS are two or three order less than that of the CHS. Up to the beta of 1.5%, the good neoclassical confinement property is kept.

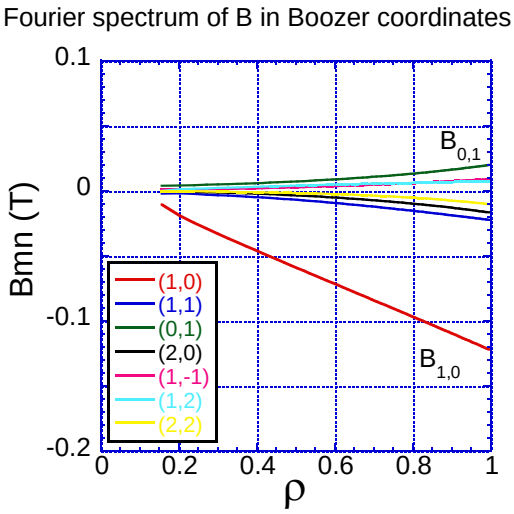

Fig. 3.2-1 The Fourier spectrum of B in Boozer coordinates.

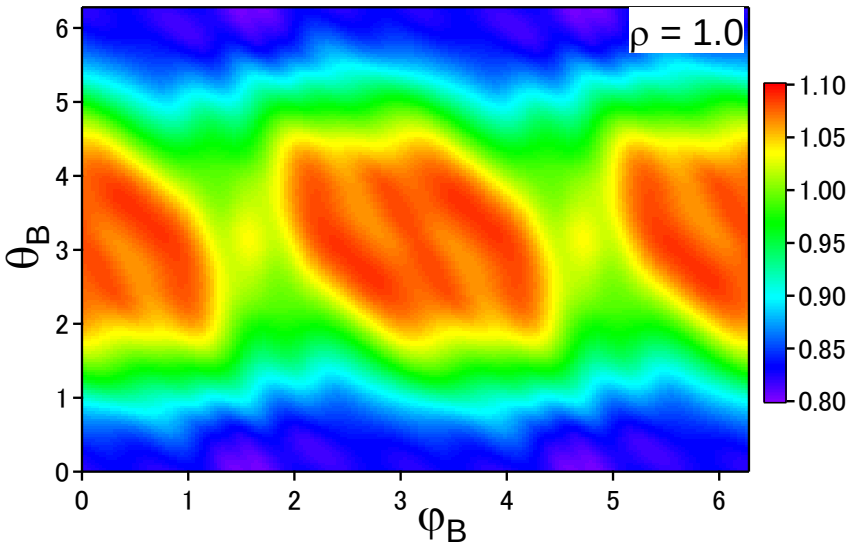

Fig. 3.2-2 The contour map of the magnetic field B in the Boozer coordinate on the outer most magnetic surface of the CFQS.

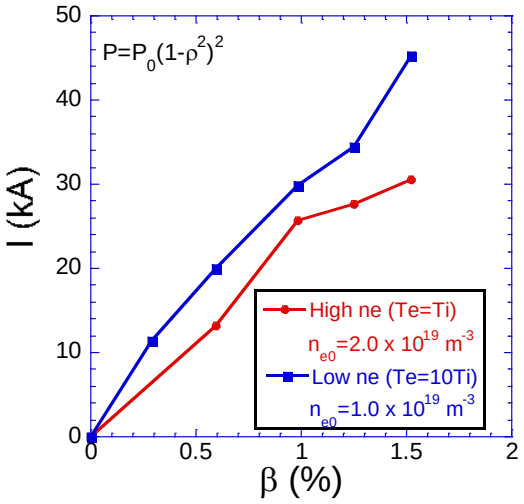

Fig. 3.2-3 The dependency of the bootstrap current on the plasma beta.

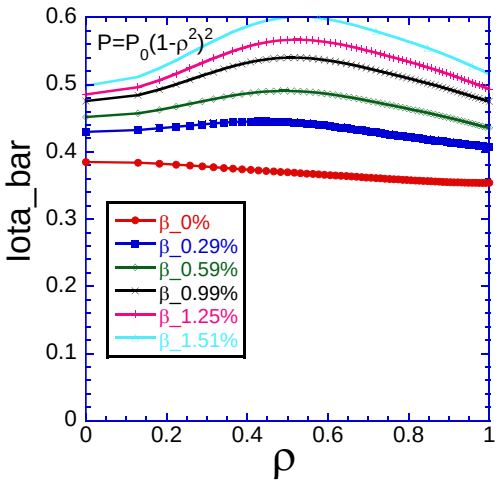

Fig. 3.2-4 The radial profile of the rotational transform considering the bootstrap current.

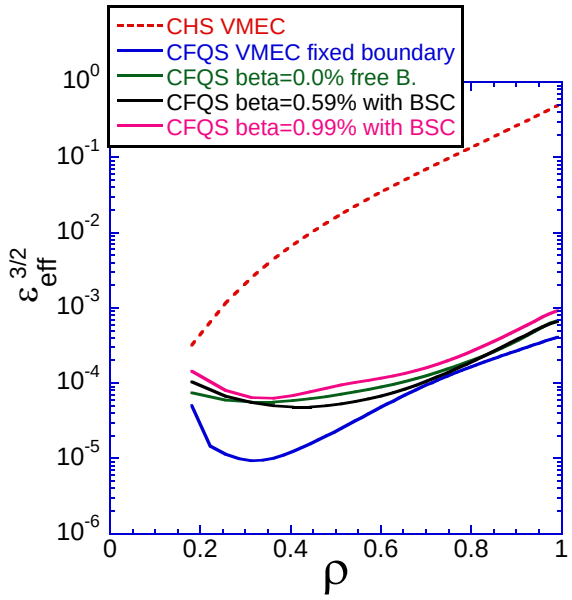

Fig. 3.2-5 The radial profile of the effective helical ripple, $\varepsilon_{eff}^{3/2}$, are shown. In the latter three cases, (green, black, pink), the free boundary calculation result of the VMEC are used to estimate $\varepsilon_{eff}^{3/2}$.

References

[3.2-1] K. C. Shaing *et al.*, Phys. Fluids **B 1** (1989) 148.

[3.2-2] V. V. Nemov, S. V. Kasilov *et al.*, Phys. of Plasmas **6** (1999) 4622.

3.3 MHD stability

Key MHD stabilities in the design of a finite-β quasi-axisymmetric stellarator configuration are discussed in this section. Mercier stability, ballooning mode, kink mode and tear mode are investigated to determination of β limit. These four issues are not independent. The VMEC, COBRAVMEC, BOOTSJ, TERPSICHOR codes are executed to estimate them [3.3-1~5].

References

[3.3-1] S.P. Hirshman, and J.C. Whitson, Phys. Fluids **26** (1983) 3353.

[3.3-2] A. H. Boozer, Phys. Fluids **24** (1981) 1999.

[3.3-3] K.C. Shaing, B.A. Carreras, N. Dominguez, et.al, Phys. Fluids **B1** (1989) 1663.

[3.3-4] R. Sanchez, S. P. Hirshman, J. C. Whitson, and A. S. Ware, J. Comp. Physics **161** (2000) 576.

[3.3-5] C. Mercier, Nucl. Fusion **1** (1960) 47.

3.3.1 Mercier

The Mercier criterion is a necessary condition for the stability of localized interchange modes in a toroidal plasma, according to the ideal magnetohydrodynamic (MHD) model [3.3.1-1]. These modes are localized around mode-rational surfaces, where the parallel wavevector vanishes, so as to minimize the magnetic field line bending energy. The driving force for these modes is the pressure gradient across surfaces with average unfavourable curvature. The Mercier stability criterion involves competition between the driving force and the stabilizing effect of magnetic shear. The Mercier criterion can be written as summation of four terms, corresponding to the contributions coming from the shear, magnetic well, net currents, and geodesic curvature, respectively.

Once the coils have been designed it needs to be established that these coils actually reproduce the desired MHD equilibrium and its relevant properties. For this purpose, free boundary equilibria were computed for volume averaged $\langle\beta\rangle=0$ and $\langle\beta\rangle = 2\%$. The cross sections of the plasma boundary obtained from free boundary equilibrium calculations (i.e. using the external magnetic field generated by the coils described in Sec. 4.2) are obtained. A comparison of the flux surfaces of the vacuum field and the $\langle\beta\rangle = 2\%$ solution (both VMEC) is presented in Fig. 3.3.1-1. It is observed that the Shafranov shift of the axis exists. The variation of Shafranov shift with $\langle\beta\rangle$ is displayed in the Fig. 3.3.1-2. When volume averaged beta equals 1.7%, the Shafranov shift is about the half of the minor radius.

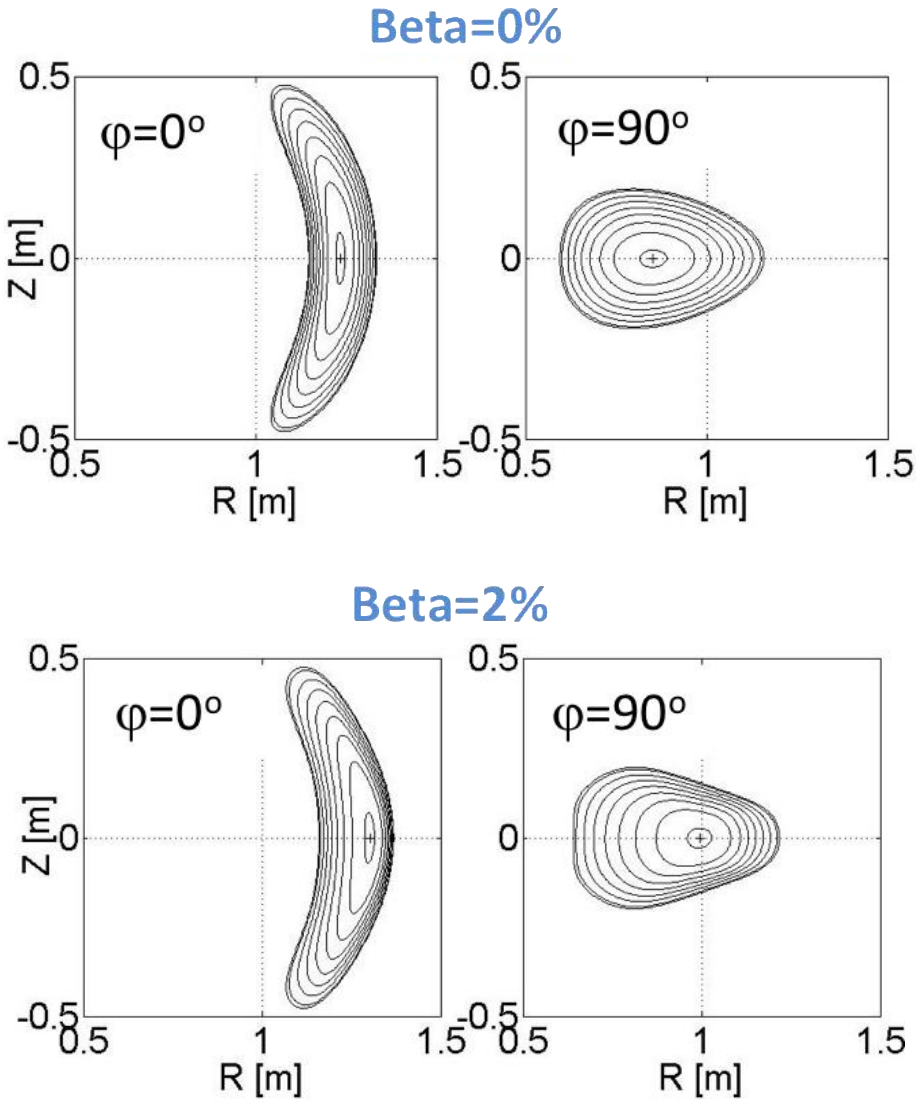

Fig.3.3.1-1 Toroidal cuts of the free boundary equilibrium (VMEC calculation) with the plasma pressure free (top panel) and volume averaged <β>=2% (bottom panel).

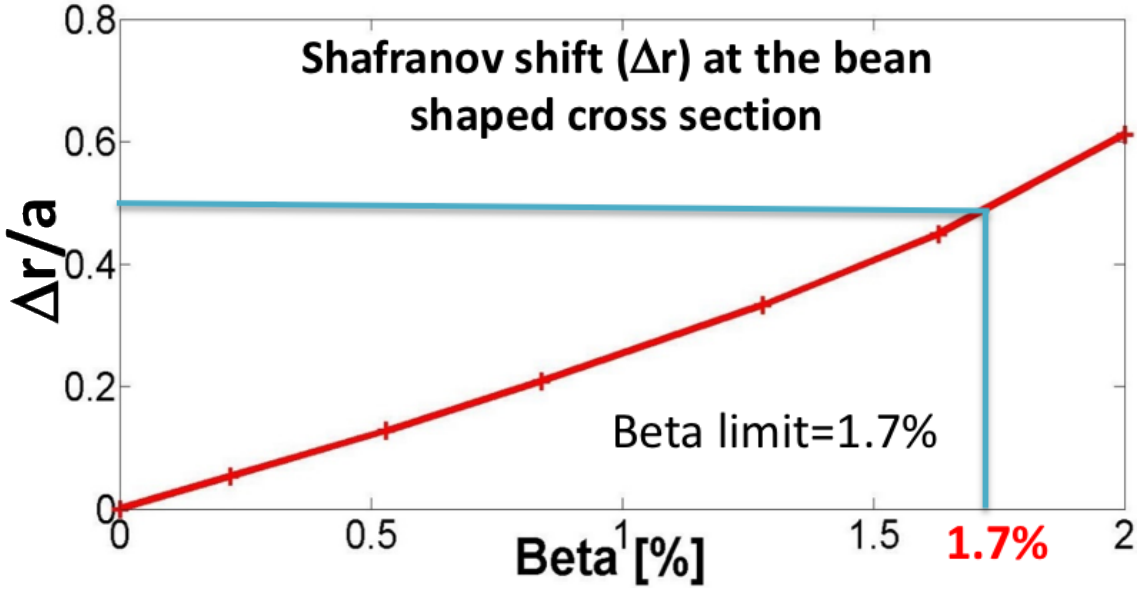

Fig.3.3.1-2 Shafranov shift vs the volume averaged <β> at the crescent shape cross section.

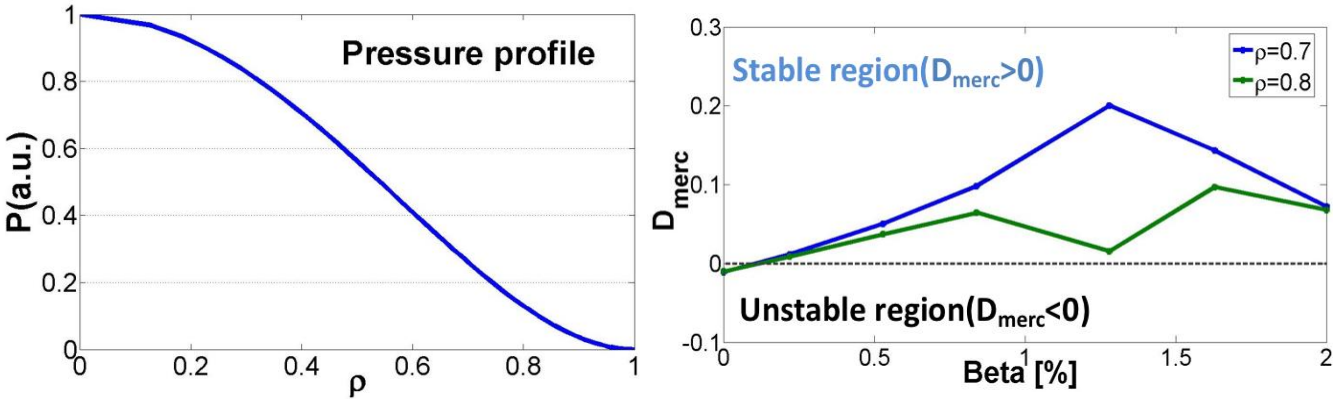

(a) (b)

Fig.3.3.1-3 (a)Assumed radial profile of plasma pressure (quadratic form) and (b) the variation of Mercier stability with the volume-averaged beta at two different radial position at two different radial position, ρ=0.7 and 0.8, respectively.

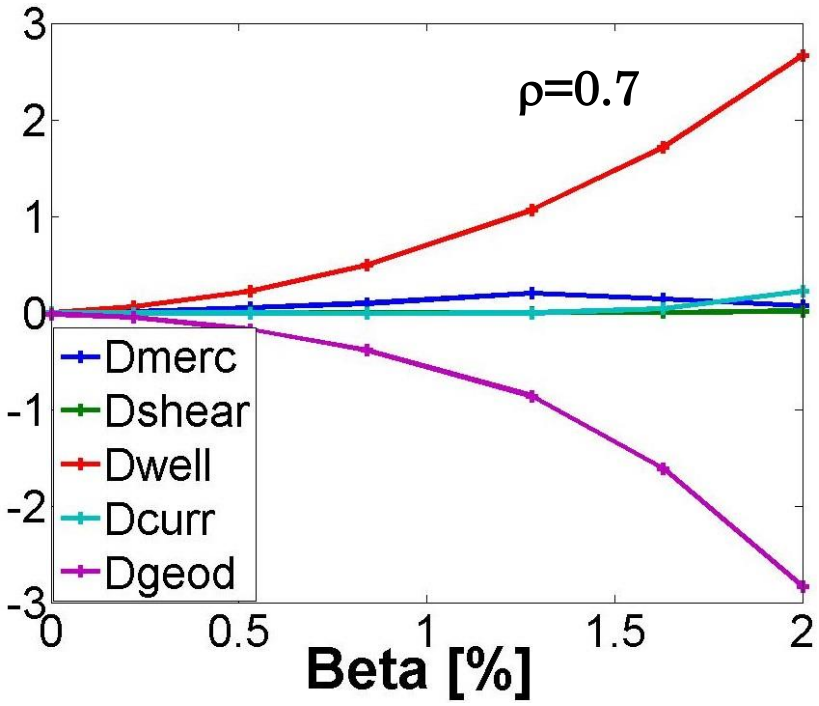

Fig.3.3.1-4 The shear term, well term, current term and geodesic curvature term versus the volume-averaged beta at radial position ρ=0.7, showing stabilization from the contribution of magnetic well.

The Fig.3.3.1-3. (a) gives the input profile of plasma pressure($p(\rho)=p_0(1+\rho^2)^2$) for the VMEC calculation with the unfixed plasma boundary and Fig.3.3.1-3. (b) displays the variation of Mercier stability with the volume-averaged beta at two different radial position at two different radial position, $\rho=0.7$ and 0.8, respectively. It shows that up to beta=2%, the interchange mode is stable. The Mercier criterion can be expressed as Dmerc=Dshear+Dwell+Dcurr+Dgeod, where these terms correspond to the contributions coming from the shear, magnetic well, net currents, and geodesic curvature, respectively. In the Fig.3.3.1-4, the variation of these four terms versus the volume-averaged beta at radial position $\rho=0.7$ is shown, which depicts the stabilizing effect from the magnetic well (Dwell > 0) is stronger than the destabilizing effect from the geodesic curvature term (Dgeod < 0).

References

[3.3.1-1] C. Mercier, Nucl. Fusion **1** (1960) 47.

3.3.2 Ballooning mode

A principle aim of stellarator research is to understand the physical mechanisms that limit the plasma stored energy. The expectation is that pressure driven instabilities will be excited as the plasma energy increases relative to the magnetic energy. Since one of the advantages of stellarators is the avoidance of current limiting instabilities, pressure driven instabilities may be critical in limiting stellarator operation. In theoretical studies of particular configurations, local criterion deduced from ideal magnetohydrodynamic (MHD) ballooning theory are often used to predict the plasma pressure limits of stellarators.

A feature related to second stability, which we call 'self-stabilization' for large pressure gradients after Ref.[3.3.2-1] has been observed in various stellarator experiments [3.3.2-2,3]. In these results, geometrical deformations associated with the Shafranov shift result in configurations which are stable with respect to Mercier modes as pressure is increased. In this section the COBRAVMEC code is utilized to calculate ideal ballooning stability for VMEC equilibria.

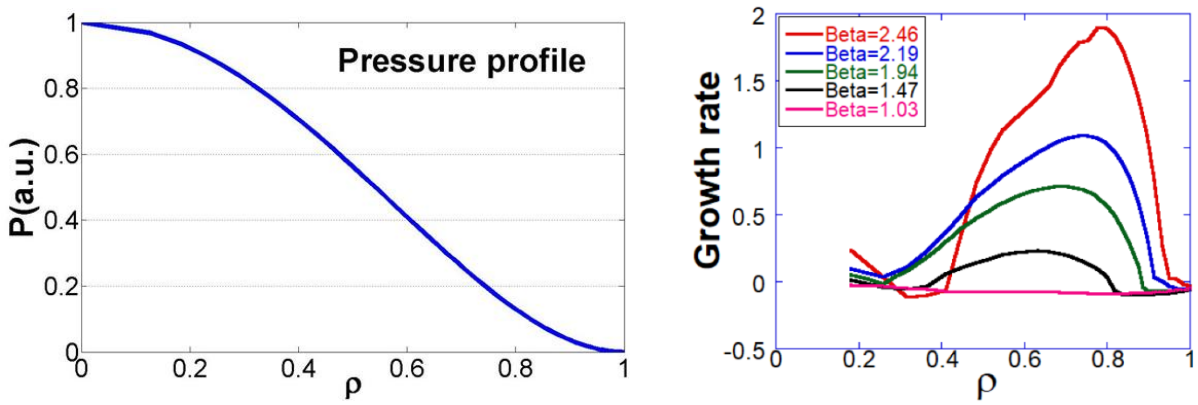

(a) (b)

Fig.3.3.1-1. (a)Assumed radial profile of plasma pressure (quadratic form) and (b) Ballooning growth rates from COBRAVMEC as a function of the normalized flux for various volume-averaged beta, indicating the first stability boundary.

For the reference configuration, a quadratic pressure profile, $p(\rho)=p_0(1+\rho^2)^2$ was chosen. Ballooning growth rates as a function of the normalized flux label, ρ, are shown in Fig.3.3.1-1.(a). As the plasma pressure is increased, the plasma first becomes ballooning unstable at 1.03%, displayed in Fig.3.3.1-1.(b). The region of instability grows until 3%, where a region of second stability appears as shown in Fig.3.3.1-2.

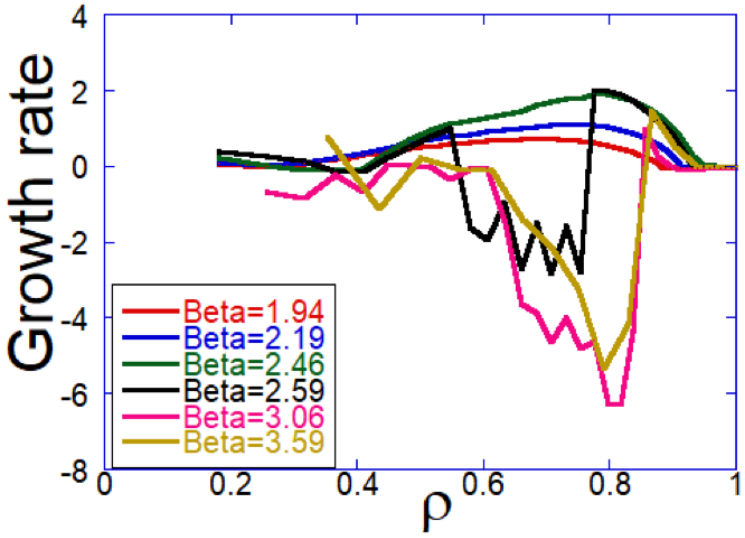

Fig.3.3.1-2 Ballooning growth rates from COBRAVMEC as a function of the normalized flux for various volume-averaged beta, indicating the onset of second stability.

References
[3.3.2-1] R. D. Hazeltine and J. D. Meiss, Plasma Confinement (Addision Wesley, Redwood City, 1992), pp. 309–312.
[3.3.2-2] C. C. Hegna and S. R. Hudson, Phys. Plasmas **9** (2002) 2014.
[3.3.2-3] R. Hudson and C. C. Hegna, Phys. Plasmas **10** (2003) 4716.

3.3.3 Kink mode

In a quasi-axisymmetric configuration, larger amount of bootstrap current (BSC) flows so as to increase rotational transform due to its tokamak-like magnetic field structure. Therefore, the onset of an external kink mode should be carefully assessed in the ideal MHD stability analysis including plasma current. If a BSC profile is given, global low-n ideal MHD stability can be calculated with TERPSICHORE code [3.3.3-1]. Since such a calculation for the CFQS configuration has not been performed yet, a typical example for the CHS-qa configuration [3.3.3-2] is described below.

A self-consistent BSC profile for a CHS-qa reference configuration has been calculated with SPBSC code [3.3.3-3]. We have solved finite beta equilibria including BSC assuming the fixed density and temperature profiles for three representative cases; (A) $n_e = 1.0\times10^{20}$ m^{-3}, $T_e = 1.04$ keV, (B) $n_e = 0.2\times10^{20}$ m^{-3}, $T_e = 5.2$ keV, (C) $n_e = 1.5\times10^{20}$ m^{-3}, $T_e = 1.04$ keV [3.3.3-4]. The resulting rotational transform is shown in Fig. 3.3.3-1 as a function of the normalized toroidal flux. Then the ideal global MHD stability has been analyzed with artificially changing the total parallel current while keeping its profile. The dependences of the most unstable eigenvalues on the total current are shown in Fig. 3.3.3-2 for the three representative cases. The onset of destabilization above 150 kA in the cases A and B clearly corresponds to the crossing of the edge rotational transform beyond 0.5 and 0.6. The associated amplitude of the dominant perturbation mode increases toward the edge, which clearly indicates the characteristics of an external kink instability. On the other hand, the global mode is kept stable up to 250 kA for the case C which has a different current profile. It indicates the possibility of stabilization of the external kink mode by controlling the current profile in a quasi-axisymmetric configuration.

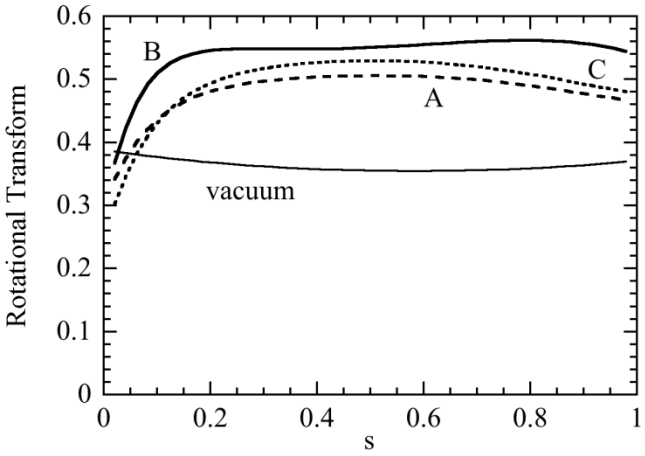

Figure 3.3.3- 1 The radial profiles of rotational transform for the three representative cases.

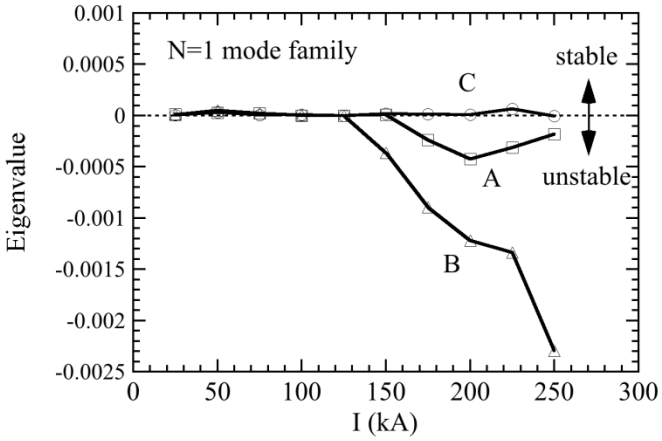

Figure 3.3.3- 2 The most unstable eigenvalues as functions of total current for the three representative cases.

References

[3.3.3-1] D.V. Anderson *et al.*, Int. J. Supercompt. Appl. **4** (1990) 34.

[3.3.3-2] C. Suzuki *et al.*, J. Plasma Fusion Res. SERIES **6** (2004) 519.

[3.3.3-3] K.Y. Watanabe *et al.*, Nucl. Fusion **35** (1995) 335.

[3.3.3-4] M. Isobe *et al.*, J. Plasma Fusion Res. SERIES **5** (2002) 360.

3.3.4 Tearing mode

The tearing mode stability, which is determined by Δ', is analyzed for existing singular point in the plasma region with the same code described in Ref. 3.3.4-1 for the CHS-qa configuration. Here, we consider a pressure less plasma in the cylindrical system with parabolic net toroidal current density J_z and check whether the tearing mode is stable or not at the rational surface of interest with increasing J_z. The tearing mode is stable for rational surfaces n/m=2/5, 3/7, 4/9 and 1/2 in the core domain (see Fig. 3.3.4-1) but the analyses indicate that it becomes unstable when singular point is in outer region (r/a>0.6) for n/m=1/2.

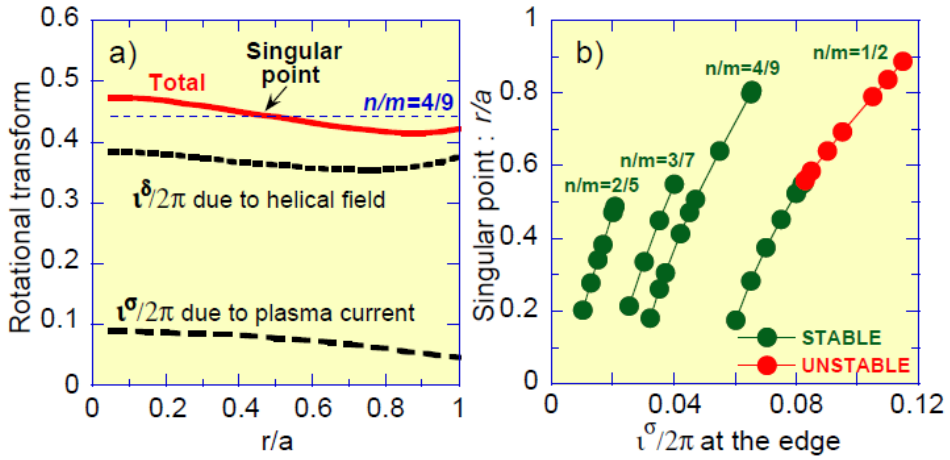

Fig. 3.3.4-1 (a) An example of rotational transform profile for tearing mode analysis for n/m = 4/9, and (b) Δ' analysis results are shown.

References

[3.3.4-1] K. Matsuoka *et al.*, Nuclear Fusion **17** (1977) 1123.

3.4 Micro instability and anomalous transport

3.4.1 maximum-J

The turbulent fluctuation suppression in the CFQS has got emphasized considerably. The suppression of the turbulent transport due to the sheared flow induced fluctuation decorrelation has been widely investigated, theoretically, leading to the significant progress in the understanding of the improved confinement regime. The other possible mechanism for turbulent suppression has been proposed based on the stabilization of microinstabilities. Several kinds of microinstabilities appear when directions of the diamagnetic drift and ∇B drift (B is the magnetic field strength) are in the same direction for trapped particles [3.4.1-1, 2]. In an axisymmetric configuration, the relevant drift is in the toroidal direction (toroidal precession). The velocity of the toroidal precession can be expressed in terms of the second adiabatic invariance J [3.4.1-3]. Also, the stability condition for microinstabilities is derived [3.4.1-4] with a scalar plasma pressure P as

$$\nabla P \cdot \nabla J > 0,$$

which is frequently called the maximum-J condition; it reduces to $dJ/dr < 0$ for a usual pressure gradient with $dP/dr < 0$. This indicates that microinstabilities can be stabilized or suppressed if the toroidal precession of trapped particles is in a favourable ($dJ/dr < 0$) direction.

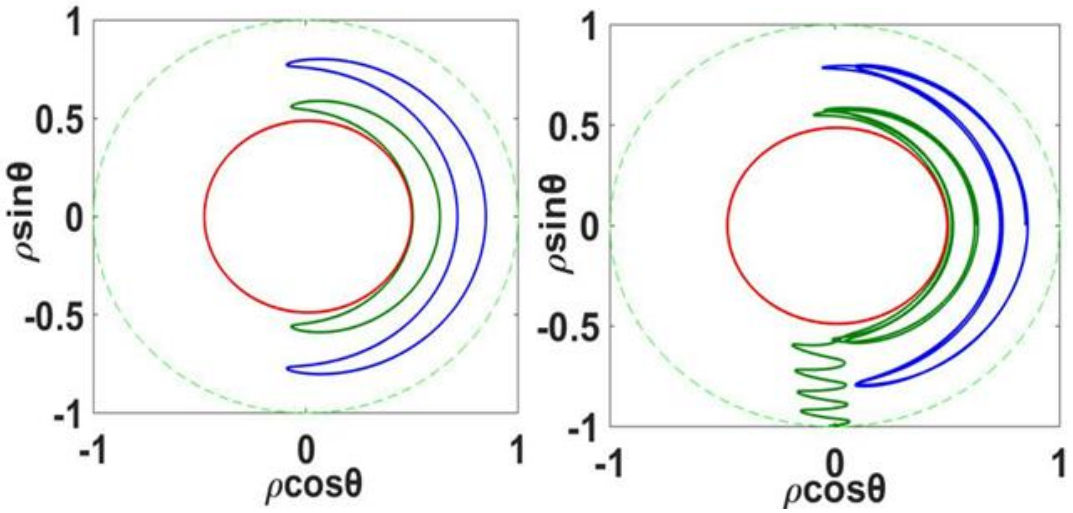

Fig. 3.4.1-1 Examples of the main orbit topologies in an axisymmetric versus a CFQS equilibrium. The dashed line represents the last closed flux surface in each case. (a) E=1Mev, Passing (red, B_{ref}=1.5) particles and Trapped (green, B_{ref}=0.94and blue, B_{ref}=0.98) particles orbit in axisymmetric equilibrium. (b) E=1Mev, Passing (red, B_{ref}=1.5) particles ,drifted (green, B_{ref}=0.94)particles and Trappled (blue, B_{ref}=0.98) particles orbit in the CFQS equilibrium.

Orbits of blocked or helically trapped particles: These particles are located in the region of phase space near the locally trapped- passing boundary. These particles may be regarded as locally trapped for a few bounces but they are able to de-trap collisionlessly. A blocked particle's trajectory is not restricted to a single toroidal segment but extends to neighbouring sections. Such particles are also called transitioning [3.4.1-5]. An illustration of these three types of orbits and a comparison with particle orbits in an axisymmetric plasma is given in Fig. 3.4.1-1.

The contour plot of J is shown as a function of the minor radius and the toroidal angle in the Fig. 3.4.1-2. The calculation of J is made by following the particle orbits starting from the outboard side of the torus with different toroidal angles. ζ_N = 0 corresponds to the vertically elongated cross section and ζ_N = 0.5 to the horizontally elongated cross section. When B_{ref} equals 0.95T, there is no maximum-J region. Whereas B_{ref} equals 0.97T, the maximum-J region comes up at the core area.

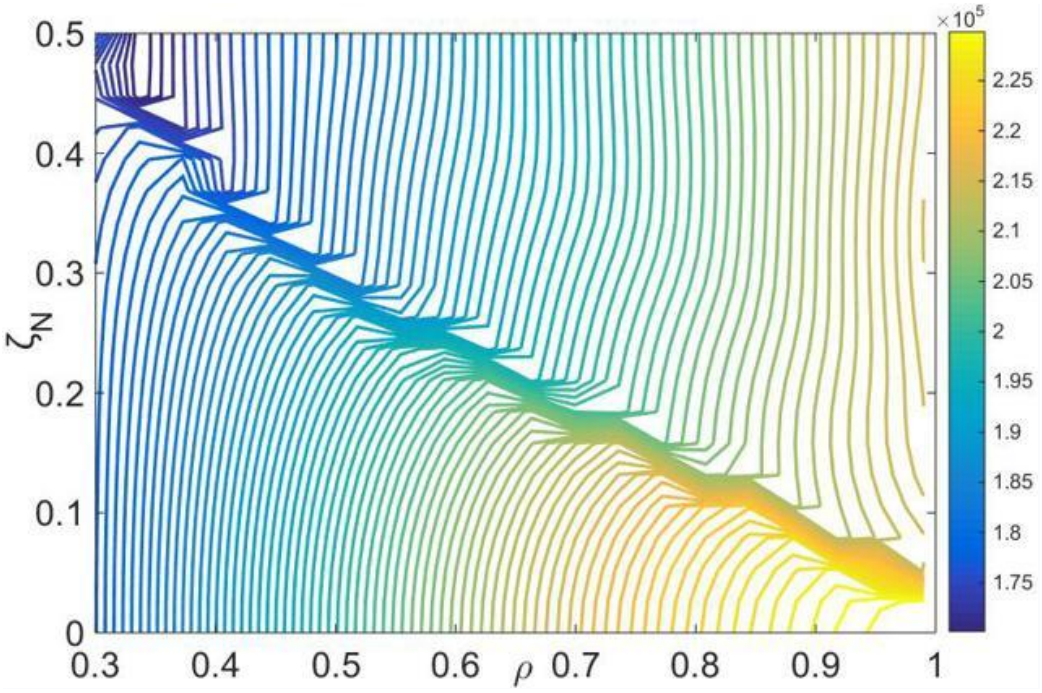

(a)

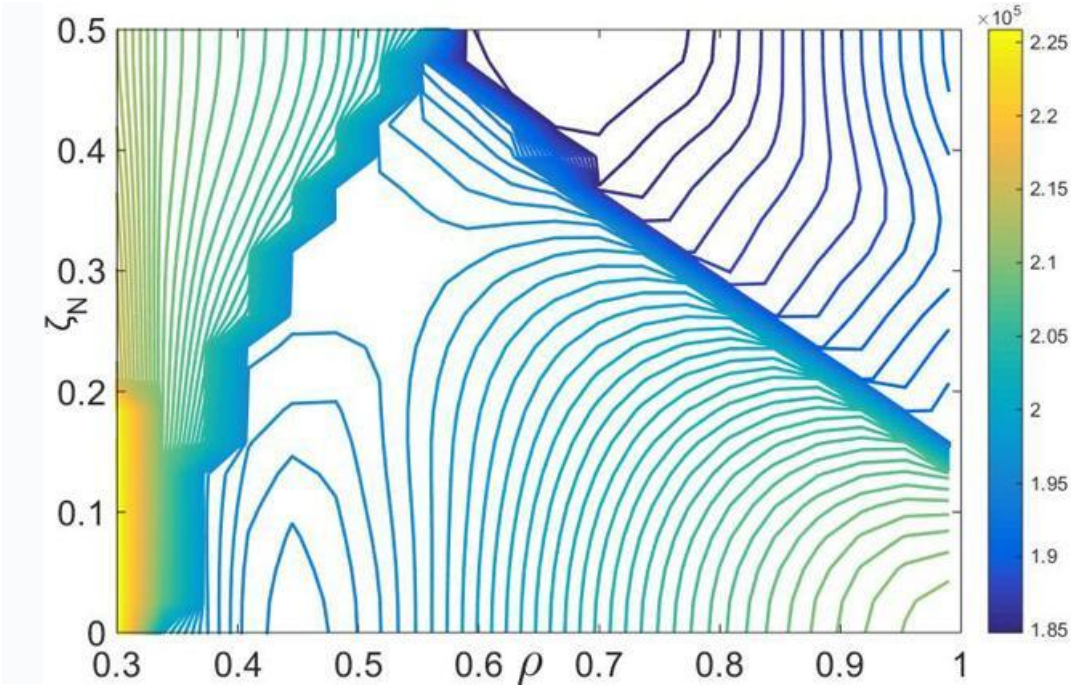

(b)

Fig. 3.4.1-2 The contour J on the (ρ, ζ_N) plane (a) B_{ref} equal to 0.95T, without maximum-J region and (b) B_{ref} equal to 0.97T, with maximum-J region.

References

[3.4.1-1] H. P. Furth and M. N. Rosenbluth 1969 Proc. Conf. 3rd Int. on Plasma Physics and Controlled Nuclear Fusion Research (Novosibirsk, 1968) vol **1** (Vienna: IAEA) p 821.

[3.4.1-2] B. B. Kadomtsev and O. P. Pogutse 1970 Reviews of Plasma Physics vol **5** (New York, London: Consultants Bureau) p 249.

[3.4.1-3] B. B. Kadomtsev and O. P. Pogutse Nucl.Fusion **11** (1971) 67.

[3.4.1-4] R. J. Hastie, J. B. Taylor and F. A. Haas, Ann of Phys **41** (1967) 302.

[3.4.1-5] C. D. Beidler, Ya. I. Kolesnichenko, V. S. Marchenko, I. N. Sidorenko and H. Wobig Phys. Plasmas **8** (2001) 2731.

3.4.2 Ion temperature gradient mode

3.4.3 Trapped electron mode and electron temperature gradient mode

3.5 Plasma rotation

In conventional helical devices, an impact of radial electric field on plasma confinement has extensively been investigated so far. It is one of the major issues also in a quasi-axisymmetric device because plasma rotation, which is closely related to radial electric field, can be driven more easily, and because anomalous transport can be possibly reduced by controlling plasma rotation/flow. Since the discovery of H-mode in tokamaks, the roles of shear flow on an improved confinement have been widely understood also in helical systems; e.g., high ion/electron temperature modes [3.5-1,2]. Consequently, the reduction of anomalous transport by shear flow has become a general issue in toroidal plasmas.

Unlike tokamaks, radial electric field or plasma rotation in helical devices are determined by a solution of an ambipolar condition according to the neoclassical theory. Also, toroidal plasma rotation tends to be dissipated in conventional helical systems because of larger toroidal viscosity which originates from larger toroidal ripple of magnetic field strength [3.5-3]. According to theoretical studies on tokamaks, transport barriers are established by a positive feedback mechanism that reduces the transport coefficients through the increase in local pressure gradient. Radial electric field (or plasma flow), which is strongly correlated with the local pressure gradient, is a key parameter for the mechanism mentioned above. In order to promote such spontaneous growths of shear flow and pressure gradient, plasma flow should be free from any constraints.

In conventional helical devices such as CHS, plasma mainly rotates poloidally because of larger toroidal viscosity. In this situation, Pfirsch-Schlüter-type return flow should exist so as to satisfy incompressibility, which can possibly be dissipated by helical ripple [3.5-4]. Therefore, it is quite difficult to drive high speed plasma rotation in conventional helical systems due to large parallel viscosity both in toroidal and poloidal directions. Indeed, the radial electric field strengths observed in CHS and Heliotron-E are around 100 V/cm at most. Furthermore, the scale length of the radial electric field tends to be longer, which leads to weaker shear. Consequently, tokamak-like transition phenomena relevant to edge transport barrier have never been observed so far in helical systems.

In order to establish transport barriers, a magnetic configuration should be free from any constraints of plasma flow due to parallel viscosity. This expended parameter range of plasma rotation is one of the reasons why we adopt the quasi-axisymmetric configuration, which is ideal for reducing toroidal viscosity as well as achieving low aspect ratio and incompressible flow at the same time.

In quasi-axisymmetric configuration, ripple trapped particles can be suppressed by reducing residual ripple. In such a situation, according to the neoclassical theory, confinement property is similar to that in an axisymmetric system. That is to say, values of radial electric field are never restricted by the ambipolar condition, which is a characteristic feature not found in the other optimized stellarators. As described below, the residual ripple in a quasi-axisymmetric configuration is drastically reduced in comparison with CHS.

In the earlier experiments in tokamaks and helical devices, it has been found that the plasma current, plasma rotation (or radial electric field) are well explained by the neoclassical theory, while particle/heat transport is dominated by anomalous transport [3.5-5]. The plasma rotation interpreted by the neoclassical theory gives a good hint to study the anomalous transport. Also, it is important to study the neoclassical theory itself as it is still incomplete for non-axisymmetric systems. In addition, it would be also important to investigate whether the neoclassical theory can predict bootstrap current, toroidal viscosity and radial electric field in a quasi-axisymmetric configuration with non-axisymmetric perturbation.

Neoclassical parallel viscosity is roughly proportional to the square of the magnetic field ripple strength defined by $\gamma^2 = < (\delta B/\delta s)^2 / B^2 >$, where $\delta/\delta s$ is differential with respect to the flow direction and $< >$ denotes averaging on a magnetic surface. This parameter should be quantitatively evaluated from the calculations including all of the Fourier components of the field strength B because higher order mode may largely contribute to the value of γ. Since the calculation of γ for the CFQS configuration has not been carried out yet, the results for the CHS-qa configuration [3.5-6] are shown hereafter. In principle, similar results are expected in the CFQS.

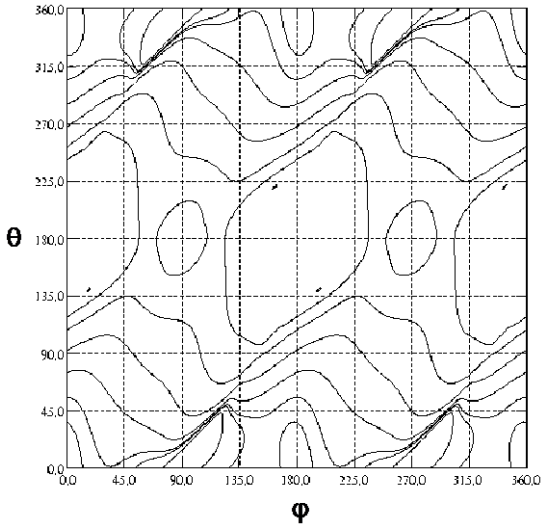

Fig. 3.5- 1 Contour plot of B for the LCFS of CHS-qa (2w39) configuration.

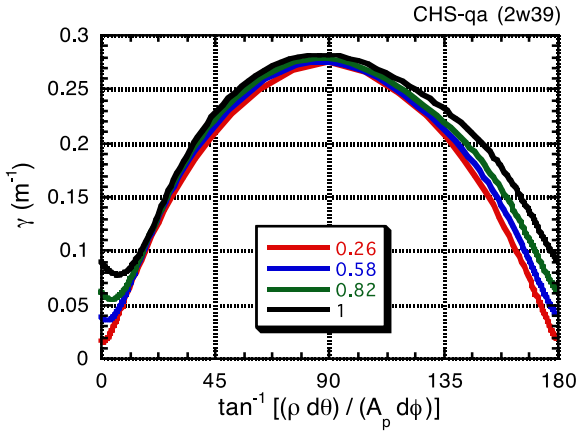

Fig. 3.5- 2 Angle dependence of γ for CHS-qa (2w39) configuration.

Fig. 3.5-1 shows a contour plot of B on the last closed flux surface (LCFS) of a reference configuration of CHS-qa (2w39). The grid data for B in cylindrical coordinates (R, Z, Φ) are constructed from the result of VMEC code calculation. Toroidal (ϕ) and poloidal (θ) angles are expressed in real coordinates, and $\theta = \tan^{-1}[(R-R_{ax})/(Z-Z_{ax})]$, where R_{ax} and Z_{ax} are R and Z values at the magnetic axis in an equal ϕ plane. This means that the effect of the excursion of the magnetic axis is ignored in the calculation. We assumed a flow direction expressed by a straight line in this ϕ-θ plane. When averaging, we fixed the angle of δ/δs direction with respect to the toroidal direction ($=\tan^{-1}(r\ \theta\ /R\ \phi)$).

Figure 3.5-2 shows the calculated dependence of γ on the flow direction at the four different flux surfaces (normalized minor radii of 0.26, 0.58, 0.82 and 1.0). As shown, the values of γ have peaks around 90 degrees in the quasi-axisymmetric configuration,

which indicates larger parallel viscosity in the poloidal direction. In the toroidal direction, γ is less than 0.1 even in the LCFS, which implies that perpendicular/anomalous viscosity plays an important role for determining toroidal rotation speed in a similar way to tokamaks. Though the effect of coil ripples are not included in the present calculation, the angle minimizing γ is not zero but 1.1~6.8 degrees unlike tokamaks, which is considered to be the effect of residual non-axisymmetric components.

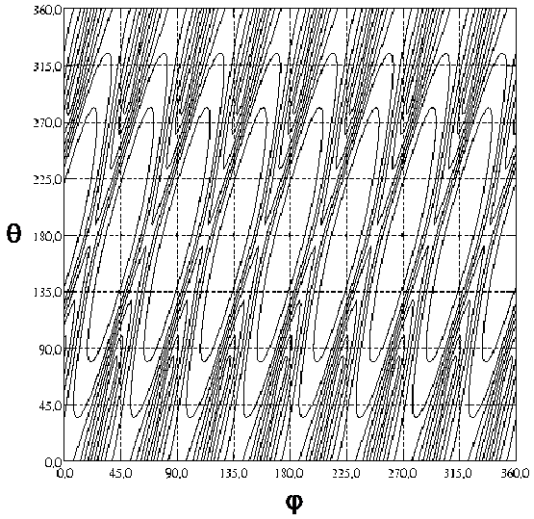

Fig. 3.5- 3 Contour plot of B for the LCFS of CHS (Rax=92.1 cm) configuration.

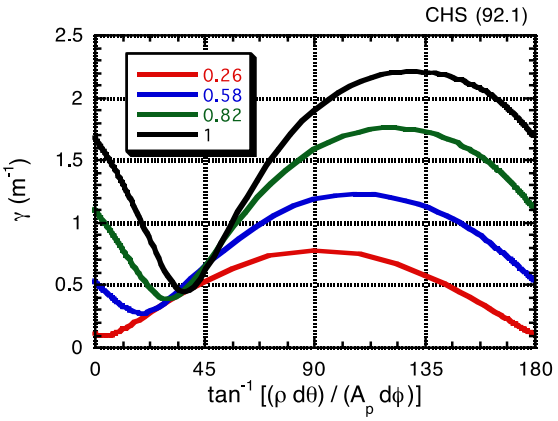

Fig. 3.5- 4 Angle dependence of γ for CHS (Rax=92.1 cm) configuration.

For the comparison with a conventional helical device, the calculation of γ has been performed for a representative configuration of CHS. The contour of B on the LCFS and the results of the γ calculation are shown in Fig. 3.5-3 and 3.5-4, respectively, in a similar way to the CHS-qa. The angle minimizing γ is around 40 degrees, which indicates the flow tends to be driven along the helical structure (m=2, n=1) of the CHS configuration. Nevertheless, this minimum value of γ in CHS is still larger than the

maximum value of γ along the poloidal direction in CHS-qa. Therefore, high speed toroidal rotation cannot be driven in CHS because of strong toroidal viscosity, as demonstrated in the previous CHS experiment.

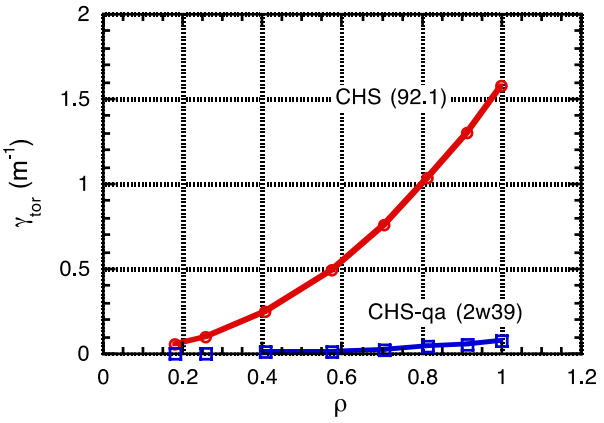

Figure 3.5- 5　Dependence of toroidal γ on minor radius for CHS-qa and CHS.

In reality, the direction of plasma flow cannot be expressed simply by a straight line in real coordinates. Experimental results in CHS suggests that the spontaneous rotation, which is driven without external momentum input (with NBI), tends to be driven along the direction minimizing parallel viscosity. In a quasi-axisymmetric configuration, this direction is the toroidal direction in Boozer coordinates. Therefore, we have also calculated γ with the angle of δ/δs direction fixed in Boozer coordinates. Fig. 3.5-5 shows γ in the toroidal direction as a function of normalized minor radius for CHS and CHS-qa. As shown, γ_{tor} in CHS-qa is much smaller than that in CHS, which implies tokamak-like nature of a quasi-axisymmetric configuration with respect to plasma rotation.

References

[3.5-1] K. Ida *et al.*, Phys. Rev. Lett. **76** (1996) 1268.

[3.5-2] A. Fujisawa *et al.*, Phys. Rev. Lett. **79** (1997) 1054.

[3.5-3] K. Ida, H. Yamada, H. Iguchi, K. Itoh, and CHS Group, Phys. Rev. Lett. **67** (1991) 58.

[3.5-4] S. Nishimura, K. Ida, M. Osakabe, T. Minami, K. Tanaka, and CHS Group, Phys. Plasmas **7** (2000) 437.

[3.5-5] O. Okamoto, NIFS-PROC-25 (1995).

[3.5-6] C. Suzuki et al., Plasma Phys. Control. Fusion **44** (2002) A225.

3.6 Energetic particle

Energetic alpha particles produced by the d-t reaction will play an essential role in sustaining a self-ignition condition in burning plasma in the future. When alpha particles are substantially lost from the plasma, the self-ignited state is easily terminated. Moreover, the localized heat load on the first wall due to the impact of the escaping alphas may seriously damage the device. Because of the reason above, a great deal of attention has to be paid to physics issues related to energetic ions such as the magnetic field ripple transport, anomalous transport and/or loss caused by MHD instabilities. Orbit characteristics of energetic ions have been numerically investigated for quasi-axisymmetric systems (QAS) of N=2 [3.6-1, 3.6-2, 3.6-3] and N=3 [3.6-4, 3.6-5, 3.6-6]. Although energetic-ion orbits in CFQS have not calculated yet, orbit characteristics and confinement properties are supposed to be similar to those in CHS-qa. Therefore, typical characteristics of EP behaviors in CHS-qa are described. Note that although neoclassical transport in CFQS is outstandingly reduced, it does not always guarantee good energetic ion confinement. Since QAS is quite similar to tokamak in magnetic field structure, EP orbits in QAS is also quite similar to those in tokamak. Figure 3.6-1 shows three-dimensional plots of typical orbits of collisionless energetic passing ion (H^+) ($v_{//}/v$~1) and toroidally trapped (or tokamak-like banana) ion with an energy of 38 keV in B_t of 1.5 T in the Cartesian coordinates for CHS-qa. Tokamak-like precessional drift of toroidally trapped ions can be clearly seen in Fig. 3.6-1(left).

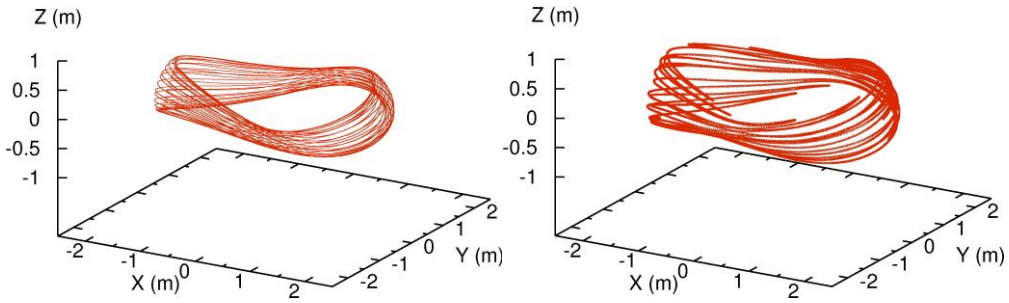

Fig. 3.6-1. Collisionless passing orbit (left) and toroidally trapped orbit (right) of energetic ion (H^+) with an energy of 38 keV in B_t of 1.5 T in the Cartesian coordinates for CHS-qa.

EP orbits have been also calculated in the Boozer coordinates. A typical guiding center orbit of toroidally trapped ion is shown in Fig. 3.6-2. Generally speaking,

toroidally trapped ion tends to diffuse radially due to residual non-axisymmetric magnetic field in QAS as seen in Fig. 3.6-2, like a rippled tokamak [3.6-7, 3.6-8]. Therefore, orbit characteristics of EPs in CFQS have to be carefully analyzed toward neutral beam injection heating.

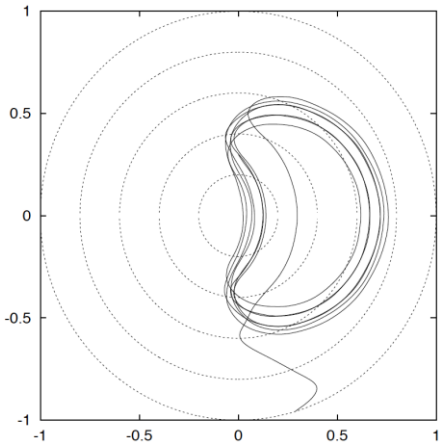

Fig. 3.6-2. Typical guiding center orbit of toroidally trapped energetic ion in QAS in the Boozer coordinates [3.6-9].

References

[3.6-1] S. Murakami *et al.*, Proceedings of 1997 International Symposium on Plasma Dynamics in Complex Electromagnetic Fields ~ for Comprehension of Physics in Advanced Toroidal Plasma Confinement ~, 8-11 December, 1997. **IAE-RR-98 054**, March 1998, pp. 137-140.

[3.6-2] M. Isobe *et al.*, 30th EPS Conference on Contr. Fusion and Plasma Phys., St. Petersburg, 7-11 July 2003 ECA Vol. **27A**, P-3.25.

[3.6-3] M. Isobe *et al.*, J. Plasma Fusion Res. SERIES, **6** (2004) 622.

[3.6-4] M.H. Redi *et al.*, Phys. Plasmas, **6** (1999) 3509.

[3.6-5] M.H. Redi *et al.*, Phys. Plasmas, **7** (2000) 2508.

[3.6-6] H.W. Kugel *et al.*, Fus. Sci. Technol., **51** (2007) 203.

[3.6-7] R.J. Goldston *et al.*, J. Plasma Physics, **26** (1981) 283.

[3.6-8] K. Tani *et al.*, J. Phys. Soc. Japan, **50** (1981) 1726.

[3.6-9] "*Experiment proposal for CHS-qa*", National Institute for Fusion Science, April 2000. (in Japanese)

4. Engineering design

4.1 Building

4.1.1 Torus hall

Subsystems of CFQS, briefly, include vacuum chamber, coil system, supporting structure, power supply, diagnostics, heating system, fueling system, cooling system and so on. The torus hall of CFQS is reconstructed by a workshop with 42 m in length, 15 m in width and 10 m in height, shown in the red dotted line area in figure 4.1. The hall is divided into 10 regions roughly. The locations and sizes of 10 regions are shown in figure 4.1 and figure 4.2, respectively. Brief descriptions of each region are given below:

1. Device region: the red part in figure 4.1. With a major radius, R=1 m, it is estimated that the entire device should occupy an area of about 4 m in diameter (compact arrangement). In the Device region, the vacuum chamber, coil system, supporting structure, first wall, molecular pumps, partial diagnostics (i.e. internal magnetic coils, optical probes and other internal components) are including. In addition, these should be a grounding system.
2. Diagnostic region: the yellow part in figure 4.1. In this region, there are electrostatic probes, optical diagnostics (CCD cameras, etc.), spectroscopic diagnostics (visible, VUV, H_α), microwave diagnostics, laser assisted diagnostics, Soft/Hard X-ray), etc. This region is generally located 1.5 meters outside the device region.
3. Precision diagnostic room: A room for the placement of precision diagnostic equipment (e. g. lasers, precision optics or electronics, etc.), which can meet some specific conditions. The area of the room is about 3×10 m^2.
4. Preassemble and repair region: This region is for the preparation and debugging

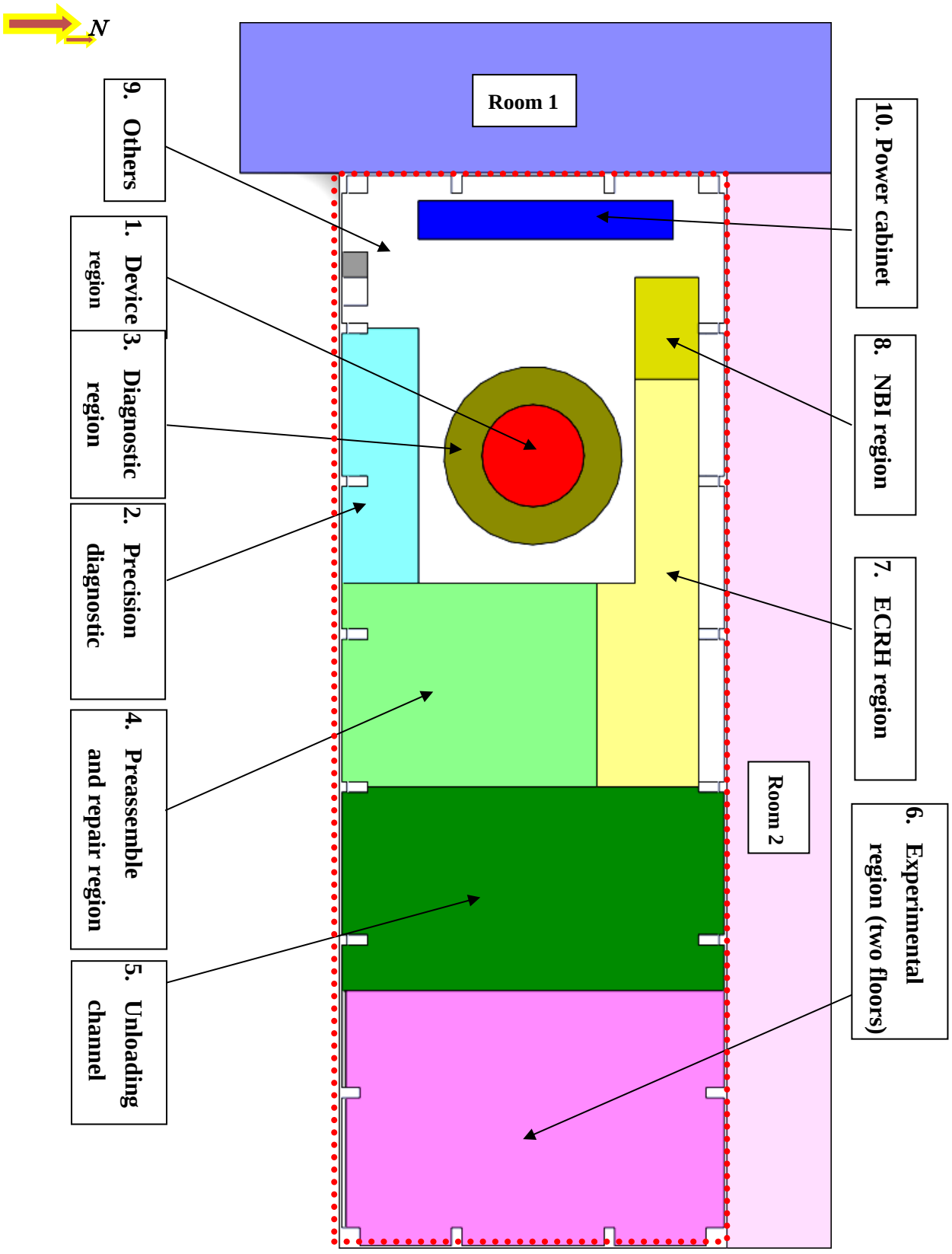

Fig. 4.1.1-1 Layout of the CFQS hall (indicated by red dotted line)

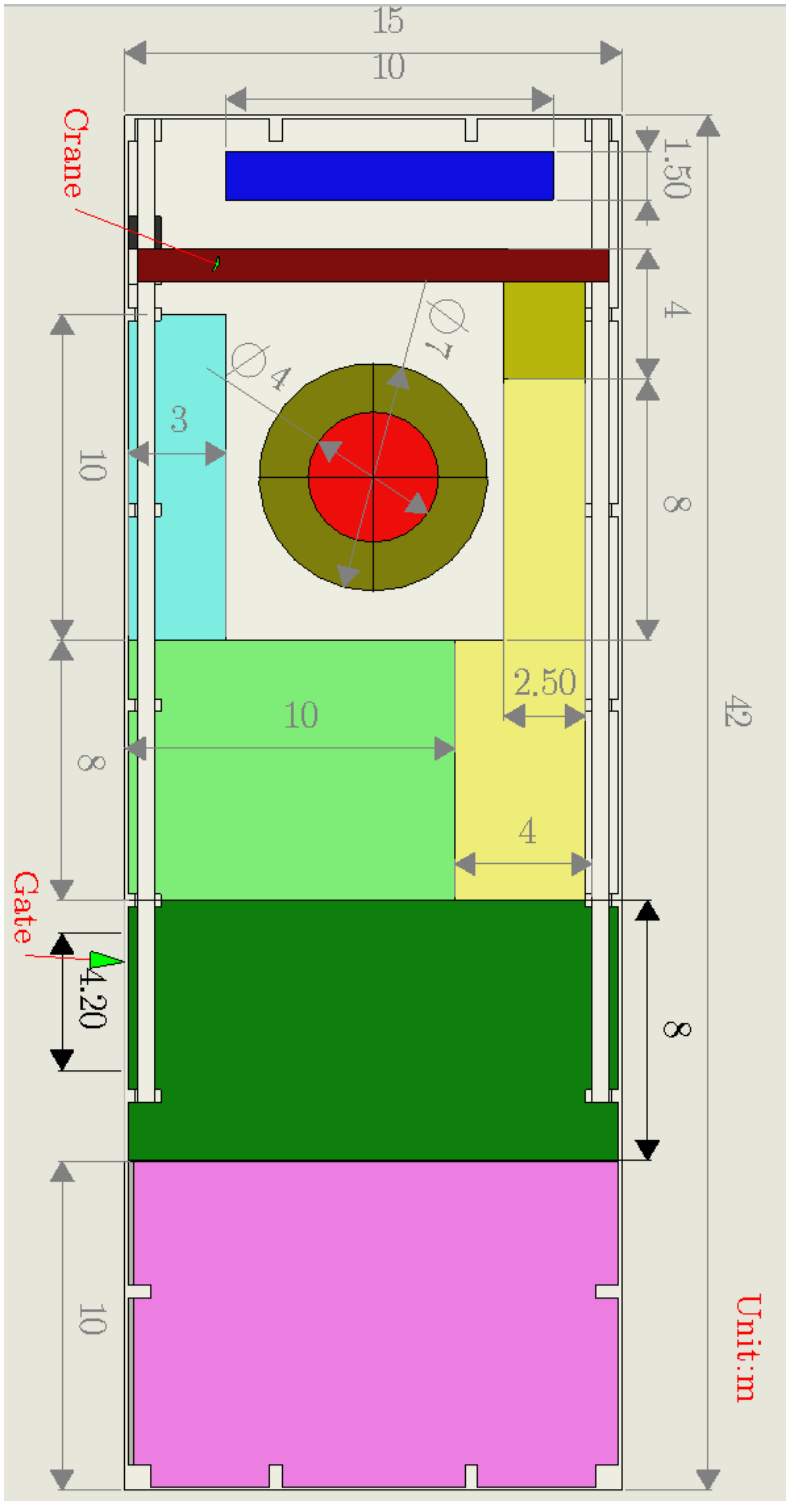

Fig. 4.1.1-2 Sizes of the CFQS hall (height between the crane bottom and ground is 7.8 m and the gate is 5.35 m in height)

before the assembling of the device and other components. It also includes the repair, leakage testing, cleaning, etc. of each component. The area of this region is about 8×10 m^2.

5. Unloading channel: This channel is toward to the Gate for unloading, lifting and so on.
6. Experimental region :This region is divide into several parts based on the different functions, including: Vacuum preparation room, Experimental material room, Metalworking workshop, Data handling room, Discharge control room and Central laboratory. This region is built two floors. Detail information is given in the figure 4.3, introduction of Experimental region.
7. ECRH region: This region is for placing the ECRH wave source system and inducting into the device through the optical path / waveguide. The area of this region is about 104 m^2 with two floors.
8. NBI region: This region is for placing the NBI system. The area of this region is about 20 m^2 with two floors.
9. Power supply cabinet : The power supply cabinet is placed in the Hall, besides the west wall. It is including power supply cabinet (connect the capacitor) of the coil system, power supply cabinet (connect the capacitor) of the heating system, power supply cabinet (connect city electricity) of the discharge cleaning / wall treatment and so on. These power cabinets are for the device discharge.
10. Others: Some space around the device for placing the vacuum pump, fueling and other equipment.

4.1.2 Room for peripherals

There are two rooms outside the hall, shown in figure 4.1. The Room 1 is for the power supply and the Room 2 is for the water-treatment plant. This arrangement can keep the danger (from the power supply and water-treatment systems) away and ensure the safety of experimenters. Detail descriptions are as following:

1. Room 1 for power supply: This room is in the west of the hall with 23 m in length, 6 m in width and 7.4 m in height. In this room, the energy storage power supply (capacitors, charge / discharge equipment), power debugging equipment (on-site commissioning equipment, fake load, etc.), power control equipment (monitoring, control, protection, grounding, etc.), high-power switching system, etc, are accommodated. A grounding pile system is needed. The energy storage power source region is relatively far away from the weak electric system such as diagnostics, and is physically separated from the device region. The arrangement

should be reasonable.

2. Room 2 for water-treatment plant region: This room is in the north of the hall with 42 m in length, 4 m in width and 4 m in height. The high pressure water cooling system is located in this room. The cooling water uses the deionized water. The consumption of the water is plentiful, so the primary circuit and the secondary circuit should be designed reasonably. In addition, high pressure gas system, which is for the pneumatic vacuum valve, pneumatic probe system and vacuum chamber baking system, is also set in this room.

4.1.3 Control room

The control room is in the Experimental region, as shown in figure 4.1. Because the hall space is limited, the control room is arranged beside function rooms, such as material and data handling rooms. Descriptions of the experimental region is as follows:

There are two floors of this region and each floor is divided into three rooms. On the first floor, there are **Vacuum preparation room** (placing vacuum equipment: leak detector, leak gas, flanges, vacuum sealed devices, cleaning bench/equipment etc.), **Experimental material room** (spare parts, cable, optical fiber, metal material, insulating material etc.) and **Metalworking workshop** (drill, grind, tool, bench, spreader tooling, fastening pieces etc). On the second floor. There are **Data handling room** (including data acquisition, amplifier, integrator, database etc), **Discharge control room** (Monitor and control the device experiment and it is the nerve center of the device with the master control equipment) and **Central laboratory** (Room for experiment co-ordination arrangements and discussion). In the primary plan, the control room is about 50 m^2, if necessary, it can be expanded.

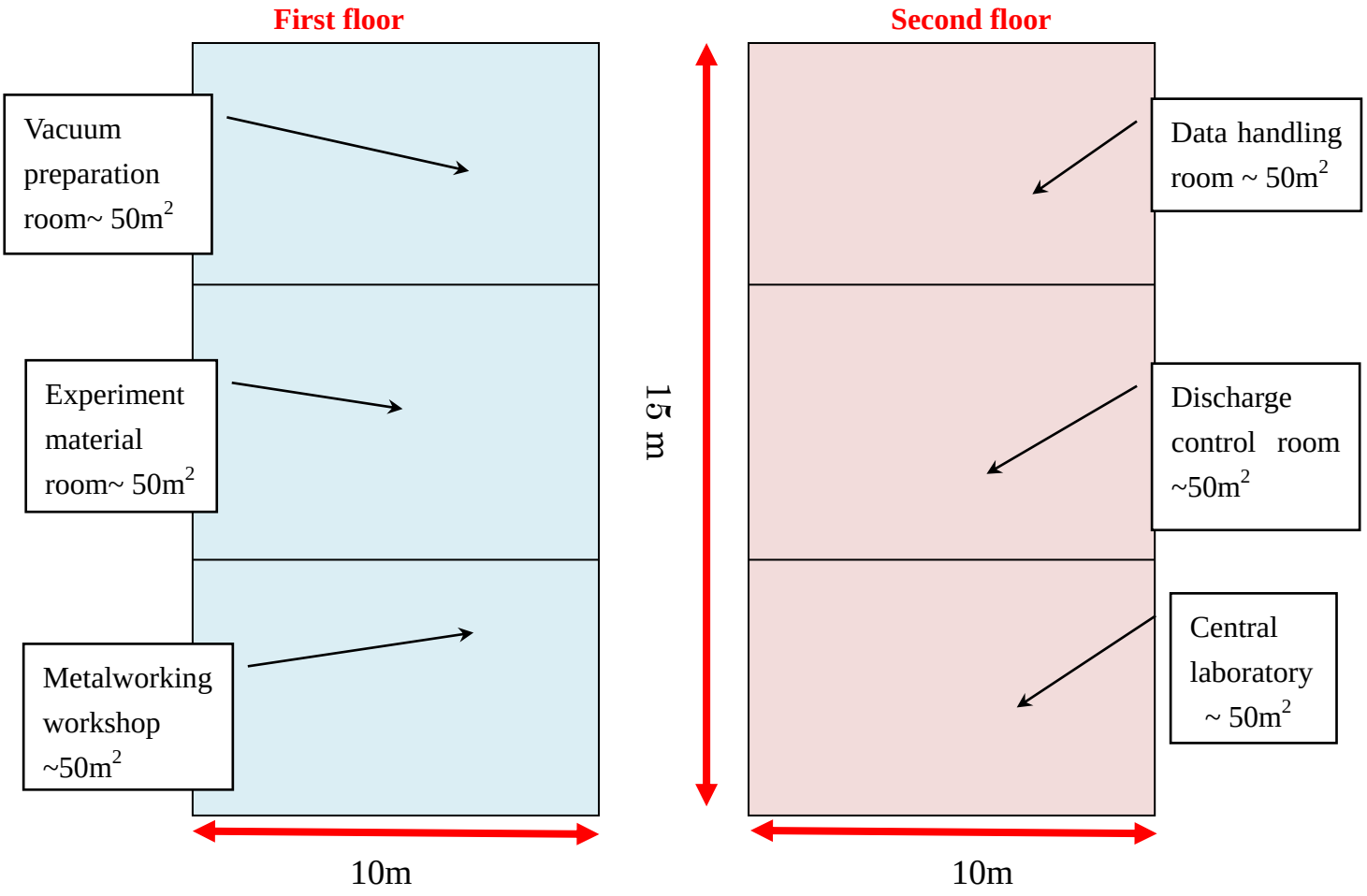

Fig. 4.1.3-1 Two- floor arrangements of the experimental region

4.2 Coil system

4.2.1 Modular coils

Vacuum equilibrium properties of a toroidal configuration are determined by the shape of the outmost closed flux surface (plasma boundary). Generally, considering the nested magnetic flux surfaces, the VMEC code enables to solve the three dimensional MHD equilibrium accurately and efficiently. In order to achieve the target magnetic configuration, a modular coil system is necessary to be designed to reproduce the plasma boundary. Due to the Neumann boundary condition, the accuracy of the magnetic configuration induced by the coil system is dependent on the normal component of the magnetic field on the plasma boundary, which is expressed as where B is the vacuum magnetic field generated from the coil system on the plasma boundary and n is the normal unit vector of this surface. Via the minimization of on the plasma boundary, the modular coil geometry is optimized. Meanwhile, the engineering constraints are taken into account which are the minimum interval between adjacent coils and maximum curvature. They are under consideration to avoid the coil-coil overlap and reduce complexity of the coil shape. This optimization process is accomplished by the NESCOIL code [4.2.1-1]. In the design of the coil system for the CFQS, the coil numbers, major radials and aspect ratio have been scanned to achieve an optimum modular coil system. The corresponding parameters of coil systems are listed in the Table 4.2.1-1. We have designed 10 magnetic configurations and 17 coil systems in total. The toroidal periodic number of all configuration is the same, 2.0. Making a comparison among them, the configuration with the major radius R_0=1.0m, aspect ratio Ap=4.0, magnetic field strength Bt=1.0 T and minor radius a=0.25 m is advantageous. The 20-coil, 16-coil and 12-coil systems are designed respectively. The results of filament-coil optimization are listed in the table 4.2.1-2. In comparison of the physics and engineering constraints among them, the table indicates that the 16-coils system is preferable, which shows that the minimum interval between adjacent filament coils is the widest; the minimum radius of curvature is the largest and the magnetic flux surface generated is the closest to the target surface.

Table 4.2.1-1 Parameters for 10 magnetic configurations designed, showing the configuration with the major radius R_0=1.0m, aspect ratio Ap=4.0, magnetic field strength Bt=1.0 T and minor radius a=0.25 m.

R_0(m)	Ap	a (m)	B_t(T)	Num of modular coils
1.5	3.2	0.47	1.0	20
1.5	3.9(2w39)	0.38	1.0	20
1.5	4.0	0.38	1.0	20
1.5	5.0	0.30	1.0	20
1.2	3.8	0.32	1.0	Ongoing
1.2	4.0	0.30	1.0	24, 20,16,12
1.2	5.0	0.24	1.0	Ongoing
1.0	3.2	0.31	1.0	20,16,12
1.0	3.6	0.28	1.0	20,16,12
1.0	4.0	0.25	1.0	20,16,12
Total	Number of configurations:10		Number of coil systems:17	

Table 4.2.1-2 Parameters of three different types of coil systems for CFQS-2b40.

Ap	R_0 (m)	a (m)	Number of coils	Min. distance between coils (cm)	Min. radius of curvature (cm)	B·n/|B|	Current per coil (MA)	Cross section of coils (cm^2)
4.0	1	0.250	20	17.0	18.2	1.11%	0.2500	17×9
4.0	1	0.250	16	18.5	21.5	0.97%	0.3125	18×10
4.0	1	0.250	12	14.2	14.7	1.21%	0.4167	19×13

The following figure gives the of 16-modular coil system. Due to the toroidal periodicity=2 and stellarator symmetry, the whole torus consists of four symmetric sections. Therefore, the coils system possesses four different shaped modular coils. The centerline of each finite sized coil is assigned by the corresponding filament coil. The all

16 filament coils are from the results of the NESCOIL code. The coil cross section is rectangular and the area is 18×10 cm^2 which includes copper conductor, insulation and coil casing.

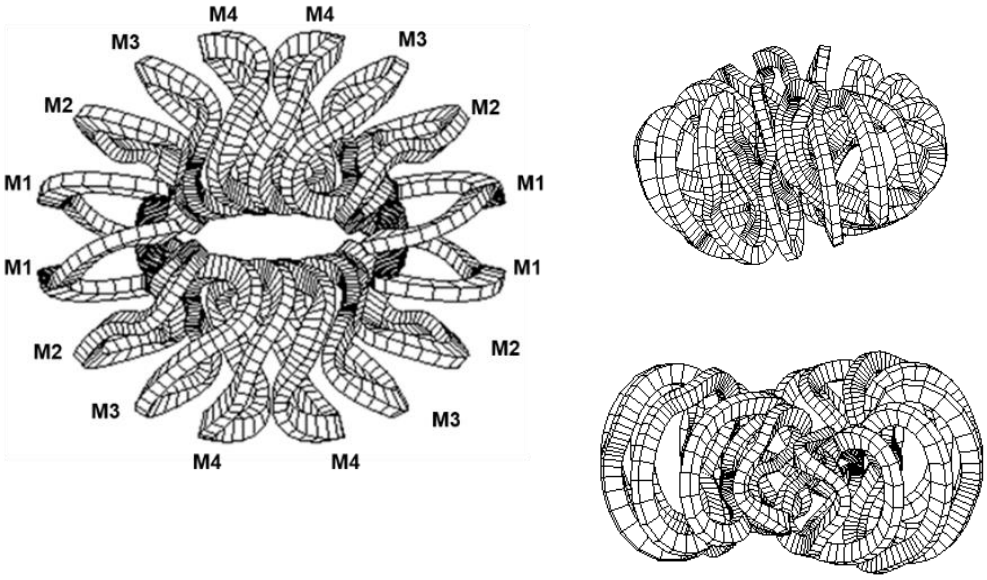

Fig. 4.2.1-1 Modular coils of the CFQS, the top view and side views at toroidal angle=0^o (vertical elongation), and 90^o (horizontal elongation). The serial number of coils represents the various shapes of coils. The coil system comprises of four different shape coils.

In order to estimate the accuracy of the magnetic configuration induced by the 16-coil system, the coils generated magnetic flux surfaces, rotational transform and Fourier spectrum of the magnetic field strength are calculated. In the Fig. 4.2.1-2, Poincaré plots of magnetic flux surfaces and rotational transform induced by the modular coils are analyzed, assuming the coils are filament ones. At the toroidal angle= 0^o, 45^o and 90^o, cross sections are displayed. The angle = 0^o and 90^o correspond to the vertically and horizontally elongated cross sections, respectively. The average of $\mathbf{B} \cdot \mathbf{n} / |\mathbf{B}|$ on the plasma boundary is below 1%, which cannot be reduced from the viewpoint of the engineering. The rotational transform profile and magnetic well induced by coils and target profile are compared in the Fig. 4.2.1-2(d). Horizontal axis ρ in this figure represents the normalized average minor radius. The figure shows a good agreement between coils induced rotational transform profile and depth of magnetic well and target ones. From the Fig. 4.2.1-2(a)-(c), they depict a good coincidence in the shapes of a magnetic flux surface and that of target plasma boundary. It should be noted that the width of outmost flux surface produced by modular coils is larger than that of target

plasma boundary, which is beneficial to raise the plasma volume by movable limiters. In order to precisely estimate the quasi-axisymmetry of the configuration, the magnetic field strength is decomposed into a Fourier spectrum in the Boozer coordinates. The Fig. 4.2.1-3.(a) depicts the spectrum of the magnetic field strength based on the the target magnetic configuration. To extinguish the small-amplitude components, the largest component B_{00} is omitted. In the Fig. 4.2.1-3.(a), the magnetic field strength is 1.0 T. B_{10} is the dominant component resulting from the toroidicity. Others components, such as mirror ripple (B_{01}) and helical ripples (B_{11}, B_{12}), are much less than B_{01}, which indicates a tokamak-like/quasi-axisymmetric configuration. In the Fig. 4.2.1-3.(b), coil induced spectrum of magnetic field strength is given. On the basis of synthetical analyzation, the designed 16-coil system is well workable.

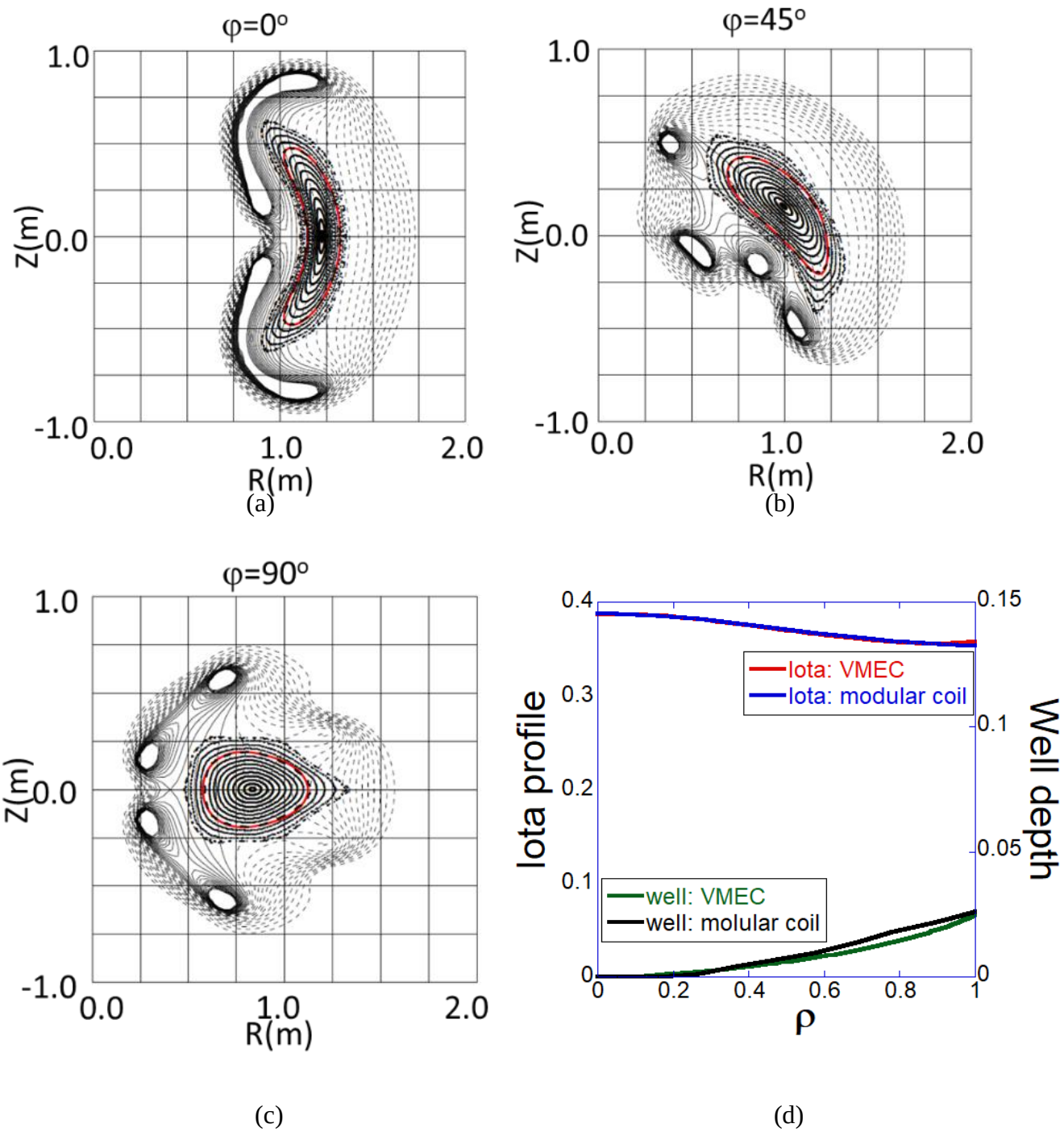

Fig. 4.2.1-2 Poincaré plots of magnetic flux surfaces at the toroidal angle =0°, 45° and 90° for (a)-(c) respectively. The red curve represents the target plasma boundary. (d) shows the comparison of the rotational transform and magnetic well between the configuration produced by modular coils and target one.

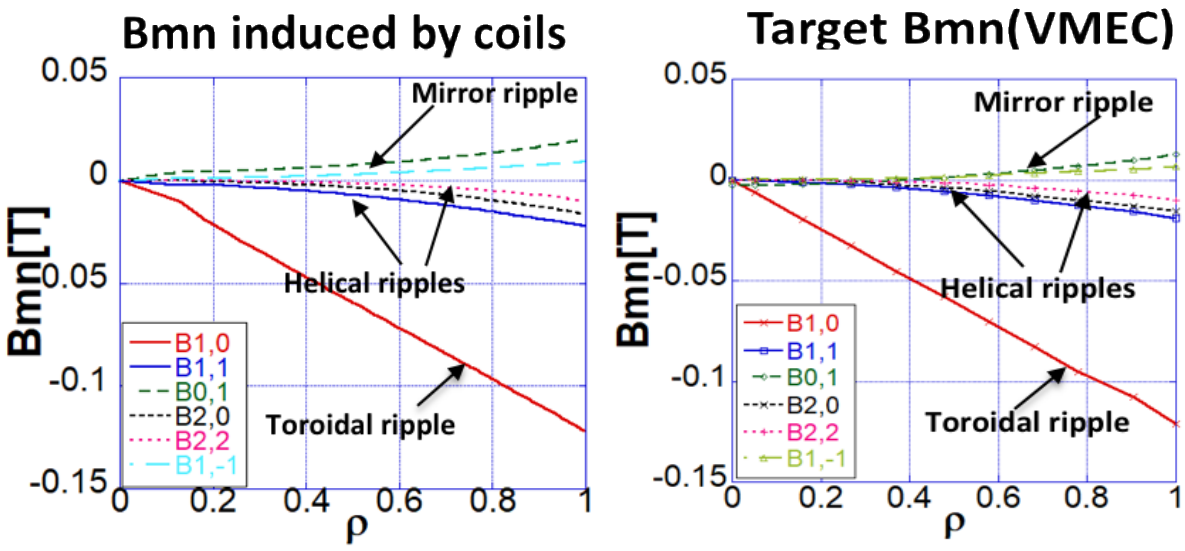

(a) (b)

Fig. 4.2.1-3 Fourier spectrum of the magnetic field strength for the CFQS configuration in the Boozer coordinates. (a) Bmn from VMEC results (target spectrum), (b) Bmn generated by modular coils.

References

[4.2.1-1] M. Drevlak, Fusion Technol **33** (1998) 106.

4.2.2 Poloidal field coils

4.2.3 Auxiliary toroidal field coils

4.2.4 Trim coils

4.2.5 Electromagnetic force analysis and supporting structure

(1)Purpose of electromagnetic force analysis

The main load acted on the modular coil is EM force, if we want to design the coils support , first of all the EM force value and direction is needed to know, and then we can carry out the support design. So the preliminary EM analysis has been performed.

(2)Parameter of modular coil

Toroidal magnetic field of modular coil is about 1 tesla, toroidal period number is 2, and major radius is 1m. The detailed parameters as the follow table are shown.

Table 4.2.5-1 Parameters of modular coil

configuration	Bt(T)	N	R（m）	a (m)	Qty.of coils	Min. dist. (mm)	Min. radius (mm)	B dot n/|B|	Cross section (mm^2)
2b40	1	2	1	0.25	16	185	215	0.97%	180×100

There are 4 types of modular coil: M1 coil, M2 coil, M3 coil and M4 coil. The total quantity of modular coil is 16. The following figures show the configuration of the modular coil.

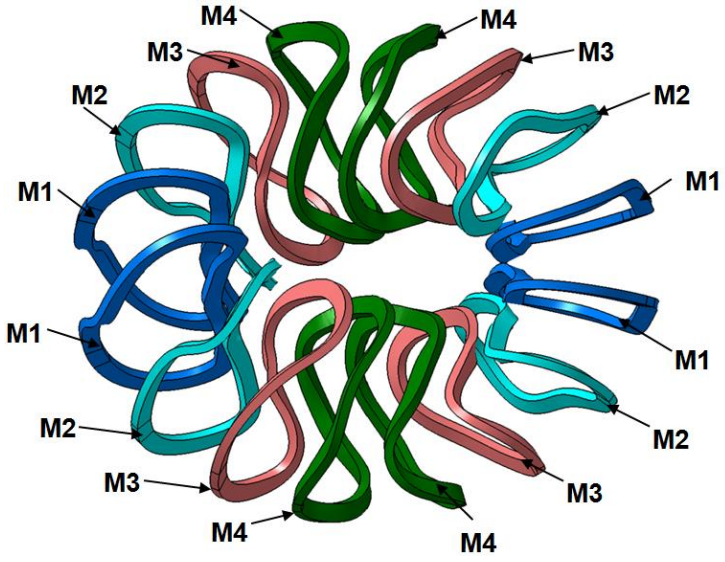

Fig. 4.2.5-1 4 types of modular coil

（3） 3D finite element model and boundary conditions for electromagnetic force analysis

- 16 currents for 16 modular coils, each coil current is 312.5 kA, and each current direction is same and perpendicular with the coil cross section.
- Material of coil is copper, relative permeability is 0.999991, and bulk conductivity is 5.8×10^7 siemens/m
- The 3D finite element model and meshing as the follow figures shown.

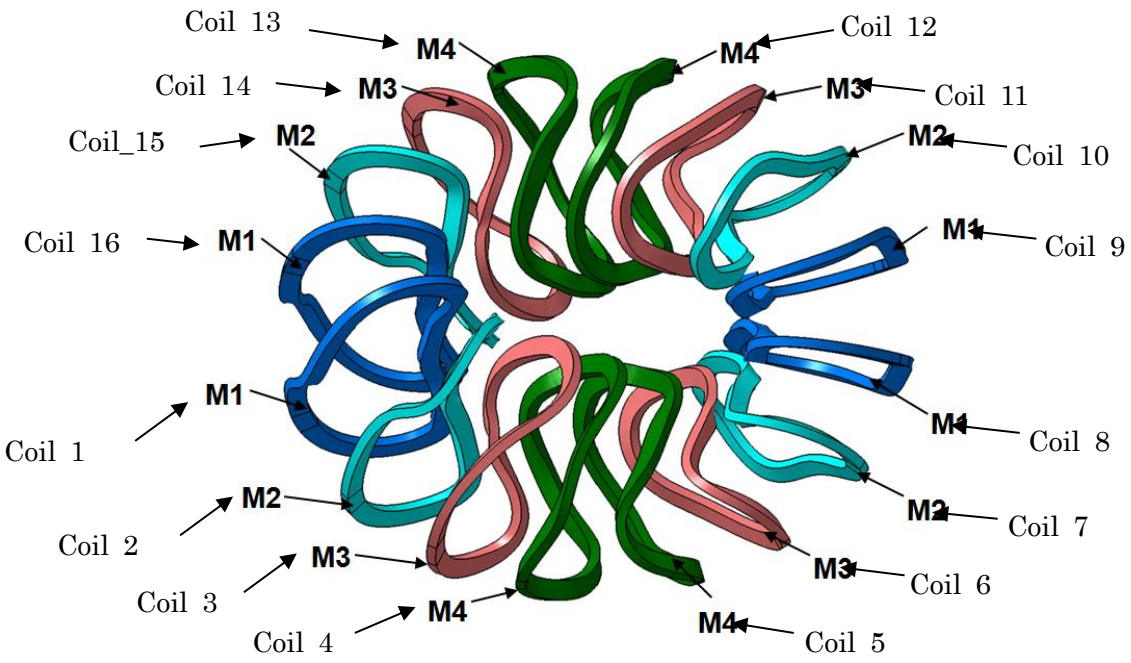

Fig. 4.2.5-2 Numbering of the modular coil

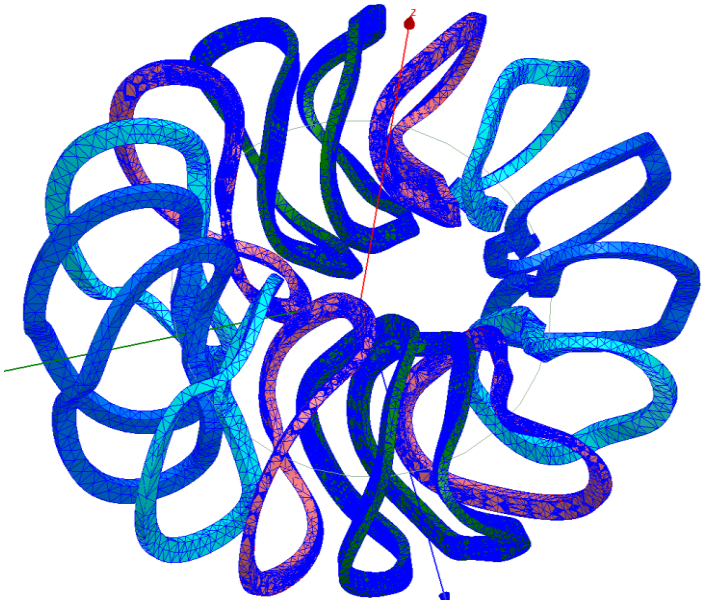

Fig. 4.2.5-3 Meshing 3D finite element model for EM force analysis

(4) Electromagnetic analysis results

- Magnetic field analysis result of the modular coil
  - Maximum magnetic filed of the modular coil

The analysis result shows that the maximum magnetic field of modular coil is about 2.5 tesla, and the maximum magnetic field location is the inner face of the modular coil, as follows.

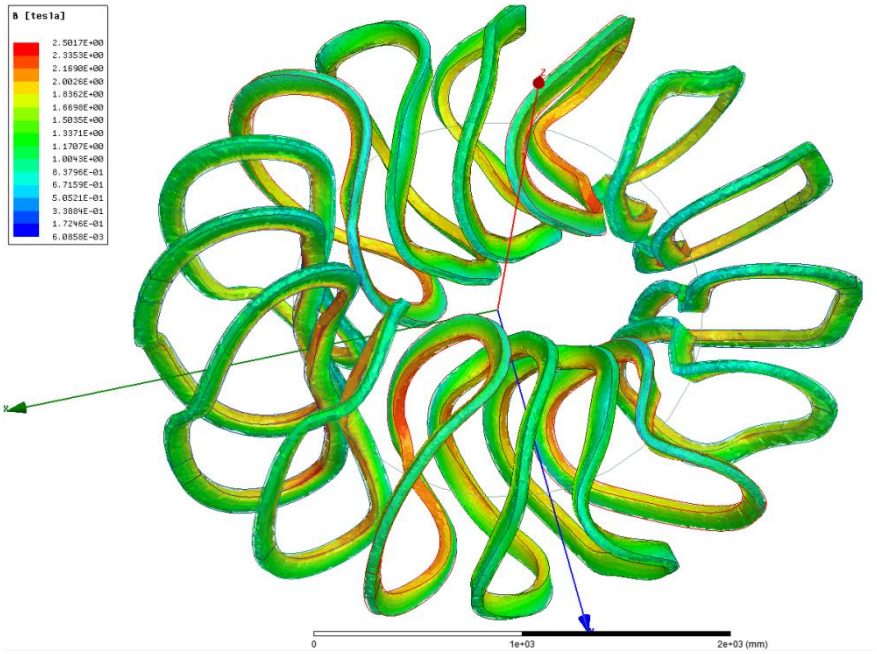

Fig. 4.2.5-4 Magnetic field analysis result of the modular coil

- Magnetic filed analysis result of the 1-meter radius region.
  The design target magnetic filed on R=1m region B_t is about 1 tesla.
  The analysis result shows that the maximum magnetic field of the 1-meter radius region is about 1.39 tesla. But 1.39 tesla just located on a small area and very close to the M1 modular coil inner face, a lot of area of R=1 region magnetic filed is about 1 tesla, as the follow picture shown.

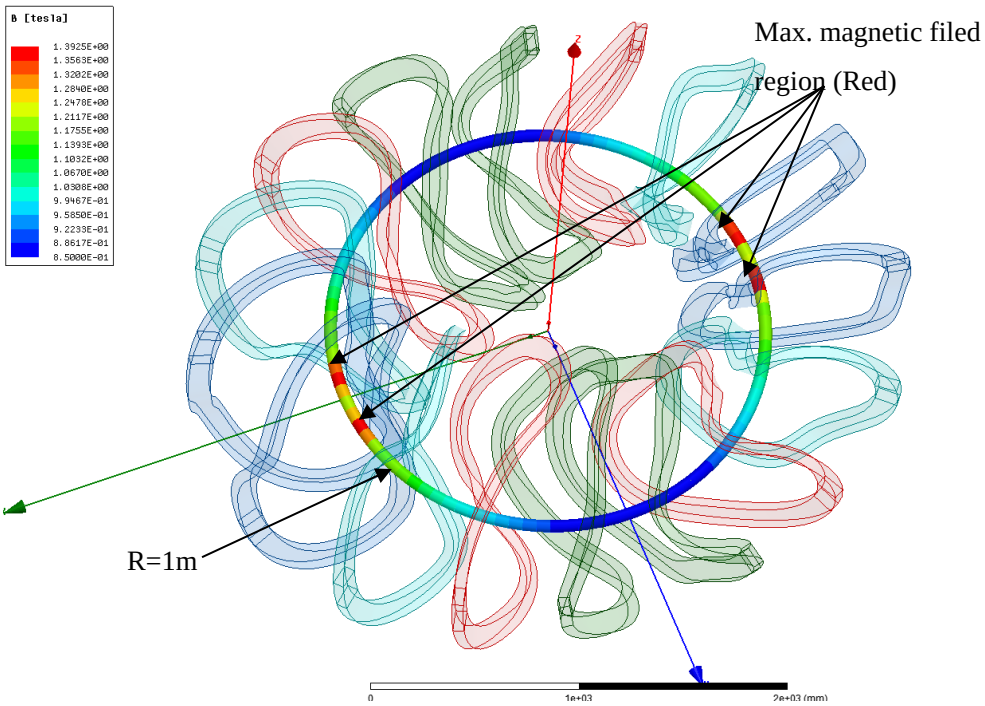

Fig. 4.2.5-5 Magnetic field analysis result of the 1-meter radius region

- Electromagnetic force analysis result of the modular coil
  - EM force volume density and direction of the 16 coils

    The EM force volume density and direction of the 16 coils is shown as the follow pictures. The maximum EM force volume density is about 1.44×10^8 N/m^3.

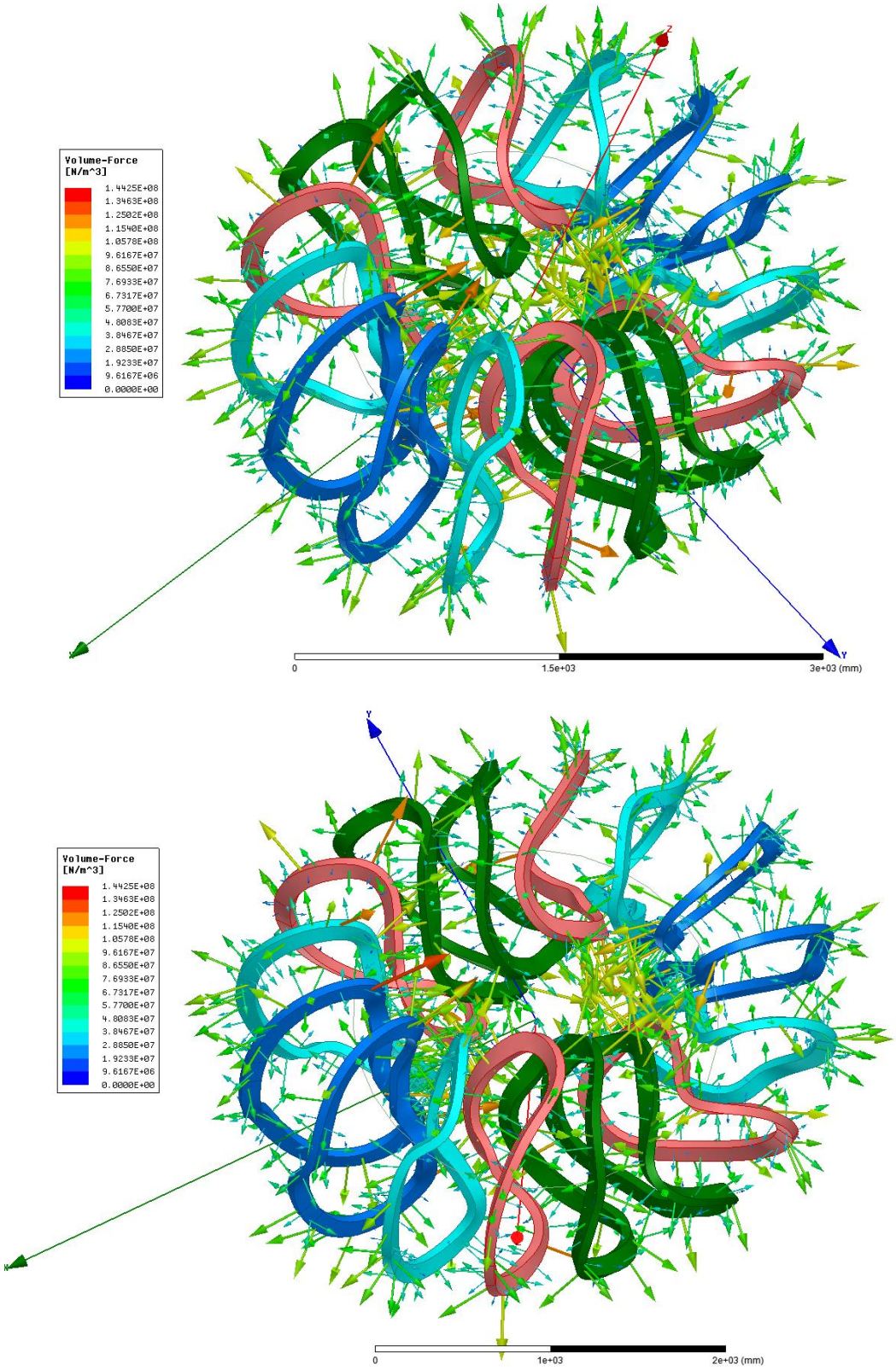

Fig. 4.2.5-6 EM force volume density and direction of the 16 coils

➢ EM force and direction of the 16 coils

The EM force direction and value of Coil_1(M1) is shown as the follow figures respectively. The total EM force of Coil_1(M1) is about 16.74 ton.

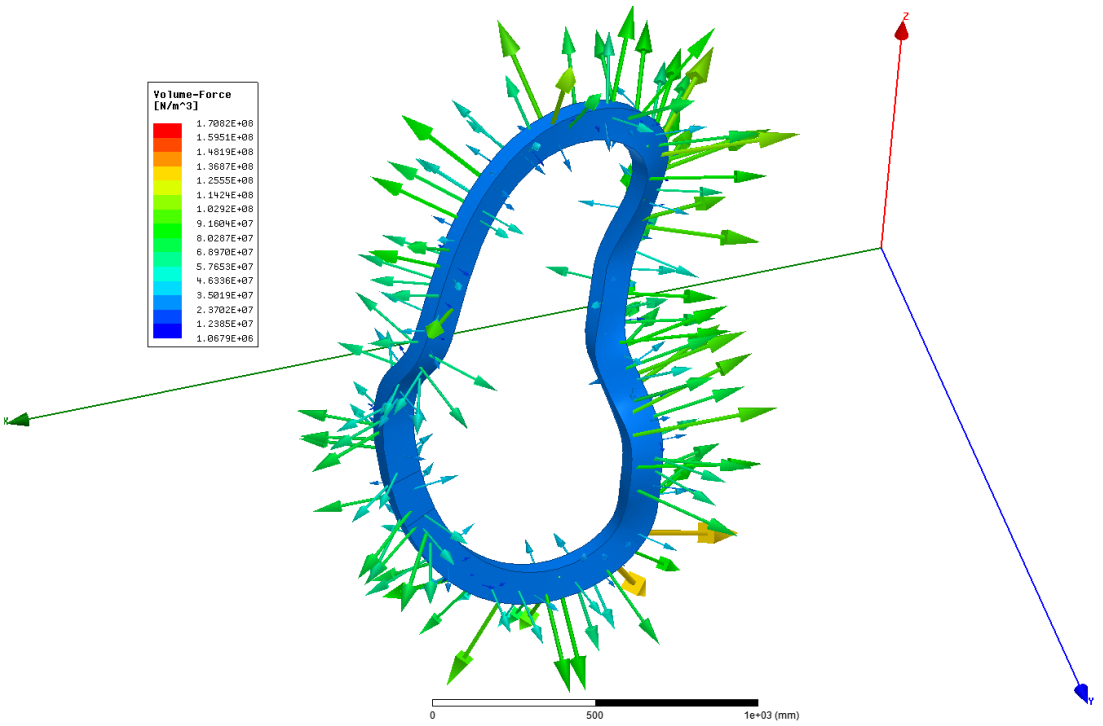

EM force of Coil_1 (M1)Coil （Unit：Ton）			
F_X	F_Y	F_Z	F_{Total}
-15.99	-4.52	-2.02	16.74

Fig. 4.2.5-7 EM force volume density and direction of coil 1

The EM force direction and value of Coil_2(M2) is shown as the follow figures respectively. The total EM force of Coil_2(M2) is about 15.53 ton.

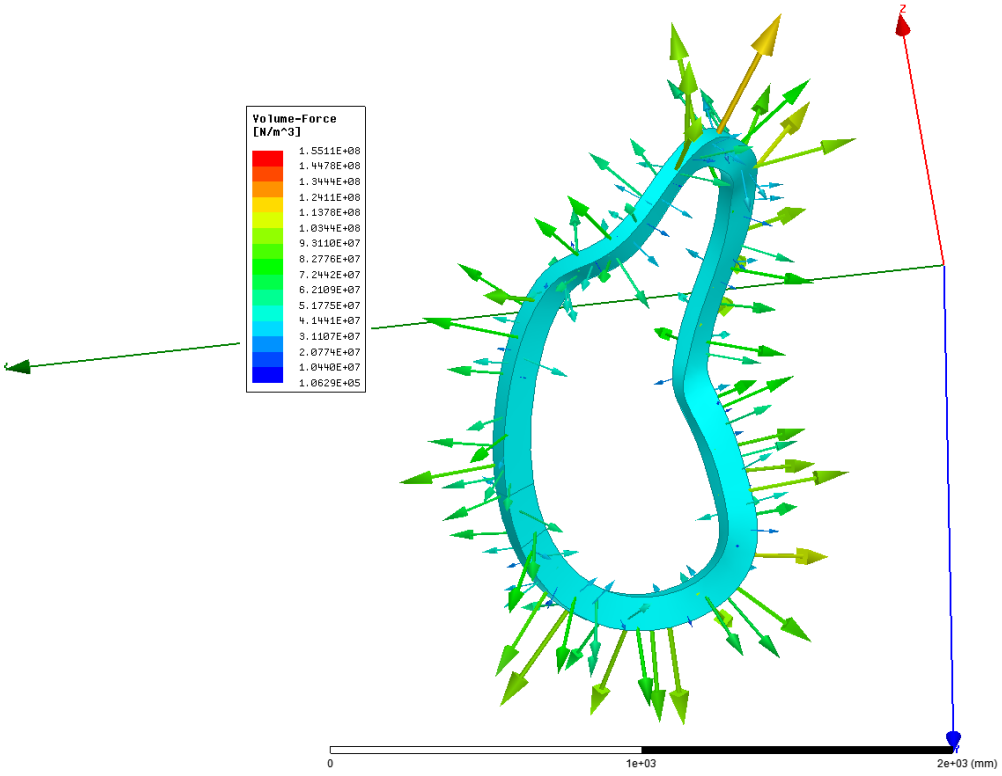

EM force of Coil_2 (M2) Coil （Unit：Ton）			
F_X	F_Y	F_Z	F_{Total}
-9.97	-10.30	-5.97	15.53

Fig. 4.2.5-8 EM force volume density and direction of coil 2

The EM force direction and value of Coil_3(M3) is shown as the follow figures respectively. The total EM force of Coil_3(M3) is about 13.27ton.

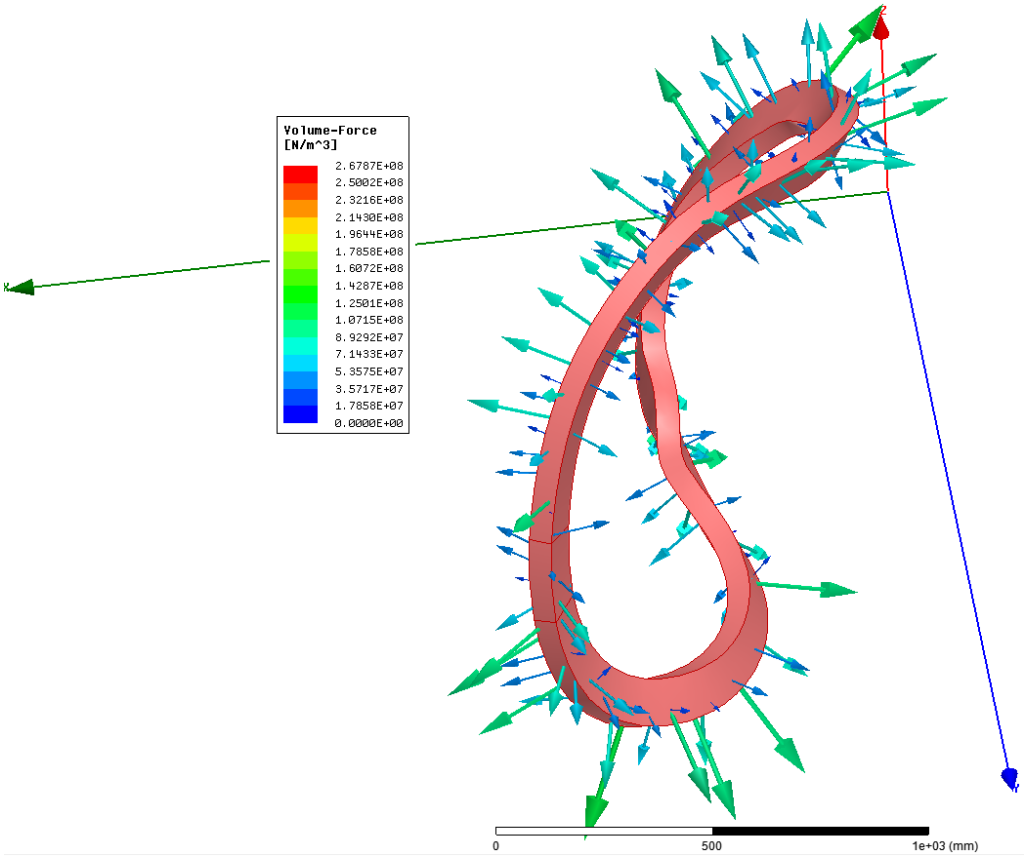

EM force of Coil_3 (M3) Coil （Unit：Ton）			
F_X	F_Y	F_Z	F_{Total}
-2.65	-9.43	-8.95	13.27

Fig. 4.2.5-9 EM force volume density and direction of coil 3

The EM force direction and value of Coil_4(M4) is shown as the follow figures respectively. The total EM force of Coil_4(M4) is about 6.90 ton.

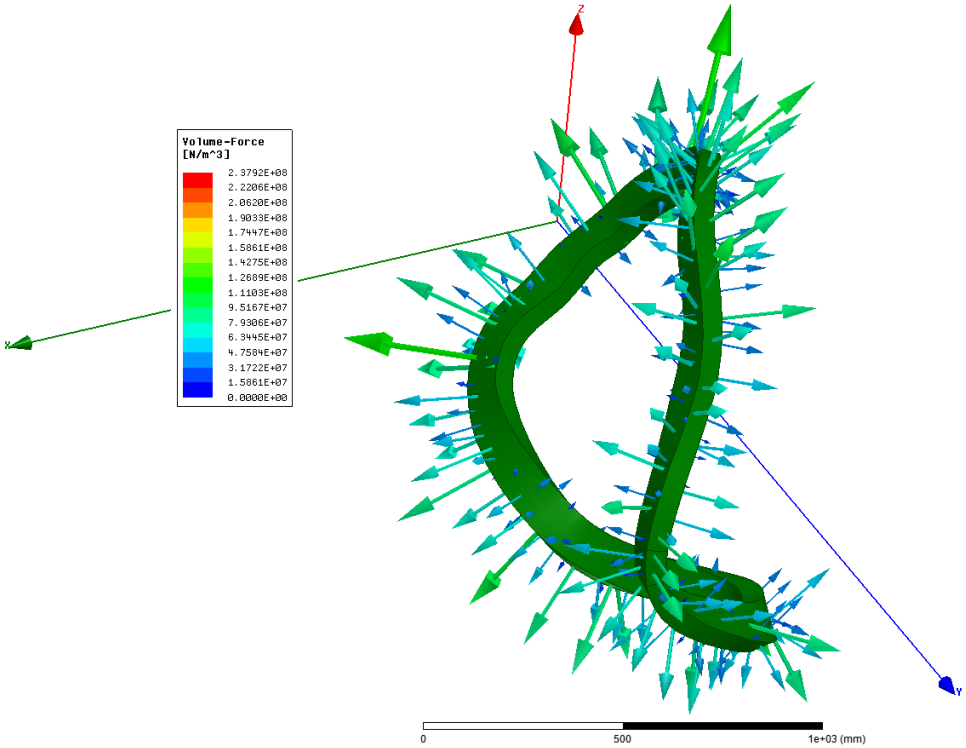

EM force of Coil_4 (M4)Coil （Unit：Ton）			
F_X	F_Y	F_Z	F_{Total}
3.41	-4.62	-3.83	6.90

Fig. 4.2.5-10 EM force volume density and direction of coil 4

The EM force direction and value of Coil_5(M4) is shown as the follow figures respectively. The total EM force of Coil_5(M4) is about 6.92 ton.

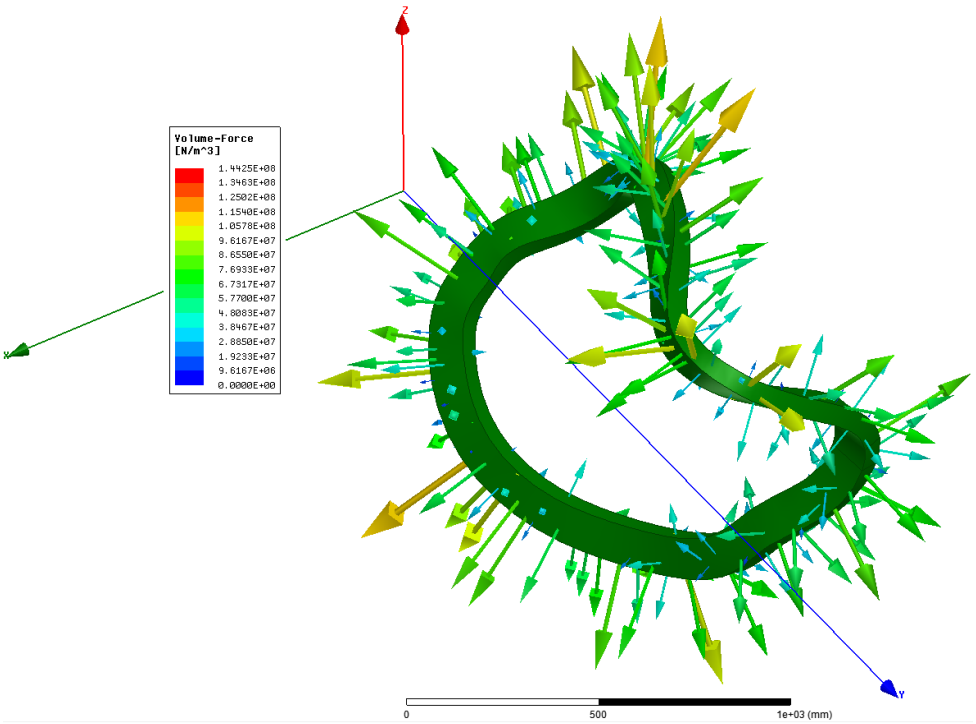

EM force of Coil_5 (M4) Coil （Unit：Ton）			
F_X	F_Y	F_Z	F_{Total}
-3.4	-4.64	3.84	6.92

Fig. 4.2.5-11 EM force volume density and direction of coil 5

The EM force direction and value of Coil_6(M3) is shown as the follow figures respectively. The total EM force of Coil_6(M3) is about 13.27 ton.

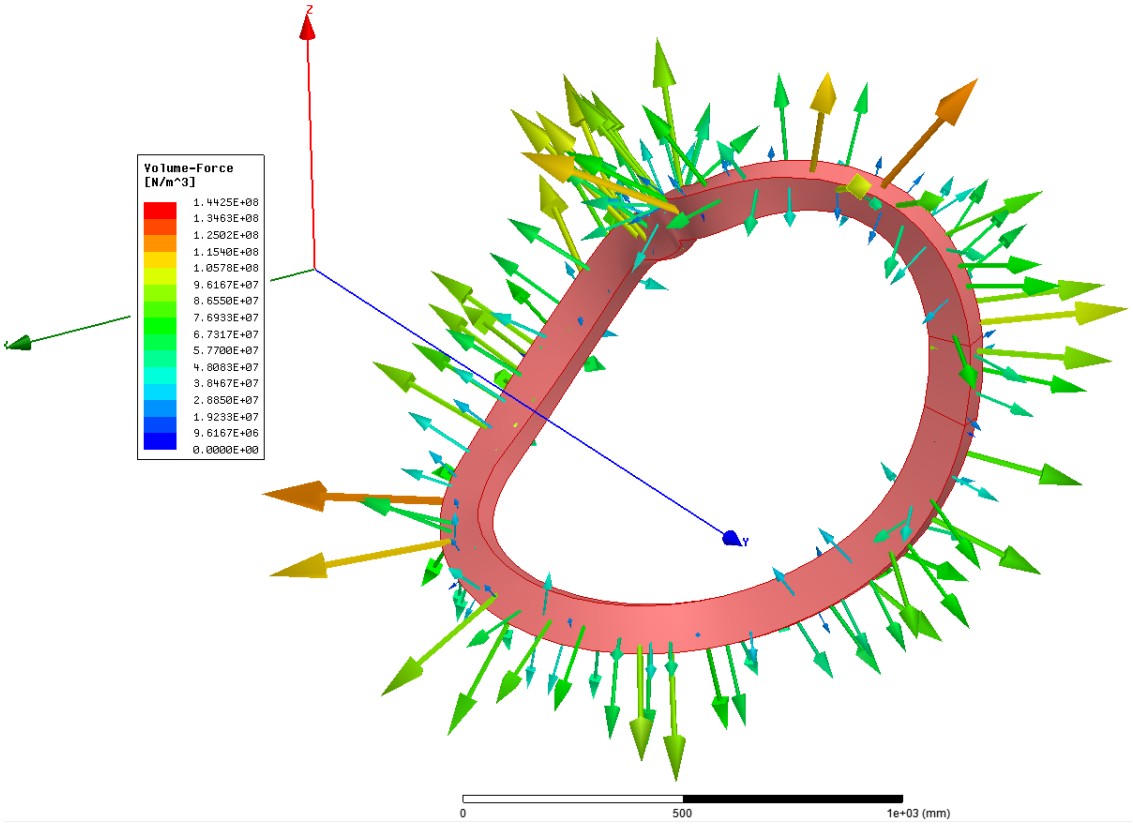

EM force of Coil_6 (M3) Coil （Unit：Ton）			
F_X	F_Y	F_Z	F_{Total}
2.65	-9.42	8.96	13.27

Fig. 4.2.5-12 EM force volume density and direction of coil 6

The EM force direction and value of Coil_7(M2) is shown as the follow figures respectively. The total EM force of Coil_7(M2) is about 15.55 ton.

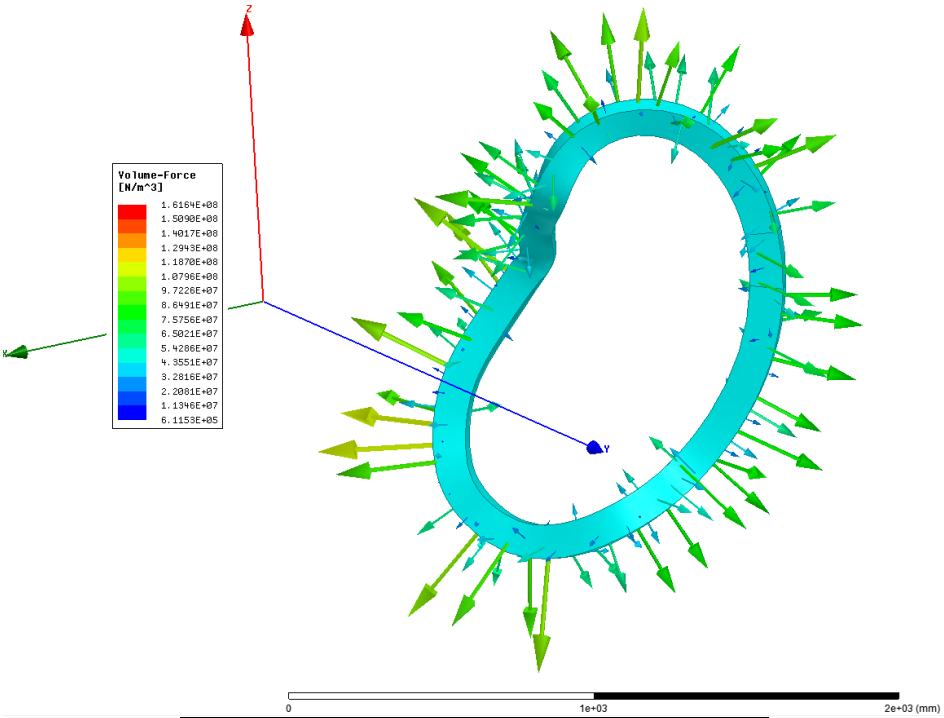

EM force of Coil_7 (M2) Coil （Unit：Ton）			
F_X	F_Y	F_Z	F_{Total}
9.90	-10.41	5.97	15.55

Figure 4.2.5-13 EM force volume density and direction of coil 7

The EM force direction and value of Coil_8(M1) is shown as the follow figures respectively. The total EM force of Coil_8(M1) is about 16.62 ton.

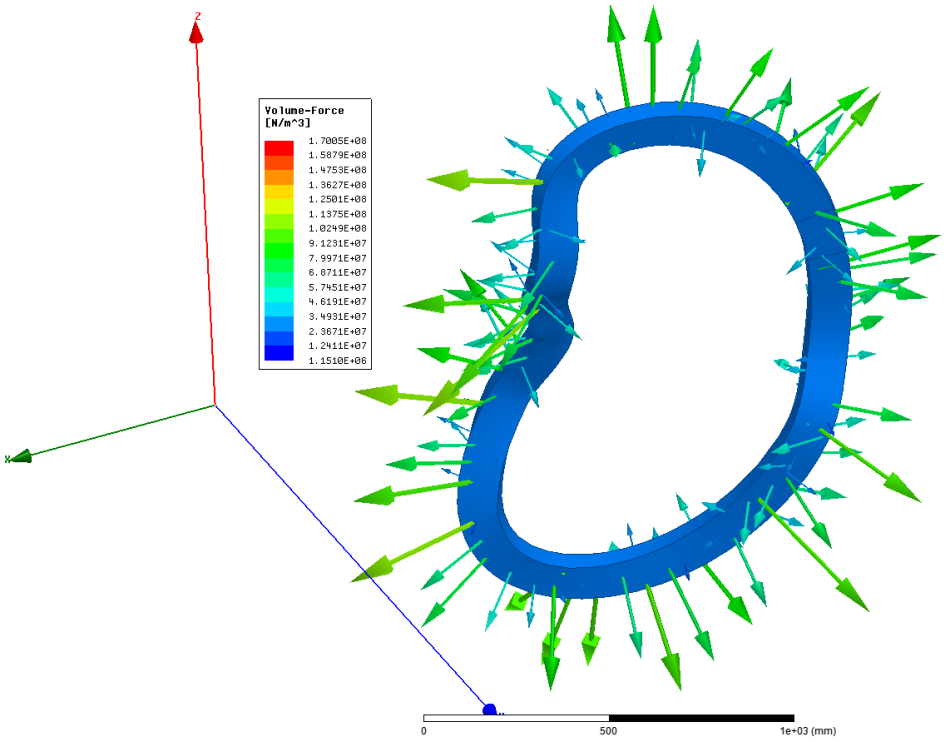

EM force of Coil_8 (M1)Coil （Unit：Ton）			
F_X	F_Y	F_Z	F_{Total}
15.91	-4.36	1.95	16.62

Figure 4.2.5-14 EM force volume density and direction of coil 8

➢ Summary of the EM force of the 16 coils

The follow picture shows the numbering of 16 coils, and the electromagnetic force of the 16 coils as the follow table shown.

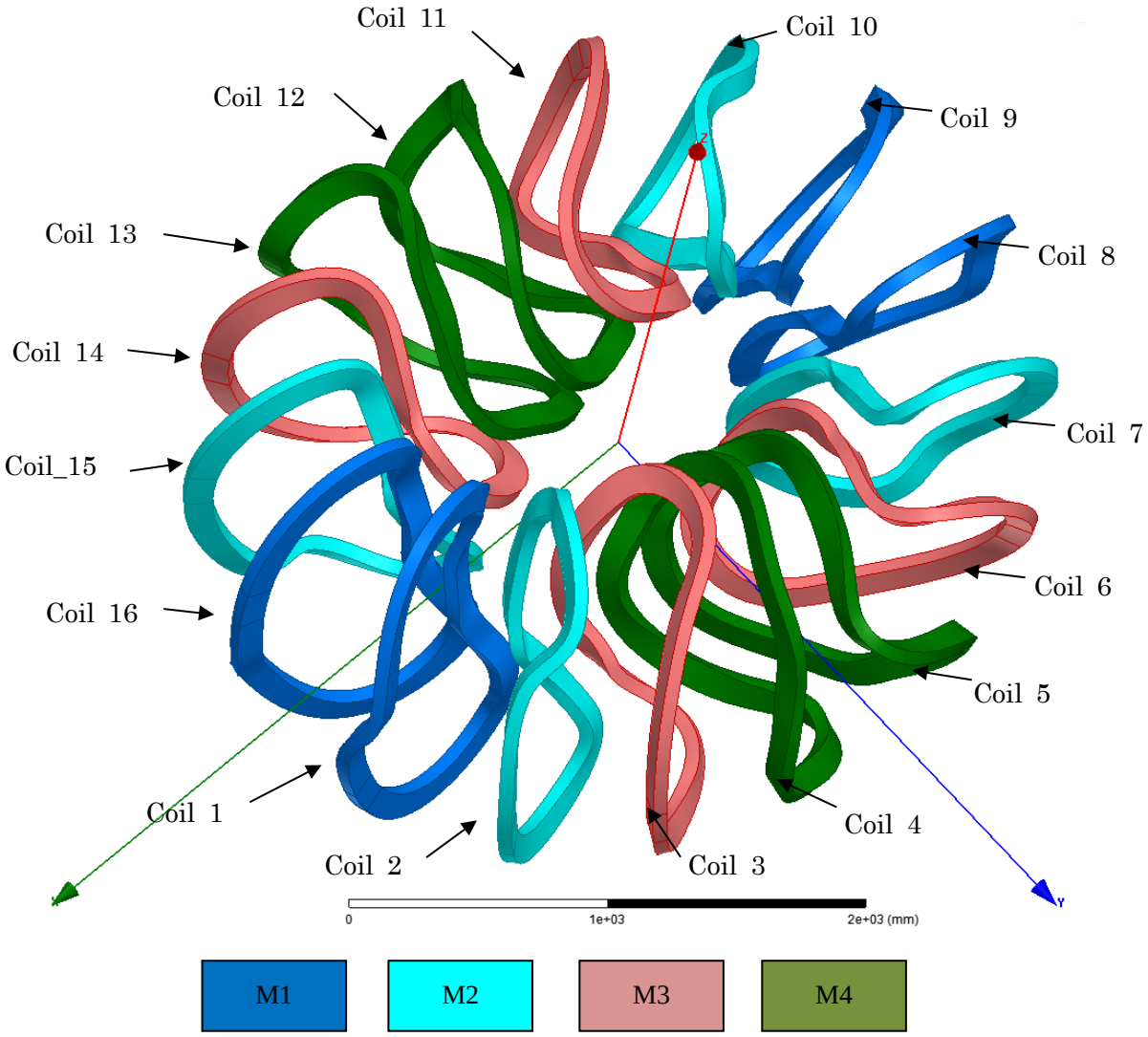

Fig. 4.2.5-15 The numbering of 16 coils

Table 4.2.5-1 EM force of 16 coils

EM force of 16 Coils （Unit：Ton）									
Coil No.	F_X	F_Y	F_Z	F_{Total}	Coil No.	F_X	F_Y	F_Z	F_{Total}
Coil_1	-15.99	-4.52	-2.02	16.74	Coil_16	-15.98	4.25	1.94	16.65
Coil_2	-9.97	-10.30	-5.97	15.53	Coil_15	-9.93	10.36	5.93	15.53
Coil_3	-2.65	-9.43	-8.95	13.27	Coil_14	-2.67	9.48	8.99	13.33
Coil_4	3.41	-4.62	-3.83	6.90	Coil_13	3.39	4.63	3.83	6.90
Coil_5	-3.4	-4.64	3.84	6.92	Coil_12	-3.40	4.62	-3.81	6.89
Coil_6	2.65	-9.42	8.96	13.27	Coil_11	2.64	9.45	-8.99	13.31
Coil_7	9.90	-10.41	5.97	15.55	Coil_10	9.81	10.27	-5.96	15.40
Coil_8	15.91	-4.36	1.95	16.62	Coil_9	15.92	4.33	-1.94	16.61

From the table of EM force of 16 coils, we can get the conclusion that the final total EM force direction is centripetal.

(5) Modular coil support design

Base on the electromagnetic force analysis of the modular coil, the preliminary conceptual design has been finished. The modular coil support mainly include 3 types of support: main structural support, coils support plate and ring support, as the follow picture shown.

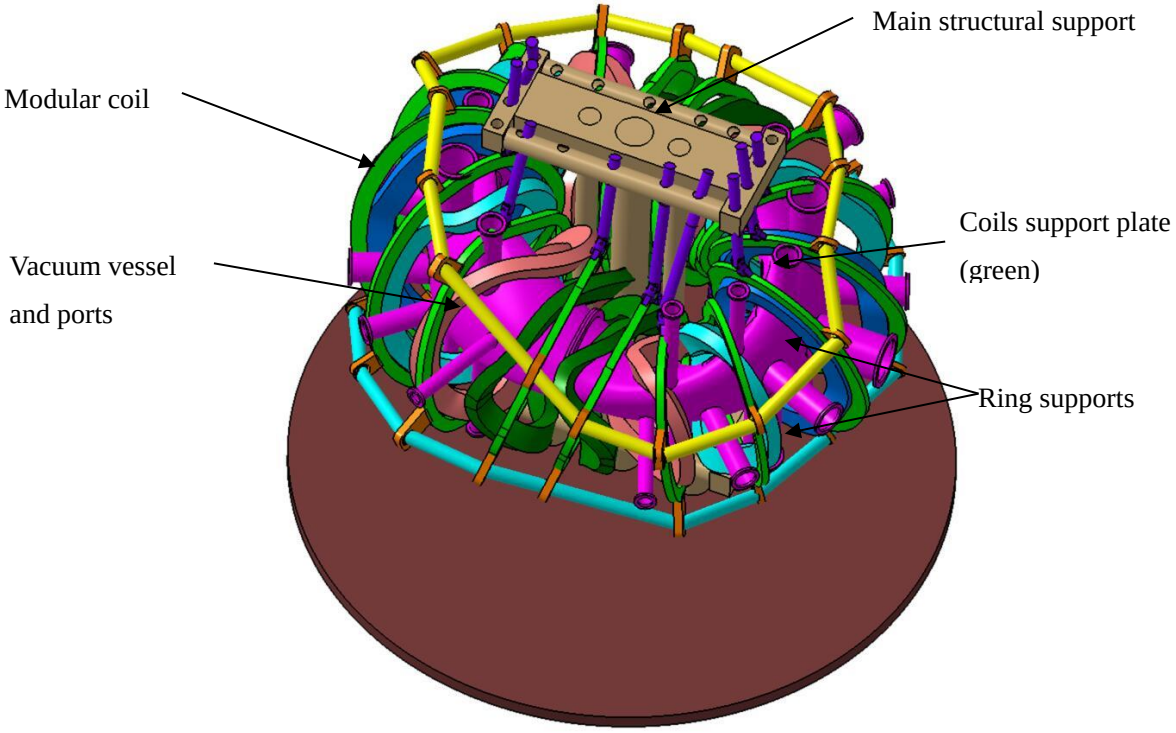

Fig. 4.2.5-16 Modular coil support

Main structural support locate in the center of the modular coil which is used to bear the total centripetal EM force and support the modular coil.

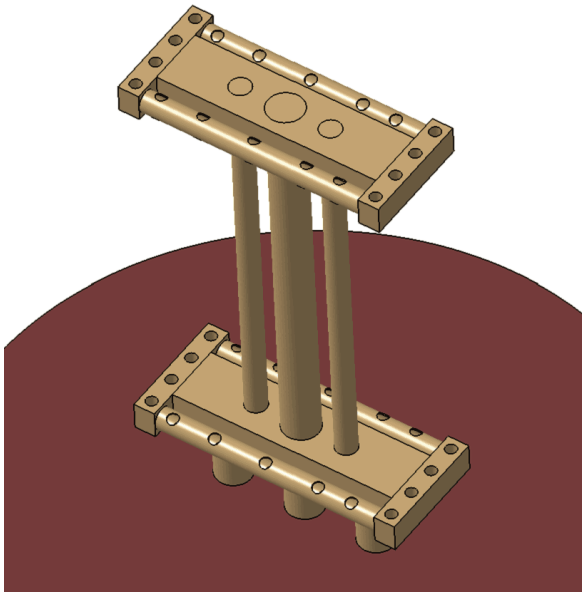

Fig. 4.2.5-17 Main structural support

The electromagnetic force analysis indicate that each coil suffer a EM force, which direction is toward outside of the coil, the coils support plates are used to bear coil EM force and support the coils.

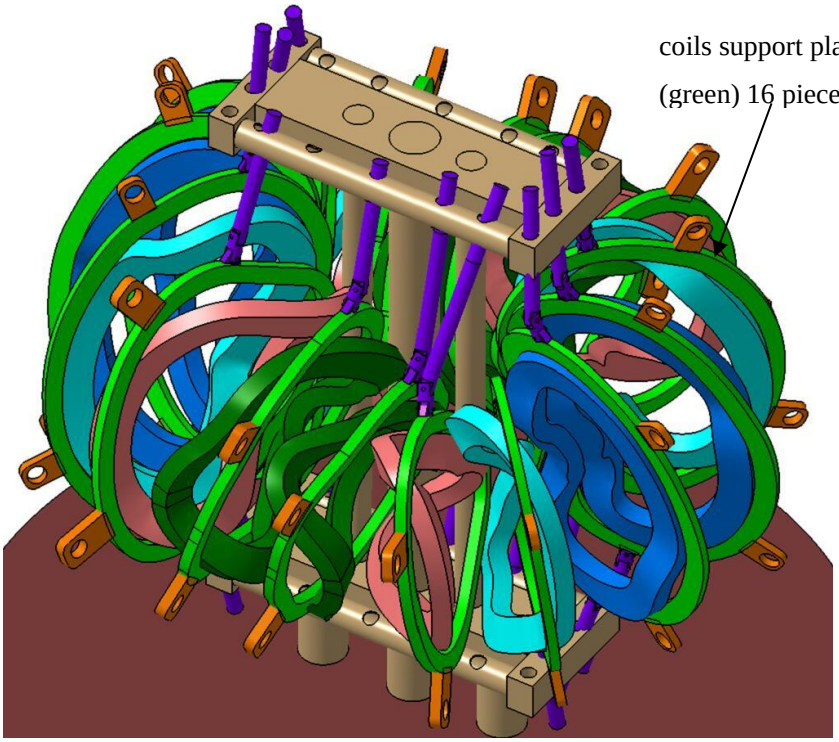

Fig. 4.2.5-18 Coils support plates

The ring supports are designed to combine the modular coils together and bear the EM force between each single coil.

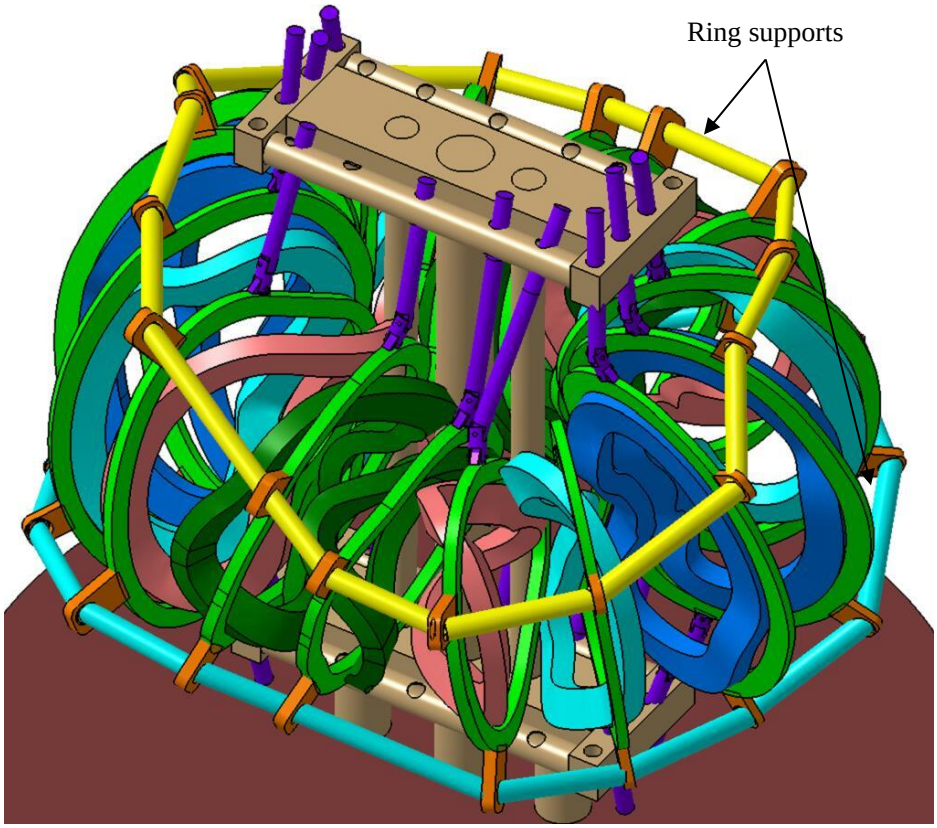

Fig. 4.2.5-19 Ring supports

4.3 Vacuum vessel

4.3.1 Main vessel

4.3.1.1 Design Requirement

Vacuum vessel is the main part of CFQS, plasma operate inside of chamber inner space directly, the requirement of plasma spatial form and location must be ensured, as to provide the fine vacuum environment of plasma operating;

For this integrated system, diagnosis and experiment demand high penetration rate, as well as various kinds of interfaces: such as heating, pumping, NBI, injection, maintenance and supporting systems.

The structure of vacuum vessel shall be strong enough to withstand the electromagnetic force which create by interaction between vortex and magnetic field.

Additional, barometric pressure and gravity shall be considered, the thermal stress created by temperature gradient from baking process as well.

With regards to the vacuum vessel structure, good performance of conductivity, fine vacuum, appropriate loop resistance and adequate supporting strength are all required, to satisfied with the operating requirement of physics and engineering.

Table 4.3.1.1-1 Vacuum Vessel Parameters

VV Parameters	
Vacuum Degree	$<2\times10^{-5}$ Pa
Whole Leak Rate	5×10^{-5} Torr.L/s
Toroidal Resistance	>1 mΩ
Plasma Temperature	$T_{e0}=T_{i0}=1$ keV for $n_{ebar}=2.0\times10^{19}$ m^{-3} $T_{e0}<6$ keV for $n_{ebar}<1.0\times10^{19}$ m^{-3}
Plasma Duration	<200 ms
baking temperature	150 °C
Temperature rising	5 °C/h for baking
Seismic Acceleration	0.33 G,~350 gal= cm/s^2

4.3.1.2. Overall Structure Design

Single layer plate type and circular structure is recommended;

The entire ring-shape is welded together by several separate sections, and flange connected;

Interface/window such as vacuum pumping, plasma diagnosis, NBI shall be considered and reserved; and all interfaces shall be arranged as symmetrical

distribution, and according to the actual demand, the range of interface diameter is Φ50 mm~Φ300 mm;

The raw material of chamber wall is proposed as SS316L, for low magnetic permeability ($\mu \leq 1.01$), and this material is not so sensitive to thermal cycling/deformation, weld-ability and gas-rate are all satisfied with vacuum chamber requirement;

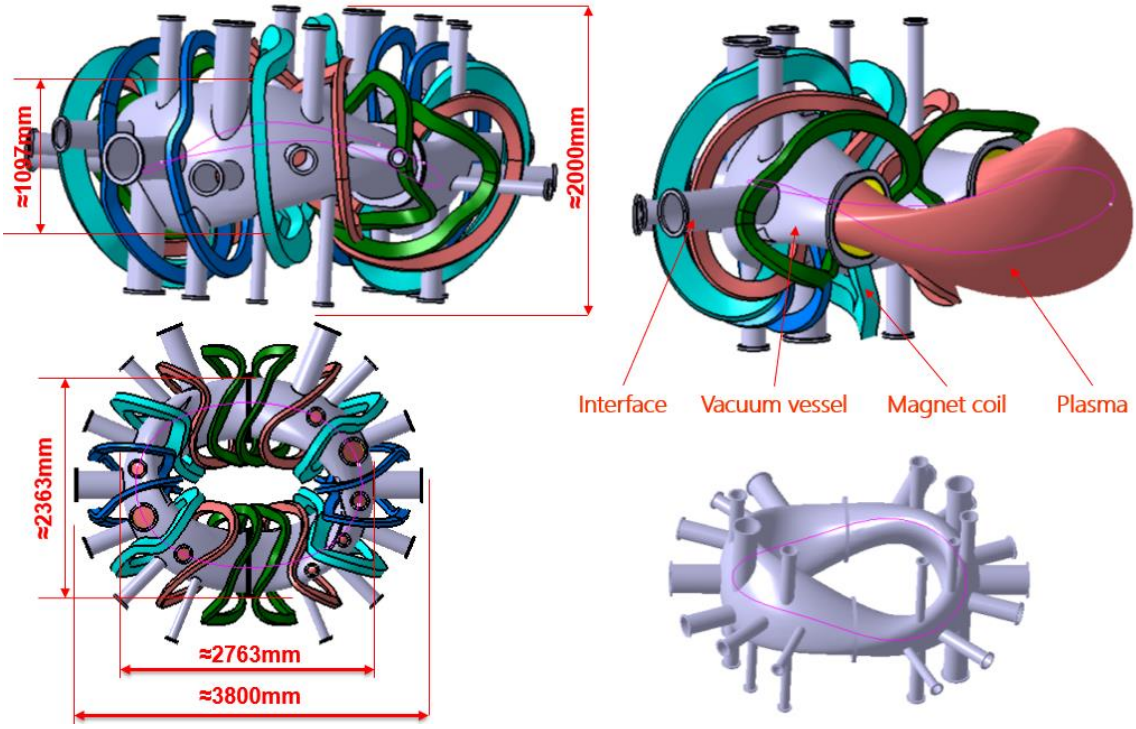

Fig. 4.3.1.2-1 Overall structure of vacuum vessel

4.3.1.3. Detailed structural design

Base on overall structure design, detailed design of the vacuum vessel is required.

1) Material for Main Body

Requirement of main material:

- high comprehensive mechanical properties, adequate capacity for gravity of self and internal parts, atmospheric pressure, thermal load, electromagnetic force.
- High resistivity;
- Low magnetic conductivity;
- Low material out-gassing rate is required for ultra-high vacuum environment;
- Machinability and weldability are required for irregular cross-section and welded construction;

- Economy and reliability;

Selection of VV main body material is one important consideration in the design phase; based on overall consideration, SS 316L stainless steel is recommended for the CFQS VV main body.

Table 4.3.1.3-1 Mechanical property of SS 316L

Temperature	Young Modulus	Yield Strength	Ultimate Strength	Ductility
300 K	>190 GPa	>170 MPa	>480 MPa	>35 %

4.3.1.4. The dimensions of VV

According to relevant experience, CFQS VV is single layer, thin wall, welded structure, which is similar to the shape of the magnetic field configuration.

4.3.1.5. Subsection of VV

Based on optimization of technology and assembly accuracy, vacuum vessel is divided into two sections, connected by flanges; Separated location is at the smallest diameter position; structure of these two sections are identical, easy to produce for manufactory.

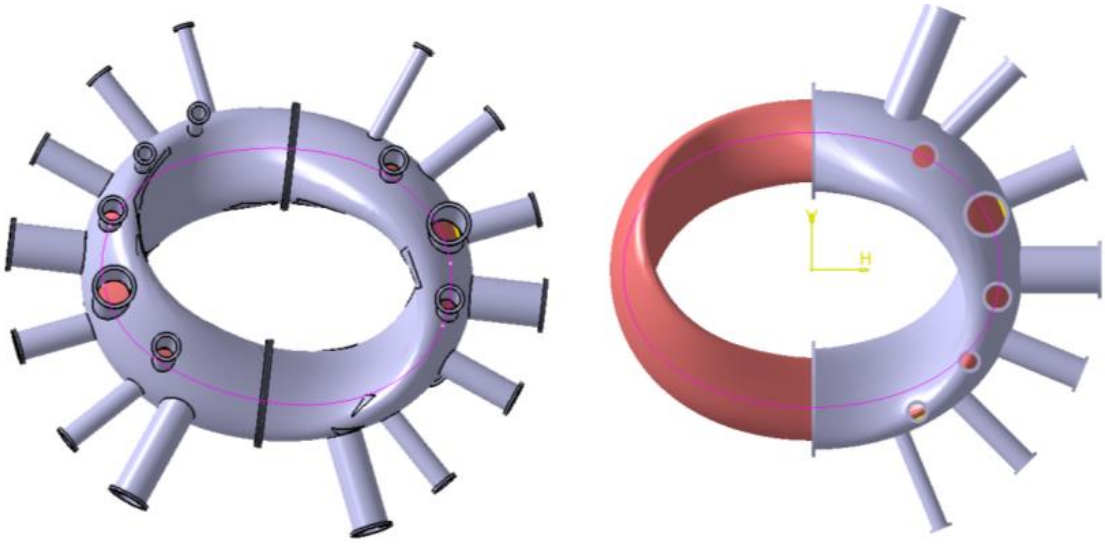

Fig. 4.3.1.5-1 Subsection of VV

Preliminary adoption of main body sealing ring is HELICOFLEX®, structure is packed spiral spring covered with non-enclosed soft metal; the characteristics are:

- Suitable for all kinds of special-shaped sealing;
- Good sealing performance durability;
- Standard O-type rubber ring is alternative, easy for flange machining.

- Data provided by the manufacturer: for the outer material is copper, free height is 4mm, sealing size is 44.45-762 mm, roughness of seal groove surface is Ra1.6~3.2, operating temperature can be reached at 300℃ (420℃ Max.), leak rate is less than 1×10^{-10} Pa m^3/s.

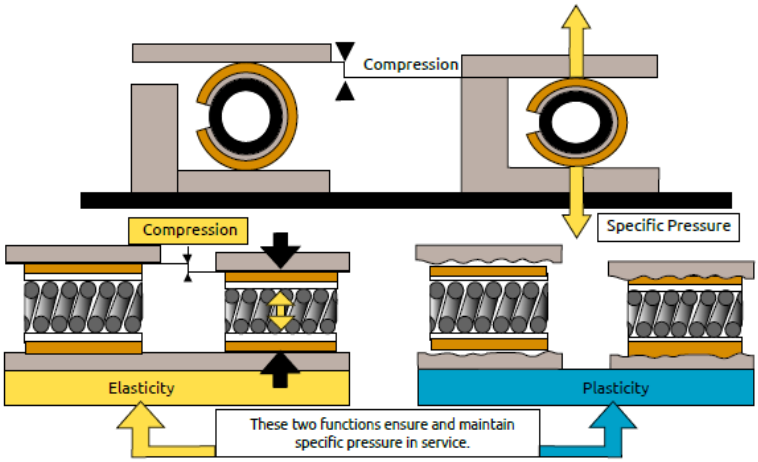

Fig.4.3.1.5-2 The Principle of HELICOFLEX® sealing

For the other interface, the CF flange can withstand high temperature baking is recommended.

4.3.1.6. Subsection of VV

Based on the position, there are three kinds of windows, their respective functions are:

- Horizontal window: diagnostic, heating, neutral beam injection (NBI) access;
- Lower window: pumping, cooling and measuring lines channel;
- Upper window: channel for diagnostic and etc.
- All window axis intersect with the magnetic axis.

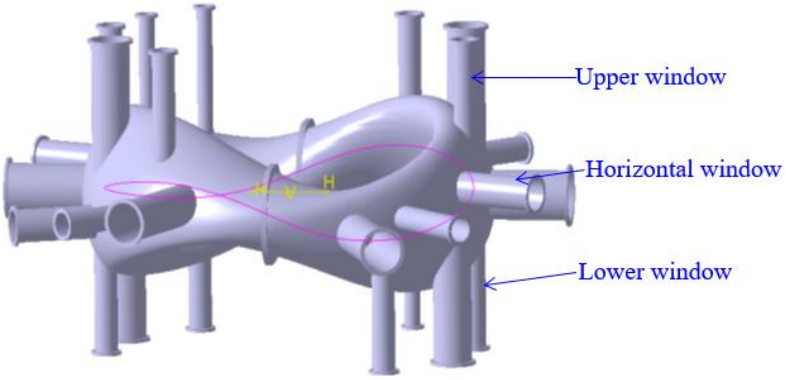

Fig. 4.3.1.6-1 Window distribution

Table 4.3.1.6-1 Table for main window (not contain the one less than DN100)

Size	Upper window	Horizontal window	Lower window	Total
DN300	0	2	0	2
DN250	2	2	2	6
DN200	0	4	0	4
DN160	4	4	4	12
DN100	2	2	2	6
Total	8	14	8	30

Because of space limited, and for convenient assembling, window necks are divided into upper and lower sections, shown as the above figure.

Necks and VV will be welded before assembly, the flange of connecting neck shall not affect the assembly, detailed design shall be based on the actual situation.

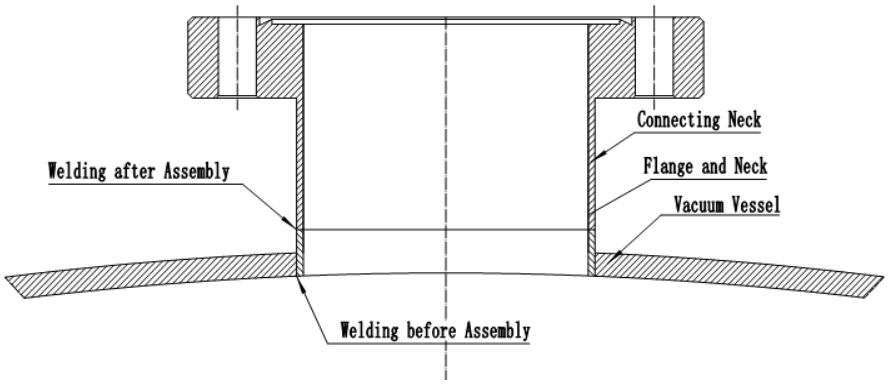

Fig. 4.3.1.6-1 Welding of window and neck

4.3.1.7. Design of pumping system

Based on the relevant experience of HSX, combined with the operating condition of CFQS, cryo-pump is used as main pump; turbo pump and dry pump are used as backing pump.

Characteristic and advantage: clean, pollution-free, high pumping speed, wide

working pressure range, high efficiency, simple structure and easy to use, long-term commissioned and can be installed in any direction.

As shown in the below figure, dry pump is used for rough pumping, then the turbo pump get involved, used for exhaust-system for cryo-pump during the temperature declining process, as the following steps:

Dry pump is used for 20-30 Pa, start the turbo pump, to reduce the time reach the work pressure. Dry pump grease can be ignored, this would not contaminate the VV.

Turbo pump id used for $5x10^{-2}$ Pa, start the cryo-pump, to reduce the starting pressure, this is beneficial to prolong the working cycle of cryogenic pump.

For leakage, turbo pump is pumping fast, which is beneficial to keep high vacuum and leak detection.

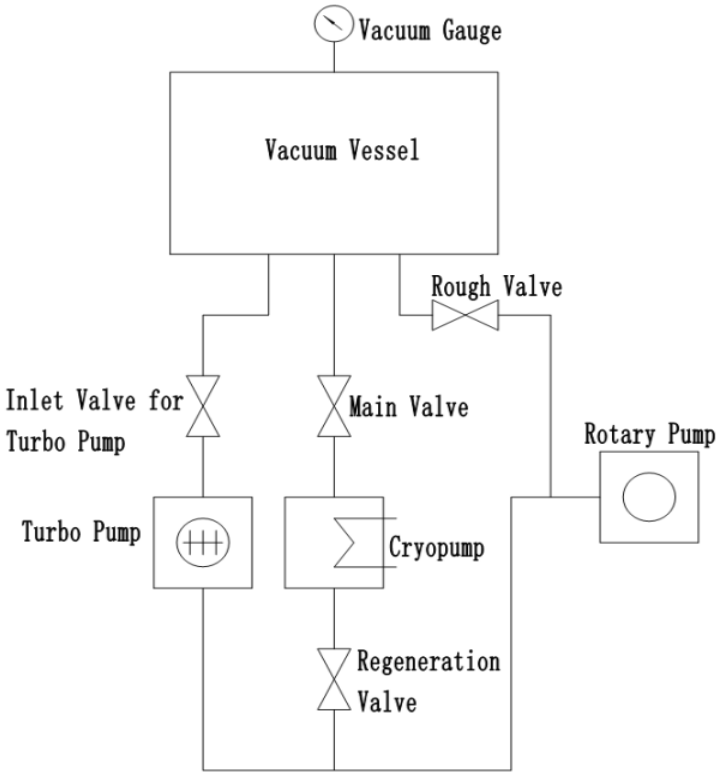

Fig. 4.3.1.7-1 Sketch of vacuum pumping system

4.3.1.8. Analysis and Optimum

Preliminary analysis and calculation of VV is performed during the main vessel design process; based on the thin-shell structure of VV, and internal and external pressure (inside of VV is vacuum, and outside is the atmospheric pressure) took into consideration, the analysis results are shown in the figure below.

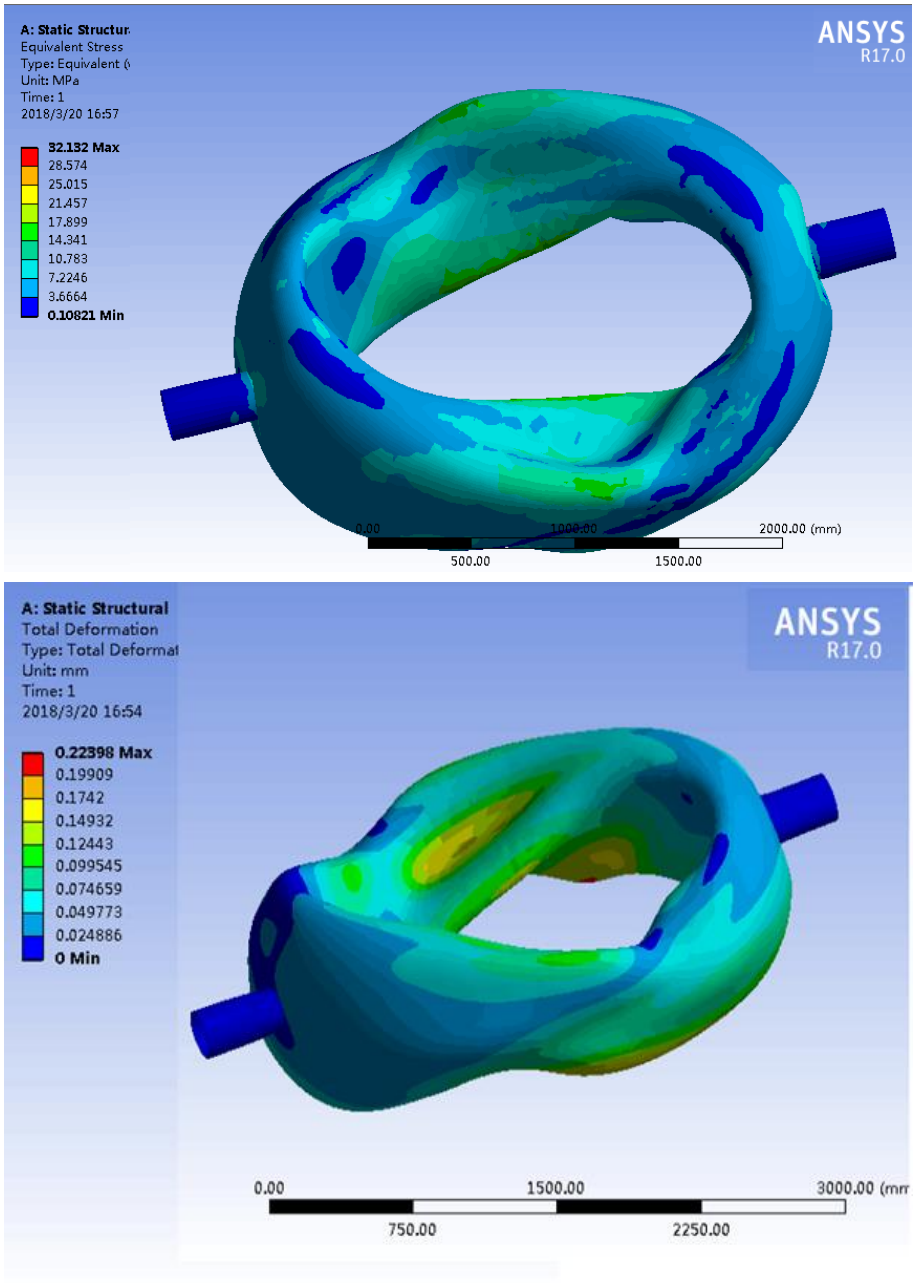

Fig. 4.3.1.8-1 Preliminary analysis results

As shown in the preliminary analysis results, the maximum stress of VV is 32 MPa under the atmospheric pressure, and the maximum deformation is 0.22 mm.

The following work is referring to the details of design terms section from Standard ASME VIII-2 (version later than 2007).

By using of FEM method, perform the linear and nonlinear buckling analysis, get these two kinds of different stress and strain loading curves, to verify the stability requirement, and further analysis and optimization is to be continued.

4.3.2 ECH port

For localized and controlled ECH power deposition and current drive, two dimensionally steerable power injection system with beam focusing is necessary. To realize the power injection system, at least, two mirror antenna system (one is plasma facing 2-D steerable plane mirror, and the other is beam focusing mirror) inside the vacuum vessel is required. The dimensions of the mirrors depend on the focused beam waist size at the plasma core region and the distance between the plasma and the mirrors. The antenna design should be optimized under the available circumstance of CFQS vacuum vessel design, to realize the beam waist size as small as possible in the plasmas.

For the power injection to the vacuum vessel, adequate vacuum window is needed. To minimize power reflection at the vacuum window, the thickness of the window d must satisfy a relation:

$d = n\lambda_{in}/2$.

Here, n is an integer and λ_{in} is wavelength of the heating wave in the window material.

4.3.3 NBI port

Tangential port with diameter of 300 mm is recommended to install NBI. The beamline is required to be arranged at the beam injection port with area of 10 m^2. The power supply system for filament arc discharge is also required to be arranged near the beamline. The typical area required for NBI system is summarized in Table 4.3.3-1.

Table 4.3.3-1 Summary of Access power to Electricity for NBI operation with port-though power of 1 MW and beam duration of 1 sec.

Area	Main Device	N-S [m]	E-W [m]	Area [m^2]
Area1F-1	A/F PS	3.5	6.5	22.75
Area1F-2	TRF,ACSW,DCC,	4.2	5.3	22.26
Area1F-3	CRYO cntl. panel	1	2	2
Area2F-1	GTOSW(GSW), DCL, VD,GS	5.5	5.2	28.6
Area2F-2	VCB, LVD	5.5	2	11
AreaB1	CryoComp	5	1.5	7.5
Total				94.11
BL Area	Beamline, IS	4	2.5	10
Cntrl Area	CPx2 + CPDx1 + PC	3.5	1.5	5.25

4.3.4 Diagnostic port

Port arrangement of the vacuum vessel in the CFQS is discussed in section 4.3.1.6. In Fig. 4.3.4-1, as a reference, the example of port arrangement for the CHS-qa [4.3.4-1] is shown. Interferometer (ϕ400), Thomson scattering (ϕ500), HIBP (ϕ260, ϕ300) are main port for diagnostics. Detail diagnostic port arrangement in the CFQS will be determined in the future, considering line of sight of diagnostic tools.

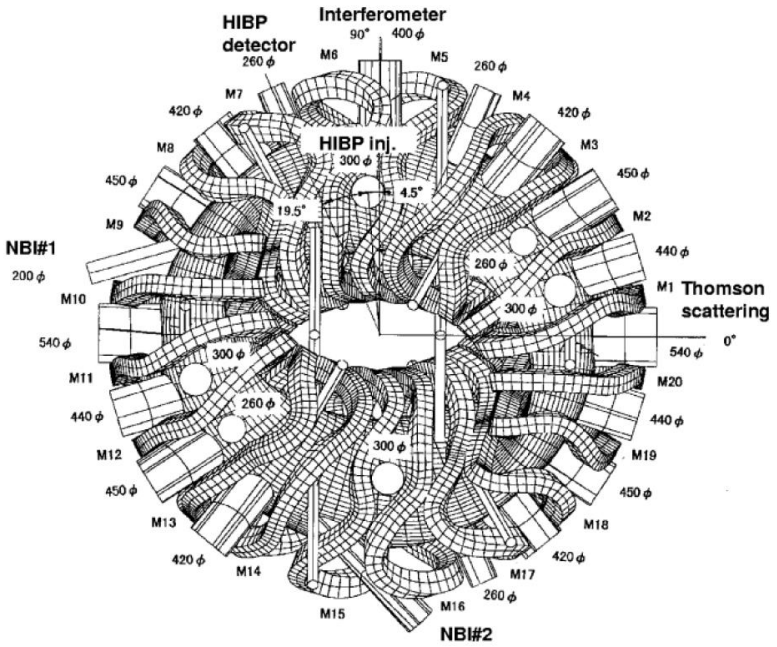

Fig. 4.3.4-1 Port arrangement for the CHS-qa

References

[4.3.4-1] K. Matsuoka *et al.*, Fusion Science and Technology **46** (2004) 379.

4.3.5 Limiter system

As in other magnetically confined fusion devices, the plasma in the CFQS is confined within closed magnetic flux surfaces and a boundary exists between plasmas and the machine-wall components. This boundary is generally called the scrape-off layer (SOL), which is determined by a solid surface (limiter) or topologically by magnetic field perturbations (divertor) [4.3.5-1]. In the SOL the impurities originated from plasma-facing components (PFCs) may cause a lot of problems, such as huge radiative power loss and dilution of fuel particles, it is therefore a crucial task to reduce impurities released from the PFC and prevent them from entering the plasma core region.

For the divertor configuration, plasma particles and energy leaving the confinement region are guided to the divertor target plate by open field lines. In stellarators, this divertor configuration can be intrinsically developed on the base of special edge magnetic structures arising from the small radial magnetic field resonant with rational surfaces [4.3.5-2]. Nevertheless, the stellarator divertor geometries may differ from each other, depending on the global magnetic shear. In the case of low-shear there exist chains of the island divertor, while in high-shear case the overlapping of island chains may form a stochastic layer [4.3.5-3]. In CFQS, the vacuum rational transform is designed between 2/6 and 2/5 from the core to the edge to avoid low-order rational surfaces, thus, the magnetic shear is quite low. It is expected from calculations that at the periphery of the CFQS, an island bundle divertor configuration will be formed under certain discharge conditions.

In different from the divertor, the limiter configuration is to use a solid surface to define the edge of the plasma. Depending on the shape and the positioning of the solid diaphragm, the limiters are generally divided into (i) poloidal limiter; (ii) rail limiter and (iii) toroidal limiter, as depicted in Fig. 4.3.5-1. The poloidal limiter is the simplest concept with a circular hole defined by a diaphragm normal to the toroidal magnetic field. The diameter of the hole is thus smaller than that of the vacuum chamber. Inside the hole the field lines are closed, while outside the hole the field lines are truncated by the diaphragm and the plasma density and temperature are radially decreasing due to parallel losses of particle and energy flux onto the limiter in the SOL. As a consequence, the limiter primarily serves to protect the wall from erosion by plasma heat loads. For withstanding heavy heat load, the limiter itself is usually made of a refractory material, such as carbon, tungsten, or molybdenum.

In the CFQS stellarator, although an innate divertor configuration exists in the plasma boundary, we intend to put two sets of the poloidal limiter inside the vacuum

chamber for defining the plasma and also protecting the wall. These two limiters will be installed at two approximately opposite toroidal locations of the torus. One limiter has a fixed diameter with a minor radius a = 27 cm. For the other one, its diameter is adjustable and the minor radius can be varied within a range of r = (20-27) cm. Because the CFQS is free of major plasma disruptions, there is little thermal shock occurred during the operation. Thus, the sputtering and arcing rates from limiters are expected to be very low. The material for the limiters can be C, W or Mo.

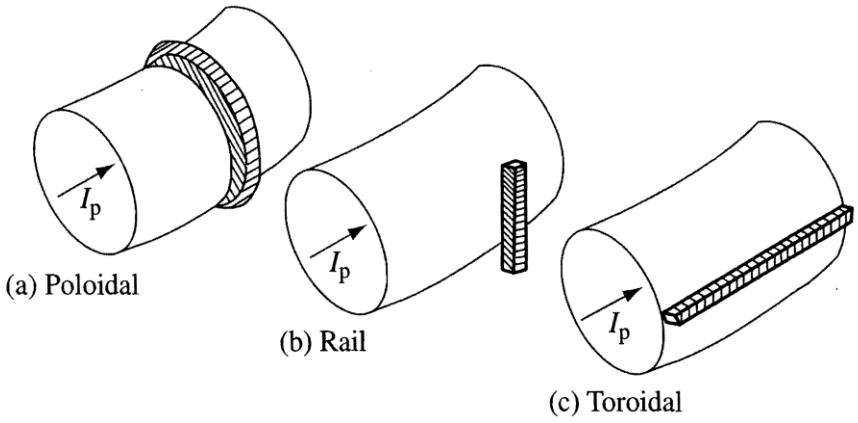

Fig. 4.3.5-1 Schematic of different types of the limiter

References

[4.3.5-1] J. Wesson, Tokamaks, fourth edition, Oxford University Press, 2011.

[4.3.5-2] Y. Xu, "*A general comparison between tokamak and stellarator plasmas*", Matter and Radiation at Extremes **1** (2016) 192 .

[4.3.5-3] Y. Feng, *et al.*, "*Comparison between stellarator and tokamak divertor transport*", Plasma Phys. Control. Fusion **53** (2011) 024009.

4.3.6 Divertor configuration

In designing the magnetic configuration of an experimental device, the first priority is placed on designing the configuration of the core confinement region. However, it is well known that without a proper design of magnetic configuration of the peripheral region the concept is not useful for the fusion reactor. This is called 'divertor design' because the most important physics issue related to the peripheral magnetic configuration is particle and heat removal.

In tokamak research, the concept of divertor is almost established and all existing

tokamak devices in the world have similar divertor configuration (single null divertor) with the direct extension to the tokamak demo design. There are still discussions for the new ideas of advanced configurations (double null divertor and snow flake divertor) but they have not been adopted in real experimental devices. In stellarator research, we do not have one established concept of divertor partly because we have varieties of stellarator configurations and divertor concept strongly depends on the magnetic configuration of core confinement region. In fact, for the two largest stellarator experiments, LHD and W7-X, these devices have different divertor structures. In LHD, the intrinsic helical divertor has divertor magnetic field lines connecting the ergodic boundary layer of the core confinement region and the divertor plates on the wall [4.3.6-1]. In W7-X, the island divertor provides a sophisticated divertor structure combined with small islands created near the boundary of the core confinement region [4.3.6-2]. For the new stellarator CFQS in China, we are designing a new divertor configuration which provides a sufficiently long connection length of magnetic field lines between the plasma boundary and the wall.

Three poloidal cross sections of the last closed magnetic surfaces (LCMS) of CFQS are shown in Fig.4.3.6-1. Modular coils were designed to realize such a magnetic configuration with a choice of the number of coils around the torus as 16 [4.3.6-3,4]. The success of this coil design was the most important contribution to the finding of a new divertor concept for CFQS. Fig. 4.3.6-2 shows the punctual plots of the vacuum magnetic field lines (magnetic surfaces) produced with these modular coils (for the third cross section in Fig.4.3.6-1). Red line shows the LCMS of the target configuration in the modular coil design. The magnetic field produced by the modular coils has many closed magnetic surfaces with a larger area beyond the target LCMS. In usual cases of designing modular coils for the advanced stellarator, it is very difficult to make larger closed magnetic surfaces beyond the target LCMS because the boundary area usually becomes stochastic.

Fig. 4.3.6-3(a) shows the profile of the rotational transform of the magnetic configuration produced by the modular coils. A very flat profile for the outer region is also very important for the new divertor concept. Red mark shows the averaged radius of the LCMS of the target configuration. Although we decided upon an aspect ratio of 4 for the CFQS device, it is technically possible to create a larger confinement region if we design the vacuum chamber with a sufficiently large size to provide space for such larger magnetic surfaces. A control of plasma boundary with movable limiter might be a possible choice for the plasma operation control.

When we introduce the auxiliary toroidal coils to provide additional toroidal field to

the stellarator field produced with modular coils, the magnetic configuration is changed to include large islands at the boundary of the core confinement region shown in Fig. 4.3.6-4. The quasi-axisymmetry is conserved with the additional toroidal field. The strength of the additional toroidal field is -0.055 times averaged toroidal field produced by modular coils. The rotational transform is increased to change the boundary value to 0.4 (shown in Fig. 4.3.6-3(b)). This is a typical magnetic configuration for any type of stellarator that has a rational value of the rotational transform near the boundary. However, essential differences between the configuration shown in Fig. 4.3.6-3 from many other cases are 1) large size of islands and 2) the completeness of the island magnetic surfaces. It is shown in Fig. 4.3.6-3 that clearly formed island bundle flux surrounds the core confinement region with a clearly defined interface of the magnetic field separatrix. This is the reason why we call such a configuration as 'island bundle divertor (IBD)'. The entire magnetic confinement area is clearly separated into two regions: hot plasma region in the core and cold plasma region in the periphery.

Fig. 4.3.6-5 shows the divertor field line tracing, which is created in the following calculation procedures. We found first the LCMS of the core confinement region. Then we distributed many field line tracing starting points with a small deviation (5 mm for R=1 m torus) from the LCMS. Because the island magnetic surfaces are complete, there is no escaping field line in such a calculation. Fig. 4.3.6-5 shows blue line for one of the possible shapes of the vacuum chamber wall. If we install divertor plates at this wall position, the cold plasma in the island bundle flux can be absorbed at the divertor plates. Fig. 4.3.6-6 shows the divertor tracing with the wall target where the field line tracing is stopped. The pattern of the magnetic field line punctual plots is very similar to the tokamak divertor structure. In fact, the transport of the magnetic field lines is exactly the same as tokamak divertor, where the peripheral regions of the divertor are connected to the core confinement region with a clear magnetic separatrix, and divertor magnetic field lines in divertor region have long connection length between the null point and the wall. Because the magnetic field lines go around through all five island bundle fluxes with very small incident angles to the wall, the distribution of the heat load on the divertor plates is determined by the precise geometric design of the shapes and the locations of divertor plates.

The length of the followed field lines between start points near LCMS and the divertor plate position is more than 150 m in this calculation and there is no exceptional field line with shorter length. This is because the island magnetic surfaces are very clear and there is no ergodic region between the core confinement region and the divertor bundle flux. This is a very clear difference from the LHD-type divertor

structure where there are some field lines with shorter length between the core region and the divertor plate because of the ergodicity of the boundary layer of the core confinement region. In the discussions of connection length, the island bundle divertor is similar to the tokamak divertor situation in the sense that the divertor field lines do not have strong poloidal magnetic field component, which makes the connection length shorter.

Because the rotational transform of IBD region is 0.4, island bundles shown in Fig. 4.3.6-4 are connected together. In other words, this bundle flux is a single flux. Thus particles and heat flux transferred from the core confinement region to the IBD can be removed at any position in the torus. Because the space between the plasma and the wall is very narrow in the toroidal position of the crescent shape of plasma (the leftmost LCMS in Fig. 4.3.6-1), we can avoid installing divertor structure at this region and take advantage of installing it where the space is larger. As shown in Fig. 4.3.6-6, the number of divertor feet is as many as ten. Thus it is possible to reduce the maximum heat load at the divertor compared with the tokamak case, where the number of feet is two (in the case of a single null). On the other hand, because the divertor fields are all connected into a single structure, it is not necessary to install as many as ten divertor plates.

Since the island structure is in general very sensitive to the control of the rotational transform, the control of bootstrap current in the stellarator operation will be essential to keep the IBD concept stable. However, we know that any plasma parameters and engineering parameters must be controlled extremely accurately in the future fusion reactor. The control of bootstrap current would be within available control knobs in the fusion reactors. Furthermore, the increase of the rotational transform necessary for IBD formation is in the range of possible bootstrap current effect of the quasi-axisymmetric stellarator.

References

[4.3.6-1] Y. Takeiri, T. Morisaki, M. Osakabe *et al.*, Nucl. Fusion **57** (2017) 102023.
[4.3.6-2] R. C. Wolf *et al.*, Nucl. Fusion **47** (2017) 102020.
[4.3.6-3] H. Liu, A. Shimizu, M. Isobe *et al.*, submitted to Plasma Fusion Res.
[4.3.6-4] A. Shimizu, H. Liu, M. Isobe *et al.*, submitted to Plasma Fusion Res.

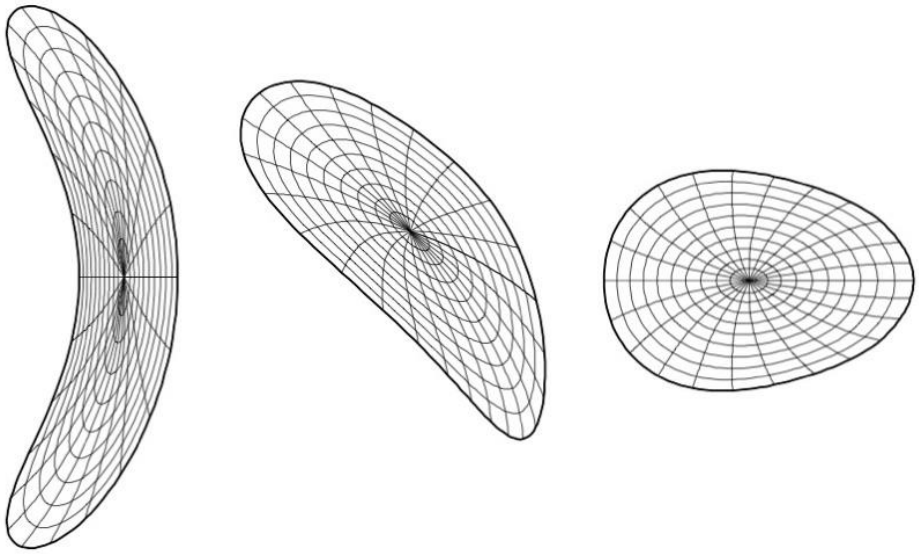

Fig. 4.3.6-1 Last closed magnetic surfaces for CFQS advanced stellarator design. Cross sections for three toroidal positions are shown.

Fig. 4.3.6-2 Punctual plots of magnetic surfaces for CFQS configuration produced by 16 modular coils. Red line corresponds to the LCMS of the 3rd plot in Fig. 4.3.6-1

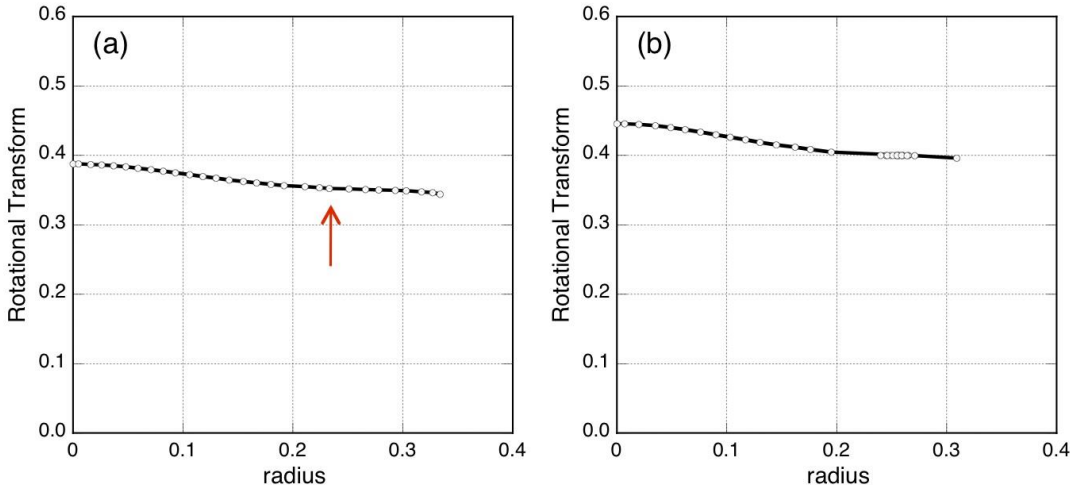

Fig. 4.3.6-3 (a) Rotational transform profile of vacuum field of CFQS. Red arrow indicates the position of LCMS of target configuration. (b) Rotational transform profile of island bundle divertor configuration with additional toroidal field.

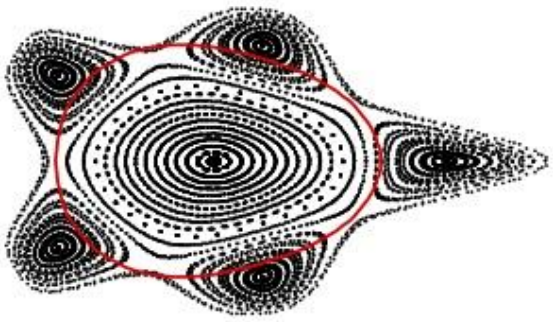

Fig. 4.3.6-4 Magnetic configuration of island bundle divertor.

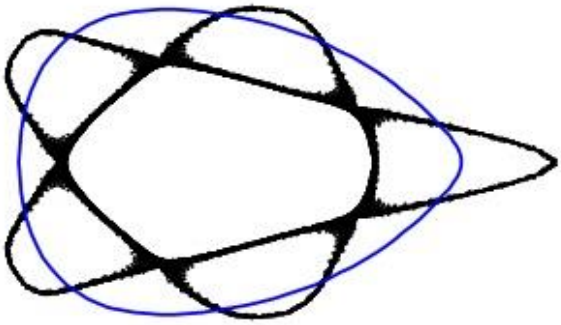

Fig. 4.3.6-5 Divertor field line tracing for island bundle divertor. Blue line shows one example of vacuum chamber wall position for locating divertor plates.

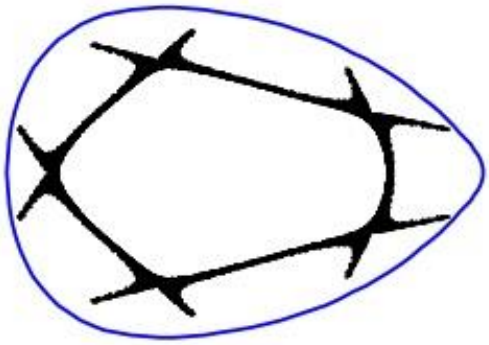

Fig. 4.3.6-6 Divertor field line tracing with assumed existence of divertor targets.

4.3.7 Baking system

4.3.8 Discharge cleaning

4.4 Power supply system

4.4.1 Power supply system for Modular coils

4.4.2 Power supply system for ECRH

For the operation of the 54.5 GHz gyrotron, power supply (PS) systems such as precisely controlled high voltage direct current (DC) PS, DCPS of ~kV order output, and low voltage alternating current (AC) electric power up to 200 V. Here, the PS system used in the CHS experiment is described as an example.

The high voltage DCPS system consists of:
Charger which generates DC high voltage up to 100 kV from 200 V AC,
Condenser bank with 86 condensers of 1.5 micro Farad electrostatic capacitance each,
Crowbar which works as fast high voltage switch in the case of failure detection, and
Regulator tube (EIMAC X2062K tetrode tube) which supplies precisely controlled high voltage up to 70 kV DC to the gyrotron.

Ion pumps to keep the vacuum conditions inside the gyrotron and the regulator tube require DCPSs of ~3.5 kV output.

Heaters to generate thermal electron beams in the gyrotron and the regulator tube require ACPSs of up to 150 V output.

High voltage PS used for crowbar-drive works at 8 kV DC.

Super conducting magnet (SCM) which generates magnetic field around gyrotron cavity requires DCPS of ~2 V/33 A output.

4.4.3 Power supply system for NBI

Access power to Electricity for NBI with port-through power of 1 MW and beam duration of 1 sec is almost 4 MVA in total. The Access powers of high voltage power supply for beam acceleration is 3.7 MVA, filament and arc power supply is 250kVA, high voltage power supply for beam deceleration is 26 kVA and DC power supply for beam bending magnet is 20 kVA.

Table 4.4.3-1 Summary of Access power to Electricity for NBI operation with port-though power of 1 MW and beam duration of 1 sec.

Acl PS	A/F PS	DclPS	BndMag PS	total
3.7MVA	250kVA	26kVA	20kVA	~4MVA

4.4.4 Power supply system for Vacuum pumping system

4.4.5 Power supply system for Diagnostics

4.4.6 Power supply system for Data acquisition

4.4.7 Power supply system for Utilities

4.5 Pure water cooling system

4.5.1 Pure water cooling system for Modular coils

4.5.2 Pure water cooling system for ECRH

For safety operation of the 54.5 GHz gyrotron, required flow rates of cooling water to remove heat loads on the parts of the gyrotron are,

Collector: 100 L/min.

Body: 6 L/min.

Vacuum window: 9 L/min.

Oil tank: 6 L/min.

with the water pressure of < 2 kgf/cm^2 at inlet flow.

If a regulator tube is used in the high voltage power supply system for the gyrotron, flow rate of the cooling water of ~120 L/min for the regulator tube EIMAC X2062K, as an example in the case of CHS experiment, would be additionally required.

4.5.3 Pure water cooling system for NBI

4.5.4 Pure water cooling system for Vacuum pumping system

4.5.5 Pure water cooling system for Diagnostics

4.5.6 Pure water cooling system for Utilities

4.6 Compressed air supply system

4.7 Heating system

4.7.1 ECRH

The main component of the electron cyclotron resonance heating (ECRH) system is gyrotron. The gyrotron which was used for CHS experiment and will be used in CFQS experiment has an oscillation frequency of 54.5 GHz and the maximum output power of up to 450 kW. The maximum pulse length is 100 ms. The gyrotron was produced by a Russian company, GYCOM.

The EC-waves generated by the gyrotron effectively and locally heat the electrons at a position on the EC-wave beam path where the resonance condition

$n \cdot \omega_{ce} = \omega - k_{//} \cdot v_{//}$,

$\omega_{ce} \equiv eB/m_e$

is satisfied.

Here, integer n denotes harmonic number, ω_{ce} is electron cyclotron angular frequency, e is a unit charge of an electron, B is the strength of magnetic field, m_e is the mass of an electron with relativistic effect, ω is angular frequency of EC-waves, and $k_{//}$ and $v_{//}$ are the components of wave number and electron velocity parallel to the magnetic field line, respectively.

Applying the frequency of 54.5 GHz with n = 1 (fundamental resonance) and $k_{//} = 0$ (pure ECRH without Doppler effect), in the non-relativistic case, the resonance condition is satisfied with $B = 1.95$ T. For n = 2 (second harmonic resonance), $B = 0.97$ T should be set.

In the case of the CHS experiment, the EC-wave power was transmitted from the gyrotron to the CHS vacuum vessel by a quasi-optical transmission line. The transmission line was furnished with focusing and plane mirrors, polarizer mirrors to control transmitted wave's polarization arbitrarily, and vacuum window to keep the vacuum condition in CHS. In the CHS vacuum vessel, an EC-wave beam injection antenna system consisted of a focusing mirror and a two-dimensionally steerable plane mirror was installed. By use of the power transmission and injection systems, effective and localized ECRH with power deposition control, electron cyclotron current drive (ECCD), and electron Bernstein wave heating (EBH) were realized [4.7.1-1 ~ 8].

References

[4.7.1-1] Y. Yoshimura *et al.*, J. Plasma and Fusion Research Series **6** (2004) 651.

[4.7.1-2] Y. Yoshimura *et al.*, Plasma and Fusion Research **1** (2006) 029.

[4.7.1-3] Y. Yoshimura *et al.*, J. Korean Physical Society **49** (2006) S197.

[4.7.1-4] Y. Yoshimura *et al.*, J. Physical Society of Japan **75** (2006) 114501.

[4.7.1-5] Y. Yoshimura *et al.*, Plasma and Fusion Research **1** (2006) 053.
[4.7.1-6] Y. Yoshimura *et al.*, Fusion Science and Technology **52** (2007) 216.
[4.7.1-7] Y. Yoshimura *et al.*, Fusion Science and Technology **53** (2008) 54.
[4.7.1-8] Y. Yoshimura *et al.*, Plasma and Fusion Research **3** (2008) S1076.

4.7.2 NBI

Neutral beam injection (NBI) is a powerful tool for plasma heating and drive of the plasma current and flow. In order to study energetic particle physics, tangential NBI is an inevitable device. Followings are specification of NBI planned in this project;

Specification:

Beam species: H/D
Beam energy: 20-40 keV
Port-through power: 1 MW
Beam duration: ~1 sec
Ion source: Filament-arc discharge with cusp magnets
Beam acceleration area: ϕ 300 mm
Aperture radius: ϕ 5 mm
Current density: 250 mA/cm^2
Beam optics: Conversing beam via offset aperture
Focal length of the beam: ~3.0 m
Beam divergence angle: ~1 degree
Diameter of drift Tube: ϕ 250mm
Neutralization: gas cell
Main vacuum pump: cryo-sorption panel (326 m^3/s)
Diagnostics: calorimetric beam profile measurement

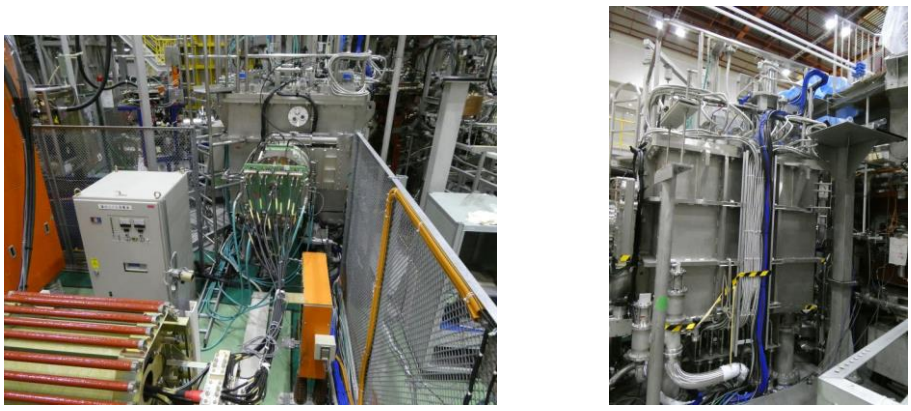

(a) (b)

Fig. 4.7.2-1 (a) Back side view of CHS-NBI#2 and positive ion source, (b) Side view of CHS-NBI#2.

4.8 Diagnostics

Diagnostics are indispensable for studying high temperature plasma physics in modern fusion research. There are a lot of interesting topics to be studied; transitions to improved confinement modes, formation of transport barriers, and their impact on plasma turbulence, etc. Roles of diagnostics are increasing in the studies on high temperature plasma properties, not only for fusion but also for basic physics.

CFQS is an innovatively designed device so as to achieve tokamak-like confinement properties and helical-like stability at the same time. Plasmas produced in the CFQS will become a good target for researches which aim at achieving cost-effective stable burning plasmas. High-quality data based on detailed measurements should be obtained for comprehensive understanding of toroidal plasmas.

As mentioned above, anomalous transport and improved confinement modes are important issues for understanding toroidal plasmas. Based on the successful results of the advanced diagnostics in CHS and LHD, we will employ advanced diagnostic systems such as heavy ion beam probe (HIBP) and microwave reflectometry in CFQS to study the following topics:

1) Spatio-temporal turbulence structure

2) Structures of electric field and plasma flow

After the installation of NBI in the future, we will consider developing charge exchange spectroscopy (CXS) for the measurement of radial electric field and plasma flow velocity to study the relation between toroidal rotation and momentum input.

Also, physics of density limit is important in helical devices because confinement property of helical systems is improved as the density increases following the scaling law. Therefore, higher priorities are given for the diagnostics of edge plasma, MHD and radiation power, including magnetic probe, bolometer, etc.

For basic diagnostics, microwave interferometer should be firstly developed to measure the electron density. Thomson scattering is also important to study the physics of transport barriers. Multi-dimensional measurement is useful for studying internal structure of basic plasma parameters. Therefore, the development of two-dimensional or three-dimensional measurements will be performed as far as possible. So that the structure and non-linear development of plasmas can be observed in detail.

Diagnostics planned in the CFQS are listed in Table 4.8-1. Assignment of ports to these diagnostics will be planned in the future. Some of the ports should be specifically designed for HIBP and Thomson scattering because these diagnostics require special geometries.

Table 4.8-1 Diagnostics planned in the CFQS

Basic diagnostics

Parameters	diagnostics	Remarks
Electron density	Microwave interferometer	150 GHz
	Far infrared interferometer	
	Thomson scattering	Multichannel
Electron temperature	Thomson scattering	Multichannel
	Electron cyclotron emission	
Ion temperature	Charge exchange spectroscopy	After NBI installation
MHD	Magnetic probe	
Edge plasma	Langmuir probe	
	Hα detector	
Radiation power	Pyroelectric detector	
	Resistive bolometer	
	AXUV photodiode array	20 channel
Stored energy	Diamagnetic loop	
Plasma Current	Rogowski coil	
Impurities	Vacuum ultraviolet spectroscopy	

Advanced diagnostics

Parameters	diagnostics	Remarks
Electric potential/field	Heavy ion beam probe	
Plasma rotation	Charge exchange spectroscopy	After NBI installation
Lost ions	Lost ion probe	
Turbulence	Heavy ion beam probe	
	Microwave reflectometer	Multichannel

4.9 Data acquisition system

5. Research plan and schedule

The schedule plan is shown in the table 5.1.

Phase I : Physics design (configuration, neoclassical transport, MHD etc.) and main machine design (modular coils, vacuum vessel, supporting structure etc.)

Phase II : Fabrication of CFQS and transfer essential heating and diagnostic systems from NIFS to SWJTU, such as gyrotron, interferometer, X-ray diagnostic, etc.

Phase III : Commissioning, verify construction accuracy and obtain first plasma.

Phase IV : Magnetic configuration studies and heating experiments.

More detail plan is shown in the table 5.2. Up to 2022 March (end of FY2021), the first plasma of the CFQS will be achieved.

Table 5-1 Schedule on the NSJP for the CFQS

JFY	4	5	6	7	8	9	10	11	12	1	2	3
H29(2017)	Phase I: Physics design and main machine design											
H30(2018)	Phase I: Physics design and main machine design					Phase II: Fabrication of CFQS Transfer heating systems and diagnostic systems from NIFS to SWJTU						
H31(2019)	Phase II: Fabrication of CFQS Transfer heating systems and diagnostic systems from NIFS to SWJTU											
H32(2020)	Phase II: Fabrication of CFQS Transfer heating systems and diagnostic systems from NIFS to SWJTU									Phase III: Commissioning and First plasma		
H33(2021)	Phase III: Commissioning and First plasma			Phase IV: Operation								

Table 5-2 Detailed schedule plan